

**Atomistic Simulations of Solute-Interface
Interactions in Iron**

by

Hao Jin

B.Sc., Shandong University, 2006

M.Sc., Shandong University, 2009

A THESIS SUBMITTED IN PARTIAL FULFILLMENT
OF THE REQUIREMENTS FOR THE DEGREE OF

Doctor of Philosophy

in

THE FACULTY OF GRADUATE AND POSTDOCTORAL
STUDIES

(Materials Engineering)

The University of British Columbia
(Vancouver)

June 2014

© Hao Jin, 2014

Abstract

The kinetics of the recrystallization and austenite-ferrite (fcc-bcc) phase transformation in steels are markedly affected by substitutional alloying elements. Nevertheless, the detailed mechanisms of their interaction with the grain boundaries and interfaces are not fully understood. Using density functional theory, we determine the segregation energies of commonly used alloying elements (e.g. Nb, Mo, Mn, Si, Cr, Ni) in the $\Sigma 5$ (013) tilt grain boundary in bcc and fcc Fe, and the bcc-fcc interfaces. We find a strong interaction between large solutes (e.g. Nb, Mo and Ti) and grain boundaries or interfaces that is consistent with experimental observations of the effects of these alloying elements on delaying recrystallization and the austenite-to-ferrite transformation in low-carbon steels. In addition, we compute the solute-solute interactions as a function of solute pair distance in the grain boundaries and interfaces, which suggest co-segregation for these large solutes at intermediate distances in striking contrast to the bulk.

Besides the prediction of solute segregation, the self- and solute-diffusion in Fe-based system are also investigated within a framework combining density functional theory calculations and kinetic Monte Carlo simulations. Good agreement between our calculations and the measurements for self- and solute diffusion in bulk Fe is achieved. For the first time, the effective activation energies and diffusion coefficients for various solutes in the α -Fe $\Sigma 5$ (013) grain boundary are determined. The results demonstrate that grain boundary diffusion is significantly faster than for lattice diffusion, confirming grain boundaries are fast diffusion paths. By contrast, the effective activation energy of self-diffusion in a bcc-fcc Fe interface is close to the value of fcc bulk self-diffusion, and the investigated bcc-fcc interface provides a moderate “fast diffusion” path.

Preface

This dissertation is written based on original research conducted by the author, Hao Jin. All of the work presented henceforth was conducted in the Materials Engineering Department of the University of British Columbia, at the Point Grey Campus. My supervisor Dr. Matthias Militzer was involved in all stages of the project, provided guidance and assisted with the manuscript composition.

Figures 1.1, 2.1, 2.2, 2.3, 2.4, 2.5, 2.6, 2.7, 2.8, 2.9, 2.10 2.11 2.12 2.13 2.14 2.15 2.16 2.17 2.18 2.19 and 4.1 in the introduction, literature review and methodology chapters have been taken with permission from the cited sources.

The contents of Chapter 5 were published in: Hao Jin, Ilya Elfimov and Matthias Militzer, “Study of the interaction of solutes with $\Sigma 5$ (013) tilt grain boundaries in iron using density-functional theory”, *J. Appl. Phys.*, vol. 115, p. 093506, 2014. Part of the simulation results was also presented in a conference: Hao Jin, Ilya Elfimov and Matthias Militzer, “Study of the interaction of solutes with interfaces in iron using density-functional theory”. 2011 TMS Annual Meeting and Exhibition, San Diego, CA, 2011.

Chapters 6 and 7 are based on the simulation work I conducted, and it will be submitted for publication. Part of the simulation results was also presented in a conference: Hao Jin, Ilya Elfimov and Matthias Militzer, “First-principles Simulations of the Interaction of Alloying Elements with the Austenite-ferrite (fcc-bcc) Interface in Iron”. 2014 TMS Annual Meeting and Exhibition, San Diego, CA, 2014.

Chapter 8 is based on the simulation work I conducted. Section 8.3

was presented in a conference: Hao Jin, Ilya Elfimov and Matthias Militzer,
“Atomistic simulations of solute interface interactions in iron”. 2012 TMS
Annual Meeting and Exhibition, Orlando, FL, 2012.

Table of Contents

Abstract	ii
Preface	iii
Table of Contents	v
List of Tables	viii
List of Figures	x
List of Symbols	xix
List of Abbreviations	xxv
Acknowledgements	xxvii
1 Introduction	1
2 Literature Review	6
2.1 Introduction	6
2.2 Solute Segregation on Grain Boundaries	6
2.2.1 Simulations of Grain Boundary Segregation	6
2.2.2 Binding Energy	10
2.2.3 Effects of Solutes on Grain Boundary Properties	13
2.3 Solute Diffusion in Grain Boundaries	16
2.3.1 Overview	16
2.3.2 Solute Diffusion in α -Fe	17

2.3.3	Point Defects in Grain Boundaries	20
2.3.4	Diffusion Mechanisms in Grain Boundaries	22
2.4	Austenite (fcc) and Ferrite (bcc) Interface	26
2.4.1	Overview	26
2.4.2	Approaches to Study Magnetism in γ -Fe	26
2.4.3	Effects of Solutes on Magnetism of γ -Fe	29
2.4.4	DFT Studies for Heterophase Interfaces	31
2.5	Conclusions	34
3	Scope and Objectives	36
4	Methodology	38
4.1	Density Functional Theory	38
4.1.1	Fundamentals	38
4.1.2	Exchange-correlation Energy	39
4.1.3	Structure Optimization	40
4.1.4	Simulation Software Package	41
4.1.5	Domain Size	43
4.1.6	Parameter Setup and Formulas for DFT Calculations	48
4.1.7	Simulation Procedure for Solute Segregation	48
4.1.8	Simulation Procedure for Diffusion	49
4.1.9	Hessian Matrix and Vibrational Frequencies	51
4.2	Kinetic Monte Carlo Simulations	52
4.3	Molecular Statics Simulations	54
5	Interaction of Solutes with the $\Sigma 5$ (013) Tilt Grain Boundary in Iron	55
5.1	Grain Boundary Structure	55
5.2	Grain Boundary Energy	56
5.3	Single Solute Segregation Energies	57
5.4	Solute-solute Interactions at the Grain Boundary	63
5.5	Molecular Statics Simulations	71
6	First-Principles Study of Face-Centered Cubic γ-Iron	74
6.1	Bulk and Grain Boundary Structures in γ -Fe	74

6.2	Magnetic Configurations for γ -Fe	77
6.3	Single Solute in γ -Fe	80
6.4	Solute-solute Interactions in γ -Fe	83
6.5	Solute Segregation in $\Sigma 5$ Grain Boundaries in fcc γ -Fe	86
7	Interaction of Solutes with α-γ Iron Interface	90
7.1	Structure of Ferrite-Austenite (bcc-fcc) Interface	90
7.2	Interface Energy	93
7.3	Magnetic and Electronic Properties for bcc-fcc Interface	95
7.4	Binding Energies of Solutes with bcc-fcc Interface	97
7.5	Solute-solute Interactions in bcc-fcc Interface	107
8	Simulation of Self- and Solute-diffusion in Fe	111
8.1	Diffusion in Fe bcc Lattice	111
8.2	Diffusion in the Fe fcc Lattice	117
8.3	Grain Boundary Diffusion in bcc Fe	122
8.4	Diffusion in the bcc-fcc Fe Interface	128
9	Conclusions and Future Work	132
9.1	Conclusions	132
9.2	Future Work	135
	Bibliography	136

List of Tables

Table 2.1	Binding energies (in eV) of various non-metallic elements with special grain boundaries.	12
Table 2.2	Calculated activation energies of fully ordered ferromagnetic state (Q_0) and pre-factor (D_0) in α -Fe vs. experimental data.	19
Table 5.1	Magnetic moments (μ_B) for single solute in grain boundary (GB) and bulk sites.	68
Table 6.1	Predictions of lattice parameters (a_l), and magnetic moments (MM) for magnetic phases of α and γ -Fe at 0 K. Earlier DFT and experimental results are also shown for comparison.	78
Table 6.2	Effective binding energies (E_{seg}^{eff}) for selected solutes in $\Sigma 5$ bcc and fcc grain boundary. Unit is eV.	88
Table 7.1	Surface and interface energies for the equilibrium bcc and fcc surfaces, and bcc-fcc interface, in units of J/m ² .* . . .	94
Table 8.1	Calculated vacancy formation energy (E_v), migration energy (E_m), vacancy-solute binding energy (E_b), and activation energy (Q_0) for self- and solute-diffusion in bcc Fe.	113

Table 8.2	Vacancy formation energies (E_v), vacancy migration barrier (E_m), and the activation energy for self-diffusion (Q_0) along each path. The migration paths are labeled in Figure 6.1.	118
Table 8.3	Lattice constants (a_l), atomic volume (V), vacancy formation energy (E_v), effective migration energy (E_m^{eff}), and effective activation energy (Q_a^{eff}) as a function of temperature.	119
Table 8.4	Calculated migration energy for various solutes along grain boundary (E_m , in units of eV). Sites a_0 , b_0 , c_0 , and c refer to boundary sites as shown in Figure 5.1.	125
Table 8.5	The effective activation energy (Q_{gb}) in $\Sigma 5$ (013) grain boundaries and the ratio of Q_{gb}/Q_{bulk}	127
Table 8.6	Migration energies of vacancy for different types of jump paths as defined in the text in the bcc-fcc interface. The arrows indicate the spin states of the jump Fe atoms in initial and final states.	130
Table 8.7	Activation energy for Fe self-diffusion in the bcc-fcc interface, fcc bulk, bcc bulk, and $\Sigma 5$ grain boundaries (GBs) at 0K. Unit is eV.	130

List of Figures

Figure 1.1	Variation of the interface velocity (ν) versus the applied driving pressure (P_d) for systems with different solute concentrations ($C_i, i = 1, 2, 3$) [5].	2
Figure 2.1	Side view of the Fe $\Sigma 3$ (111) grain boundary [15]. (a) Cluster of 53 atoms and (b) cluster of 91 atoms. The open circle represents solute atom.	7
Figure 2.2	Side view of the Fe $\Sigma 3$ (111) and $\Sigma 5$ (210) grain boundaries [25]. The lighter and darker circles mark the atoms belonging to two different planes. The interstitial positions at the grain boundary are indicated by the yellow circles. The substitutional positions in different grain layers are labeled by the numbers. Lower panels show top view of the supercells taken in the cross-section plane passing through the grain boundary (broken line).	8
Figure 2.3	$\langle 100 \rangle$ symmetric tilt grain boundary structures with structural units outlined for the $\Sigma 5(210)$, $\Sigma 29(730)$, $\Sigma 5(310)$ and $\Sigma 17(530)$ boundaries [19]. Black and white denote atoms on different 100 planes. The different structural units are labeled as A, B, and C.	10

Figure 2.4	MD simulation of the Cu $\Sigma 5(210)$ grain boundary at 800K allowing variations in grain boundary density. The boundary undergoes a first-order phase transformation from filled kites (labeled in blue color) to split kites (labeled in red color) nucleating and growing from the surface [29].	11
Figure 2.5	DFT simulations for segregation energies as a function of segregation site for the Fe $\Sigma 3(111)$ grain boundary with sulfur at the substitutional site [34].	13
Figure 2.6	Calculated binding energies of phosphorous with varying the segregation concentration in the $\Sigma 3(111)$ grain boundary in Fe [35].	14
Figure 2.7	Results of energy difference relative to the equilibrium vs. uniaxial tensile strain for the pristine (solid line with closed circles (black)), 1 hydrogen atom- (broken line with open circles (blue)) and 4 hydrogen atoms-trapped (broken line with squares (red)) $\Sigma 3(112)$ grain boundaries [39].	16
Figure 2.8	Minimum-energy path for carbon diffusion in α -Fe and the local structures of initial, intermediate, final, and transition states [9].	18
Figure 2.9	Molecular statics results for vacancy formation energy as a function of the distance from the grain boundary in Cu [42].	21
Figure 2.10	Examples of vacancy instability in Cu $\Sigma 9(1\bar{2}2)$ grain boundary. (a) Perfect grain boundary structure; (b) Unstable vacancy at boundary site 6 [42].	22
Figure 2.11	Possible migration path of He interstitial atom in the Fe $\Sigma 11$ grain boundary. Small sphere represents the He atom. Arrows indicate possible paths [65].	23

Figure 2.12	Diffusion coefficients of hydrogen atoms in bulk, on free surface and in a $\Sigma 5$ grain boundary. The activation energies for hydrogen diffusion in bulk, free surface, and grain boundary are 0.044 eV, 0.066 eV, and 0.31 eV, respectively [67].	24
Figure 2.13	Calculated and measured self-diffusion coefficients in a $\Sigma 9$ Cu grain boundary [42].	25
Figure 2.14	Phase diagram for bcc Fe and fcc Fe with different magnetic configurations [9].	27
Figure 2.15	Variation of average atomic volume and magnetic moment (MM) per Fe atom of the fcc structured Fe-Cu alloys against the Cu concentration [85].	30
Figure 2.16	Fragment of crystal and magnetic structure of γ -Fe for the AFMD magnetic ordering [73]. Carbon interstitial impurity in octahedral position is shown by dark (red) circle.	31
Figure 2.17	Schematic of the (a) Fe(001)-Ag(001) interface and the (b) Fe(110)-Ag(111) interface [88]. The cross symbols mark the high-symmetry sites with respect to the Ag plane for the successive Fe atom at interface. The layers around the interface are indexed by numbers.	32
Figure 2.18	Evolution of the atomic magnetic moment of the Fe atoms as a function of the position of the layer in the Fe(001) slab (black circles) and in the Au(001)-Fe(001) interface (red squares) [91].	33
Figure 2.19	Projected densities of the d states of individual Fe atoms in the Au(001)/Fe(001) interface. Fe_{surf} , Fe_{center} , and Fe_{int} denote the Fe atoms at the surface, in the center, and at the interface, respectively [91].	34

Figure 4.1	Sketch of the search paths for the minimum of a function (i.e. energy) using the steepest descent (left) and conjugate-gradient approach (right). In both cases, the search begins at point 1. The conjugate-gradient method converges faster [97].	41
Figure 4.2	Convergence test of the total energy with respect to energy cutoff.	44
Figure 4.3	Convergence test of the total energy with respect to k -point mesh for the conventional bcc Fe unit cell.	45
Figure 4.4	Convergence test of Nb cohesive energy with respect to supercell size.	46
Figure 5.1	(a) Side view of the $\Sigma 5$ (013) symmetrical tilt grain boundary. The lighter and darker circles represent Fe atoms in different (100) atomic planes. (b) Atomic structure of the boundary sites. The letters a , b , and c refer to different boundary positions. The superscript ($'$) indicates the symmetric position with respect to the (013) boundary plane. The subscript identifies different boundary unit cells of the $\Sigma 5$ (013) grain boundary.	56
Figure 5.2	Grain boundary energy as a function of distance between grain boundaries.	57
Figure 5.3	Binding energies for substitutional solutes at the $\Sigma 5$ (013) tilt grain boundary as a function of distance from the boundary plane; a , b , c , b' , and c' refer to the boundary sites as labeled in Figure 5.1.	58
Figure 5.4	Total grain boundary segregation of Nb as a function of temperature in $\Sigma 5$ grain boundary in Fe. The symbols are calculated according to Equation 5.3, while the line is the Langmuir-McLean fit.	59

Figure 5.5	(a) The average binding energies, and (b) the effective binding energies of solutes as a function of solute atomic volume. The dotted line indicates the atomic volume of Fe in the bcc lattice.	60
Figure 5.6	Valence electron density difference contour maps in the (100) plane for (a) Co-, and (b) Nb- segregated at boundary position a with respect to the non-segregated grain boundary (in units of $e/\text{\AA}^3$ with a contour spacing of $0.01 e/\text{\AA}^3$). The solid red and dashed blue lines indicate gains and losses in electron density, respectively.	62
Figure 5.7	Binding energies for a second solute atom segregating at (a) boundary position a , and (b) boundary position b when the same solute is already present at another boundary site. The square symbols indicate the binding energies of a single solute atom.	64
Figure 5.8	Pair interactions for (a) Nb, (b) Cr, (c) Cu, and (d) Si in the Fe bulk and at the $\Sigma 5$ (013) grain boundary.	66
Figure 5.9	Binding energies for the grain boundary with Nb segregating at (a) boundary position a , and (b) boundary position b when another solute (i.e. Mo, Ti, Mn, Cr, V, Cu, or Si) is already present at a neighboring site indicated by the second letter. The dotted line indicates the binding energies for a single Nb atom.	70
Figure 5.10	Site volume distribution in $\Sigma 5$ (36.9°), $\Sigma 29$ (43.6°) and $\Sigma 61$ (10.4°) grain boundaries.	72
Figure 5.11	Averaged atomic volume as a function of grain boundary misorientation angle. The bars indicate the maximum and the minimum atomic volume of the boundary sites.	73
Figure 6.1	Fe fcc lattice structure with AFMD magnetic configurations. Red and blue circles indicate spin-up and spin-down magnetic states. The letters o , p , q , w , e , and e' are used to label the different positions in the fcc bulk.	74

Figure 6.2	SQS-32 structure for fcc Fe lattice. The red and blue ball indicate spin-up and spin-down states.	75
Figure 6.3	(a) Side view of the Fe $\Sigma 5$ fcc grain boundaries with AFMD magnetic configurations. (b) Top view of the supercells. Red and blue circles indicate spin-up and spin-down magnetic states.	76
Figure 6.4	Various magnetic configurations vs. lattice constant in fcc Fe. The bcc ground state is set to be the reference (zero) state.	79
Figure 6.5	Magnetic moments for solute atoms in bcc and fcc Fe matrix. The x -axis is arranged in ascending order of atomic number.	80
Figure 6.6	Calculated partial density of states (DOS) of $3d$ -orbital for solutes in the bcc (left) and fcc (right) phases. The Fermi levels (E_F) are set to zero	82
Figure 6.7	Pair interactions for (a) Nb, (b) Cr, (c) Mn, (d) Ni, (e) Cu, and (f) Si in γ - and α -phase Fe matrix.	84
Figure 6.8	Binding energies for substitutional solutes at the $\Sigma 5$ fcc grain boundary as a function of distance from the boundary plane; a , b , c , b' , and c' refer to the boundary sites as labeled in Figure 6.3.	87
Figure 6.9	Volume distribution per periodic unit cell for $\Sigma 5$ grain boundaries in bcc and fcc Fe.	88
Figure 7.1	Structure of bcc-fcc interface with K-S orientation relationship. (a) AFMD and (b) SQS configuration for fcc. The white circles represent atoms in the bcc Fe grain, and the red (blue) circles indicate atoms in the fcc Fe grain with spin up (down) states.	92
Figure 7.2	bcc-fcc interface energy as a function of (a) the bcc grain size while the length of the fcc grain is fixed to 25.4 Å; and (b) the fcc grain size while the length of the bcc grain is fixed to 21.3 Å.	93

Figure 7.3	Magnetic moments of Fe atoms across the bcc-fcc interface.	95
Figure 7.4	Averaged site volume distribution across the bcc-fcc interface. The bars indicate the range of values of site volumes for Fe atoms with spin-up or spin-down states.	96
Figure 7.5	Relative energies for (a) Nb, and (b) Mn across the α - γ interface as a function of distance from the habit plane. The bars indicate the range of energies for the SQS simulations, where the replaced Fe atom has spin-up or spin-down states.	98
Figure 7.6	Relative energies for substitutional solutes across the bcc-fcc interface as a function of distance from the habit plane. The bars indicate the range of energy values, where the replaced Fe atom has spin-up or spin-down states. The fcc grain is described by the AFMD configuration.	99
Figure 7.7	Definition of the binding energy using linear interpolation from the bulk energies.	100
Figure 7.8	Binding energies for substitutional solutes at the bcc-fcc interface as a function of distance from the habit plane. The bars indicate the actual values of binding energies. The fcc grain is described by the AFMD configuration. The interface width is indicated by two dashed lines.	101
Figure 7.9	Relative binding energies of Nb at the bcc-fcc interface as a function of the site volume.	102
Figure 7.10	Calculated effective binding energies for selected alloying elements as a function of solute volume in bcc-fcc interface. The dotted line indicates the volume of Fe calculated from the first nearest neighbor distance in the bcc bulk Fe.	105
Figure 7.11	Calculated effective binding energies for selected alloying elements as a function of solute volume in bcc-fcc interface. The dotted line indicates the volume of Fe calculated from the first nearest neighbor distance in the bcc bulk Fe.	106
Figure 7.12	Illustrations of interaction profiles between solute atoms and bcc-fcc interface.	107

Figure 7.13	Pair interactions for (a) Nb, (b) Cr, and (c) Mn in bcc-fcc Fe interface. The first solute occupies its favorite position. The subscripts α and γ indicate solute atom occupies bcc α - or fcc γ -phase grain, respectively. The superscripts ‘1st’ and ‘2nd’ denote the first and the second substitutional solute atom, respectively. The arrow \uparrow (\downarrow) represents solute atom has spin-up (spin-down) state.	109
Figure 8.1	First-neighbor diffusion of the vacancy in bcc Fe. One vacancy locates in the center, and diffuses along the red line to the corner of the cubic cell (the corner atom diffuses into the centered vacancy). The calculated migration barrier for vacancy is also shown.	112
Figure 8.2	Relationship between $\bar{\alpha}$ and ΔM_{12} . The triangles denote the parameter $\bar{\alpha}$ is derived from experiments [169–172] and the line gives the model according to Equation 8.4.	114
Figure 8.3	An illustration of the different vacancy hops involved in the Le Claire nine-frequency model for the correlation factor for solute diffusion in Fe. X and V denote the solute atom and the vacancy, respectively.	115
Figure 8.4	Predicted temperature dependence of the calculated α -Fe self-, Mn, Mo, and Nb solute-diffusion coefficients vs. published experimental data [11, 48, 165, 170, 171, 174?–178].	117
Figure 8.5	The modified activation energies for Fe self-diffusion in bcc and fcc phase at different temperature.	121
Figure 8.6	Predicted temperature dependence of the Fe-self diffusion coefficients vs. published experimental data in bcc and fcc [174, 175].	122
Figure 8.7	Vacancy formation energies at different sites of $\Sigma 5$ (013) grain boundaries in α -Fe. The dotted red line indicates the value in the bulk lattice.	123

Figure 8.8	Vacancy-solute binding energies at $\Sigma 5$ (013) grain boundaries and bulk in α -Fe. Vacancy segregates at (a) boundary a_0 , and (b) boundary b position. The capital letters X refer to the solute and V refer to the vacancy . . .	124
Figure 8.9	Predicted temperature dependence of the calculated Nb, Mo, Mn, and Fe-self diffusion coefficients at grain boundaries.	126
Figure 8.10	Vacancy formation energies as a function of distance from the habit plane. The bars indicate the actual vacancy formation energies, where Fe atom has spin-up or spin-down states.	129
Figure 8.11	Illustration of various jump paths in the bcc-fcc interface. Blue and red circles indicate fcc Fe atoms with spin-down and spin-up magnetic state, while white circles represent bcc Fe atoms.	129

List of Symbols

A_S	Area of the boundary or interface
a_l	Lattice constant
\vec{a}	Acceleration in the Newton's second law
a, b, c, b', c'	Different positions in boundaries
C_{11}, C_{12}, C_{44}	Elastic constants in the bulk
c_{bulk}	Solute concentration in the bulk
c_{gb}^i	Solute concentration at the boundary site i
c_{gb}	Total solute concentration at the grain boundary
c_{gb}^0	Fraction of boundary sites with favourable binding
c_{int}^i	Solute concentration at the bcc-fcc interface site i
c_{int}	Total solute concentration at the bcc-fcc interface
c_{int}^0	Fraction of bcc-fcc interface sites with favourable binding
c_v^{eq}	Equilibrium vacancy concentration
d_1, d_2, d_3	First nearest neighbor distance in the fcc bulk with AFMD state
$d_{oe}, d_{oe'}$	Second nearest neighbor distance in the fcc bulk with AFMD state

d_{gs}	Grain size
d_{α}	bcc grain size
d_{γ}	fcc grain size
D	Diffusion coefficient
D_0	Pre-factor in the Arrhenius expression for diffusion coefficient
D_{app}	Apparent diffusion coefficient
D_b	Grain boundary diffusivity
D_I	bcc-fcc interface diffusivity
D_l	Bulk diffusivity
D_l^{α}	bcc bulk diffusivity
D_l^{γ}	fcc bulk diffusivity
E_b	Solute-vacancy binding energy
E_{cut}	Cut-off energy
E_m	Migration energy
E_{f_2}	Correlation energy
E_v	Vacancy formation energy
E_X	Total energy of the supercell with one solute
E_{X+Y}	Total energy of the supercell with two solute atoms
E_{\square}	Total energies of the supercell with one vacancy
$E_{\square+X}$	Total energy of the supercell with one vacancy and one solute
E_{rel}^i	Relative energy of the solute at the interface site i
E_{seg}^i	Segregation energy of the solute at the boundary site i

E_{gb}	Total energy of the supercell with grain boundaries
E_{X+gb}^i	Total energy of the supercell with grain boundaries and one solute atom segregated at the boundary site i
E_{eff}	Effective solute-solute interaction
E_F	Fermi energy
\vec{F}	Force
f_2	Correlation factor
F_i	Fraction of the grain boundary or interface sites that have binding E_{seg}^i
\vec{G}	Vector of the reciprocal lattice
$H_{i,j}$	Hessian matrix
$H_{i,j}^m$	Mass-weighted Hessian matrix
\hat{H}	Hamiltonian operator
$\hat{H}_H[\rho(\vec{r})]$	Electrostatic interactions in Kohn-Sham equations
J_1	Exchange parameter in the first coordinate shell
\vec{k}	Momentum
K	Bulk modulus
l_i	Supercell dimension in i direction
M	Interface or grain boundary mobility
m_a^i	Atomic mass
ΔM_{12}	Sum of the change in the local magnetic moments induced on the Fe atoms in the first and second neighbor neighbors of an solute atom

MM	Local magnetic moments
N	Number of atoms in the supercell
$N_{itermax}$	Total number of vacancy jumps in the KMC simulations
o, p, q, w, e, e'	Different positions in the fcc bulk
Q_0	Activation energy at 0K
Q_a	Activation energy
Q_P	Activation energy in paramagnetic state
R_N	Summation of the jump rate
$\langle r^2(t) \rangle$	Mean square displacement of the diffusing solute atoms during time t
\vec{r}_i	Electron coordinates
\vec{R}_i	Nuclei coordinates
$s(T)$	Reduced magnetization at given temperature T
S_v	Vacancy formation entropy
T_c	Curie temperature
T_m	Equilibrium melting temperature
$T_{\alpha-\gamma}$	Ferrite-austenite transition temperature
$\hat{T}[\rho(\vec{r})]$	Non-interacting kinetic energy in Kohn-Sham equations
$\hat{U}_{ext}[\rho(\vec{r})]$	Potential energy in Kohn-Sham equations
u_{rand}	Random number in the KMC simulation
$\hat{V}_{xc}[\rho(\vec{r})]$	Exchange-correlation energy in Kohn-Sham equations
x_{rand}	Random number in the KMC simulation

α	Ferrite
$\bar{\alpha}$	Species-dependent parameter that quantifies the dependence of Q_a magnetization
α_{el}, γ_{el}	Parameters in Eshelby elasticity model
γ	Austenite
Γ_j	Jump frequency to site j
Γ_X	Solute-vacancy exchange jump frequency
δ	Effective thickness of the grain boundary
δ_α	Effective thickness of the interface in the bcc grain
δ_γ	Effective thickness of the interface in the fcc grain
ε_i	Eigenvalues in mass-weighted Hessian matrix
θ	Misorientation angle
ν_0	Attempt frequency
ν_i	Frequencies of the pure Fe system
ν_i^{eq}	Frequencies of the equilibrium configuration with one vacancy
ν_i^{sp}	Frequencies of the saddle-point configuration
ρ	Electron charge density
σ	Interface or grain boundary energy
τ_{kmc}	Residence time associated with the KMC step
$\Psi(\vec{R}, \vec{r}^\dagger)$	Wave functions in the many-body Schrödinger equation
$\Phi_i(\vec{r})$	Wave functions in Kohn-Sham equations
$\langle \bar{\prod}_{l,m} \rangle_{SQS}$	Correlation function for SQS, where $\{l, m\}$ are the “interaction parameters” of figures

Ω_0 Primitive cell volume

List of Abbreviations

AFM	Anti-ferromagnetic
AFMD	Double-layer anti-ferromagnetic
AHSS	Advanced high strength steels
bcc	Body-centered cubic
CE	Cluster Expansions
CPA	Coherent potential approximation
CG	Conjugate-gradient
CLS	Coincident site lattice
DFT	Density functional theory
DOS	Density of states
DP	Dual phase
EAM	Embedded atom method
ECIs	Effective cluster interactions
fcc	Face-centered cubic
FM	Ferromagnetic
GBs	Grain boundaries

GGA	Generalized gradient approximation
JMAK	Johnson-Mehl-Avrami-Kolmogorov
LDA	Local density approximation
MS	Molecular statics
MD	Molecular dynamics
KMC	kinetic Monte Carlo
K-S	Kurdjumov and Sachs
NC	Non-collinear
NEB	Nudged elastic band
NM	Non-magnetic
NN	Nearest-neighbor
N-W	Nishiyama and Wassermann
PAW	Projector augmented wave
PBE	Perdew, Burke, and Enzerhof
PM	Paramagnetic
SQS	Special quasi-random structure
TMs	Transition metals
TST	Transition state theory
TRIP	Transformation induced plasticity

Acknowledgements

First of all, I would like to express my sincere gratitude to my supervisor Dr. Matthias Miltzer for providing continuous support and wisdom throughout my studies at UBC. His diligence, self-discipline and enthusiasm always inspire me and set me a good example to follow for the rest of my life.

Secondly, I would like to give a special thank to Dr. Ilya Elfimov. Ilya has consistently supported and actively contributed to all my work. He also spent many extra hours to provide professional advices for my graduate studies.

I would also like to extend my thanks to my committee members, Dr. Chad Sinclair, Dr. Jörg Rottler and Dr. Warren Poole for their constructive criticism and valuable advice on my research.

I had a pleasure of spending wonderful time with colleagues and friends at the Microstructural Engineering group at the Department of Materials Engineering. In particular, I would like to thank Benqiang, Liam, Tao, Sina, and Tegar for their stimulating discussions.

I would like to thank the Natural Sciences and Engineering Research Council (NSERC) of Canada for the financial support of this work, as well as WestGrid and Compute/Calcul Canada for computational resources.

I want to thank Xiao, who appeared in my life in the dusk of the Ph.D. program and made it so much brighter

Above all, I would like to thank my parents for their love, unconditional support, and tireless dedication throughout my life.

Chapter 1

Introduction

As the demand to produce new families of low-carbon high-strength steels increases, advancing knowledge of the physical mechanisms of microstructure evolution becomes increasingly important in order to develop steels with desired properties. These steels are so-called advanced high-strength steels (AHSS) and have improved properties. AHSS include dual phase (DP) steel, transformation induced plasticity (TRIP) steel, complex phase steel and martensitic steel. The tensile strengths range from 500 to 1900 MPa. These steels are superior in strength and ductility combination, and thus facilitate the energy absorption during impact and ensure safety when reducing weight. As a result, with appropriate manufacturing techniques, AHSS offer great opportunities for designing inexpensive, safe and fuel-efficient vehicles by reduction of product weight, enhancement of crash performance, and improvement of car fuel economy.

Using existing facilities to produce AHSS one is required to have an increased alloying content in terms of substitutional elements, such as V, Mn, Nb, Mo, Cr, Si, and Ti. Due to the presence of a high density of structural imperfections at interphase boundaries, these solute atoms are more likely to accumulate at these interfaces. It is believed that solute interact with the migrating interface and this is a basic phenomenon effectively used during industrial processing to tailor the phase transformation kinetics.

In order to aid the alloy design, great effort has been made to develop

knowledge-based process models for the steel industry in the last decades [1, 2]. However, these process models require numerous empirical parameters that are typically determined from time-consuming laboratory experiments. In addition, important physical properties in terms of the solute-interface interaction are still essentially unexplored and have become an important research area.

By analyzing the physical mechanisms of microstructure evolution, it is known that the presence of alloying elements can drastically reduce the migration rate of interface in pure metals. For example, substitutional alloying elements (e.g., Nb, Mo) can significantly retard recrystallization and the austenite-ferrite phase transformation in steels. This retardation is known as the solute drag effect, which plays a crucial role in tailoring the material properties [3, 4]. In Figure 1.1, the interface velocity as a function of the driving pressure is shown. For a given driving pressure, the velocity decreases with the increase in solute concentration [5]. At sufficiently high driving pressures, the interface velocity approaches the intrinsic mobility of the system without solute elements.

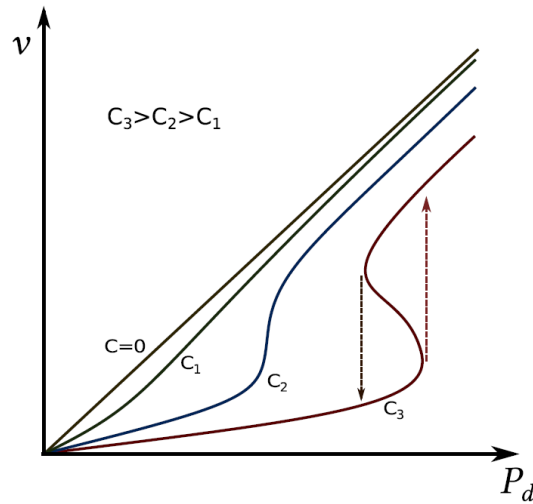


Figure 1.1: Variation of the interface velocity (ν) versus the applied driving pressure (P_d) for systems with different solute concentrations (C_i , $i = 1, 2, 3$) [5].

The transition between high and low interface velocity regimes occurs for higher solute concentrations. When the driving pressure increases in the low velocity regime, the interface breaks up from the solute atoms at a critical velocity. While at high velocity regime, when the driving pressure decreases, at a critical velocity, the solute atoms can significantly reduce the velocity of the interface. The transition velocity is not the same for the two conditions, and thus there can be a jump from high to low velocity regime as shown in Figure 1.1.

The solute drag effect has been studied for several decades. Lücke and Detert developed the first quantitative theory to explain the influence of small amounts of impurities upon recrystallization [6]. Then a continuum model proposed by Cahn [7] and followed by Hillert [8], formed the basis of the current understanding of the phenomenon. In these approaches, the two solute drag parameters, i.e. binding energy (E_{seg}) and trans-interface diffusivity (D), and the intrinsic mobility (M) are introduced to describe the solute-interface interactions. It should be emphasized that these approaches are phenomenological models used on the macroscale. When describing experimental observations, the intrinsic mobility and two solute drag parameters are essentially employed as fitting parameters. Currently, intrinsic mobility and solute drag parameters cannot be determined exactly by independent experimental studies. To improve the predictive capabilities of these models, new theoretical models and simulation tools with a minimum of empirical parameters are required.

Recent progress in Computational Materials Science has provided tremendous opportunities to formulate models containing fundamental information on the basic atomic mechanisms of microstructure evolution that can be implemented across different length and time scales [4]. This approach, also called multi-scale modeling, can connect parameters from the atomistic scale to the macroscopic scale of an industrial product. The multi-scale studies start from atomistic simulations, e.g. density functional theory (DFT), which provide fundamental properties based on the knowledge at the atomistic level. The solute drag parameters, i.e. the binding energy and trans-interface diffusivity can be quantitatively determined by the DFT

simulations.

DFT is based on the Hohenberg-Kohn theorem, in which the electron density is treated as the fundamental variable. Hohenberg and Kohn proved that the total energy of a many-body system is a unique functional of the electron density and has a minimum corresponding to the ground state density. Within the framework of Kohn and Sham, the many-body problem of interacting electrons in a static external potential is reduced to a problem of non-interacting electrons moving in an effective potential, which can be applied to a system containing in principle any number of particles. The connection between true many body and auxiliary single particle systems is made through the exchange-correlation potential for which there are no known analytical expressions. Fortunately, the widely used approximation, i.e. the Generalized Gradient approximation (GGA), gives remarkably accurate results. For example, the calculated lattice constant for bcc Fe differs from the experimental result by less than 1% [9]. Note that the DFT calculations are limited to $T = 0\text{K}$. Nevertheless, it has been shown to be a very powerful theoretical tool to obtain reliable quantitative information such as binding energies of solute at interfaces and activation energies for solute diffusion [9–11].

In grain boundaries and interfaces, the activation energies of the solutes depend on the boundary positions. Consequently, there are a multiple of jump rates. To investigate solute diffusivities, the kinetic Monte Carlo (KMC) approach is employed. KMC methods rely on probabilities of events, which can effectively overcome the time and length scale limitation, and determine the solute diffusion in a large system. The probabilities are obtained based on the detailed input from DFT calculations.

The solute drag parameters influence the overall phase transformation as observed on the industrial line. The motivation of the present work is to provide more insight into the atomistic mechanisms of the solute-interface interaction and determine the important solute drag parameters by using atomistic simulations, i.e. DFT and KMC. These values can then be used in the process model with a greatly reduced number of fitting parameters. The combination of atomistic simulations with process model will provide a

more reliable and efficient way to predict trends on how alloying additions affect the phase transformation for advanced steels [12].

Chapter 2

Literature Review

2.1 Introduction

In this review, the focus is on the atomistic simulations of solute drag parameters, i.e. the binding energy (E_{seg}) and the trans-interface diffusivity (D). We first review the current results of solute segregation on grain boundaries in Fe with emphasis on atomistic simulations approaches, e.g. density functional theory and molecular dynamics simulations. The self- and solute-diffusion in the bulk and grain boundaries are then discussed. In the latter part of this chapter, atomistic studies based on the density functional theory for heterophase interfaces and the magnetic ground states of fcc Fe are reviewed.

2.2 Solute Segregation on Grain Boundaries

2.2.1 Simulations of Grain Boundary Segregation

A grain boundary is the interface between two grains (crystals), which are critical for many properties of materials. For examples, grain boundaries are well known to act as sinks for point defects, preferential sites for nucleation of secondary phases and offer the possibility for fast diffusion [13]. Modeling and simulation of segregation to grain boundaries at the atomic scale can

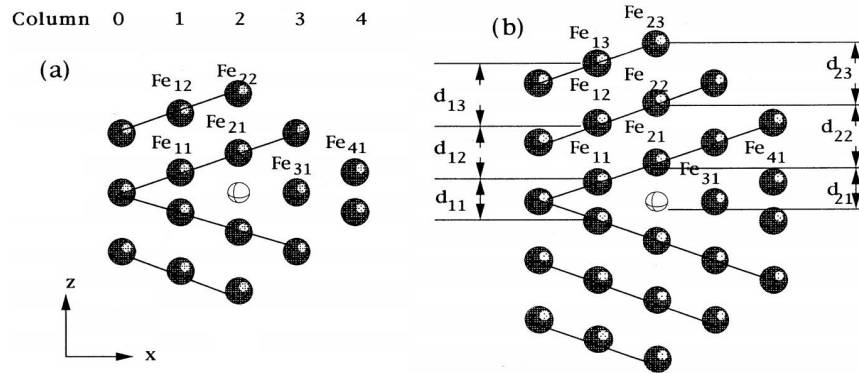


Figure 2.1: Side view of the Fe $\Sigma 3$ (111) grain boundary [15]. (a) Cluster of 53 atoms and (b) cluster of 91 atoms. The open circle represents solute atom.

provide valuable insight into segregation processes. In the past decades, a large amount of simulation work has been devoted to the structure of high-angle grain boundaries in Fe, especially for special boundaries, such as symmetrical tilt boundaries and pure twist boundaries [10, 14–20], in which the grain boundary is treated as a perfect planar interface between two crystals that have different orientations. Among all these studies, symmetrical low Σ boundaries as defined in the coincident site lattice (CSL) theory [21, 22], were primarily investigated.

First-principles calculations are often used to study the solute segregation behavior at grain boundaries and their influence on grain boundary cohesion. These kinds of simulations for grain boundaries in bcc Fe were pioneered by Freeman and Olson [10, 14–17]. In their early studies, a cluster model (i.e. non-periodic structure) containing 6~10 atoms was employed to simulate the $\Sigma 3$ (111) grain boundary in Fe [14]. Soon after it was realized that when impurities (e.g. phosphorus) are introduced, the elastic lattice distortions exceed the dimensions of the cluster. In the subsequent calculations, they expanded the cluster size up to 91 atoms for more realistic simulations [16, 17]. Figure 2.1 shows the cluster model for the Fe $\Sigma 3$ (111) grain boundary containing 53 and 91 atoms, respectively. In addition, other grain boundaries, for example $\Sigma 5$ (013) grain boundaries, were also

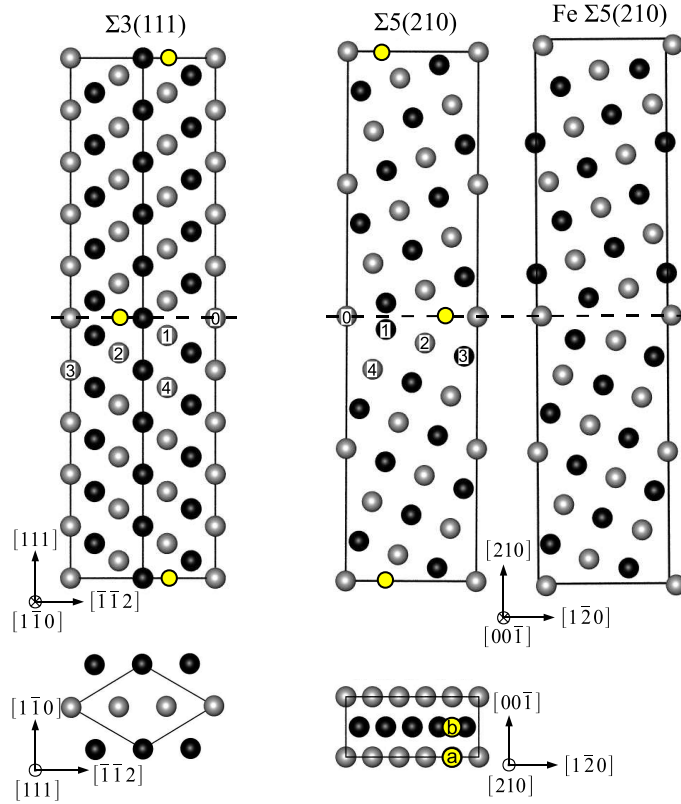


Figure 2.2: Side view of the Fe $\Sigma 3$ (111) and $\Sigma 5$ (210) grain boundaries [25]. The lighter and darker circles mark the atoms belonging to two different planes. The interstitial positions at the grain boundary are indicated by the yellow circles. The substitutional positions in different grain layers are labeled by the numbers. Lower panels show top view of the supercells taken in the cross-section plane passing through the grain boundary (broken line).

investigated [23, 24]. In these studies, a cluster model containing up to 196 atoms was used.

The cluster approach often suffers from finite size effects even when the cell consists of several hundred atoms. As a result, the calculated results may contain significant errors [15]. This casts some doubts on the applicability of these models. To overcome this problem, a supercell approach with periodic

boundary condition is utilized in modern studies of the grain boundaries and interfaces.

In the supercell model, the grain boundary structure is created by rotating two grains around the common axis by misorientation angle θ . In order to maintain the periodic boundary conditions, each supercell has to contain two identical, reversely oriented grain boundaries. The typical structures of $\Sigma 3$ (111) and $\Sigma 5$ (210) grain boundaries are shown in Figure 2.2 [25]. By now, there have been a considerable number of studies dedicated to these boundaries, and encouraging results have been obtained [25–27]. However, it should be emphasized that all these studies are limited to these special low Σ grain boundaries, i.e. $\Sigma 3$, $\Sigma 5$, and very recently, $\Sigma 11$ grain boundaries [25, 27, 28]. The higher Σ and low angle grain boundaries have never been considered based on the framework of first-principle calculations due to the expensive computational costs.

To access those general high Σ grain boundaries, molecular dynamics (MD) simulations are a viable approach. These simulations are much less computationally expensive than first-principles calculations, but are limited by the accuracy or availability of interatomic potentials. Nonetheless, MD simulations are increasingly being used to study grain boundary segregation.

Recently, a series of MD calculations have been performed to systematically study $\langle 100 \rangle$, $\langle 110 \rangle$, and $\langle 111 \rangle$ symmetric grain boundaries [18–20]. These boundaries not only contain several low-order coincident site lattice (CSL) grain boundaries (e.g., $\Sigma 3$, $\Sigma 5$, $\Sigma 9$, and $\Sigma 11$ boundaries), but also include more general high Σ boundaries. In these studies, the grain boundaries are analyzed by characterizing the local atomic structure as structural units. One important finding is that the high Σ grain boundaries can be characterized by structural units from two neighboring low Σ boundaries.

Figure 2.3 shows an example of the $\langle 100 \rangle$ symmetric tilt grain boundary system, where the $\Sigma 29(730)$ boundary is a combination of structural units from the two $\Sigma 5$ boundaries [19]. The structural units for the $\Sigma 5(310)$ and $\Sigma 5(210)$ grain boundaries are labeled as B and C, respectively. In a similar manner, the $\Sigma 17$ boundary is a combination of the $\Sigma 5$ structural units C

<100> Symmetric Tilt Grain Boundary Structure

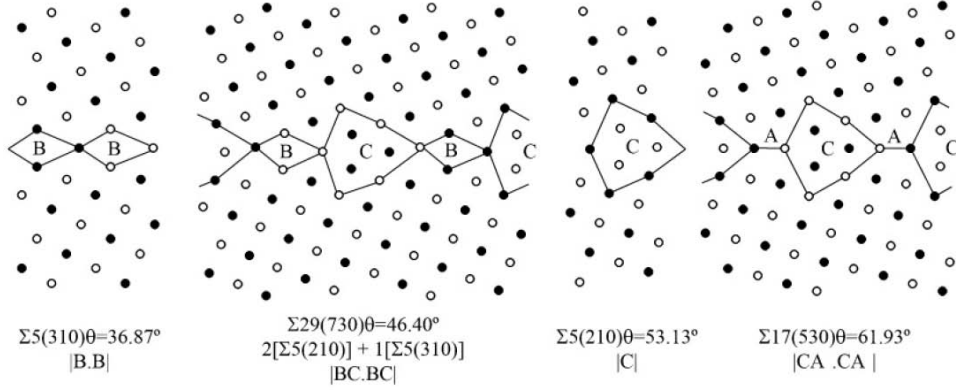


Figure 2.3: < 100 > symmetric tilt grain boundary structures with structural units outlined for the $\Sigma 5(210)$, $\Sigma 29(730)$, $\Sigma 5(310)$ and $\Sigma 17(530)$ boundaries [19]. Black and white denote atoms on different 100 planes. The different structural units are labeled as A, B, and C.

and structural units of the bulk lattice, i.e. A. This conclusion is general and holds for pure tilt and twist boundary types with low index rotation axes, which implies that the results obtained from special low Σ grain boundaries can be extended to more general high Σ grain boundaries.

The effect of temperature on the grain boundary structures was recently studied by Asta's group [29, 30]. With MD simulations, they characterized multiple grain boundary phases by structure and atomic densities in the grain boundary core region. As shown in Figure 2.4, phase transformations are found in the $\Sigma 5(210)$ grain boundary. During isothermal anneals at temperatures below 1050 K, the grain boundary transforms into its thermodynamically stable phase at low temperatures, i.e. the split kites (labeled in red color as shown in Figure 2.4). On the contrary, when the boundary with split kites is heated up to 1100 K, its structure transforms to filled kites (labeled in blue color as shown in Figure 2.4). Frolov *et al.* suggested that this first-order phase transformation was induced by point defects, where the absorption of point defects strongly modified the grain

boundary structure, and finally resulted in structural transformations.

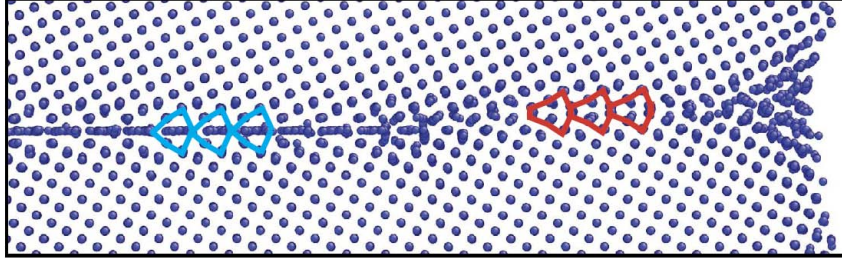


Figure 2.4: MD simulation of the Cu $\Sigma 5(210)$ grain boundary at 800K allowing variations in grain boundary density. The boundary undergoes a first-order phase transformation from filled kites (labeled in blue color) to split kites (labeled in red color) nucleating and growing from the surface [29].

2.2.2 Binding Energy

The binding energy of a solute with a grain boundary (also called segregation energy) determines thermodynamically the solute segregation behavior. Within the framework of atomistic calculations, the binding energy is defined as the energy difference of the system when solute atoms moved from the bulk to the grain boundaries, which can be expressed as:

$$E_{seg} = E_{X,gb} - E_{X,bulk} \quad (2.1)$$

where $E_{X,gb}$ and $E_{X,bulk}$ are the total energies of the supercell with one X solute at the grain boundary or in the bulk. Negative E_{seg} means that the impurity segregation at the grain boundary position is favorable. In a series of first-principles calculations, the binding energies of various non-metallic elements (i.e. hydrogen, boron, carbon, nitrogen, oxygen, phosphorous, and sulfur) with special grain boundaries have been studied. Table 2.1 summarizes these results.

Table 2.1 demonstrates that: (1) In general these elements prefer to segregate at the interstitial boundary positions independent of the boundary types. (2) For a given grain boundary, the binding energy varies significantly

Table 2.1: Binding energies (in eV) of various non-metallic elements with special grain boundaries.

	Interstitial Position				Substitutional Position	
	$\Sigma 3(111)$	$\Sigma 3(112)$	$\Sigma 5(012)$	$\Sigma 5(013)$	$\Sigma 3(111)$	$\Sigma 5(012)$
H	-0.45 [31]	-0.34 [32]	-	-0.3 [33]	-	-
B	-2.0 [27]	-	-3.1 [25]	-	0.4 [27]	-1.9 [26]
C	-1.0 [27]	-	-1.0 [27]	-1.8 [27]	0.5 [27]	-2.4 [27]
N	-0.1 [25]	-	-1.1 [25]	-	0.4 [27]	-2.0 [27]
O	-	-	-1.9 [27]	-	-	-1.8 [27]
S	-3.1 [27]	-	-5.0 [27]	-	-0.2~-1.4 [27, 34]	-1.6 [27]
P	-3.2 [35]	-	-4.5 [35]	-	-0.1 [35]	-1.0 [35]

for different impurities. For example, the binding energy of interstitial phosphorous with the $\Sigma 3$ grain boundary is -3.2 eV, while it is an order of magnitude smaller for nitrogen. (3) The binding energies at the $\Sigma 5(012)$ grain boundary are larger (absolute value) than $\Sigma 3(111)$ grain boundaries. At the $\Sigma 5(012)$ grain boundary, the binding energies are distinctly negative for all impurities in interstitial and substitutional sites, while they are positive, i.e. repulsive for boron, carbon and nitrogen at substitutional positions in the $\Sigma 3(111)$ grain boundaries. (4) The binding energy depends on the boundary sites. Figure 2.5 shows the variation of binding energies as a function of the distance from the center of the boundary plane in a $\Sigma 3(111)$ grain boundary [34]. It is clear that at different boundary sites, the binding energy of sulfur varies from -0.2 eV to -1.4 eV. These variations are suggested to be attributed to the local-arrangement of the atoms at the grain boundary [34, 35].

In addition, Figure 2.5 also shows that the binding energy decreases quickly when sulfur moves into the interior of the grain. Similar results were also obtained by Solanki *et al.*, who carried out molecular dynamics

calculations for a more general high-angle grain boundary [36]. In their studies, 75 sites within 15 Å of the $\Sigma 13$ (320) grain boundary were selected to calculate the binding energy of phosphorus. Their results revealed that the distance associated with the binding energy approaching the bulk value was about 5 Å. In other words, the influence of the grain boundary on the solutes was short ranged, and limited to about 4~5 atomic layers.

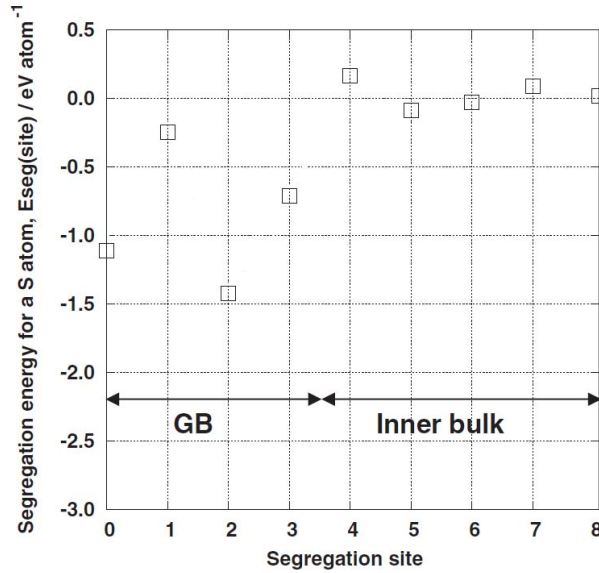


Figure 2.5: DFT simulations for segregation energies as a function of segregation site for the Fe $\Sigma 3$ (111) grain boundary with sulfur at the substitutional site [34].

The binding energies as a function of solute concentration were investigated recently. Using DFT, Yamaguchi systematically increased the number of solute atoms (N_P) in the supercell, where $N_P \leq 8$ [35], and determined the most stable configurations of solute atoms for each concentration. Figure 2.6 shows the example of binding energies of phosphorous. The total binding energy ($E_{tot}^{seg} = \sum_i^{N_P} (E_i^{seg})$) of N_P phosphorous atoms is denoted by lines and points (left tick mark). The columns indicate binding energy (E^{seg}) of the additional phosphorous atoms (right tick mark). One can see that in the range of $N_P = 1$ to 4, E^{seg} is roughly constant and

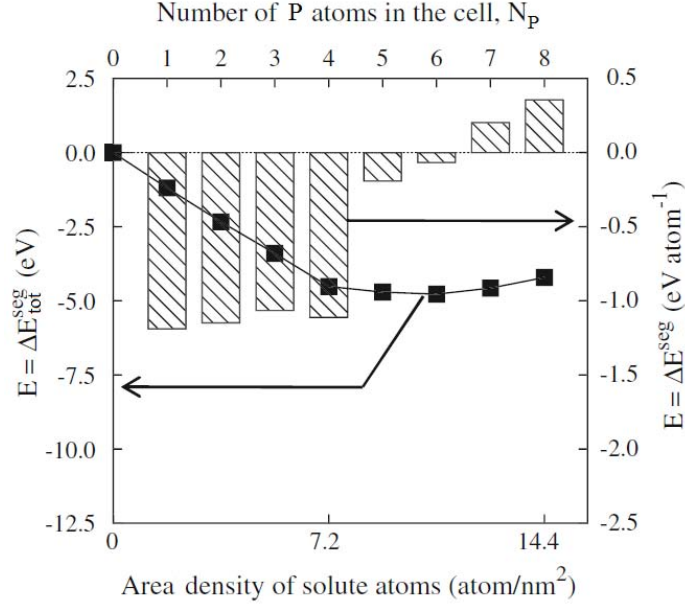


Figure 2.6: Calculated binding energies of phosphorous with varying the segregation concentration in the $\Sigma 3$ (111) grain boundary in Fe [35].

the total binding energy increases continuously. This indicates that the interaction between solute atoms is weak. Afterwards the repulsion between the segregated solute atoms becomes more pronounced and at $N_P = 7$, the incremental segregation energy (E^{seg}) is positive, i.e. the boundary sites are no longer favorable for P segregation. As a result, the segregation approaches saturation.

2.2.3 Effects of Solute on Grain Boundary Properties

Solute segregation at grain boundaries can significantly influence the mechanical properties of a material through the embrittlement effect. Some impurities, for example hydrogen, can strongly reduce the grain boundary cohesion, resulting in grain boundary embrittlement. Whereas other impurities, e.g. carbon, can increase grain boundary cohesion [4]. Despite of the use of relatively small supercells with simple $\Sigma 3$ or $\Sigma 5$ grain boundaries,

first-principles calculations have been proved to be very useful in predicting the embrittlement effect of various impurities.

Within the atomistic simulation framework, Rice and Wang postulated an approach to determine the strengthening or embrittling effect of an impurity on grain boundaries [37]. In this method, the key quantity that determines the solute-induced embrittlement is the strengthening energy, which is defined as the difference between the binding energies of the solute elements to the grain boundary (E_{seg}) and to the surface (E_{sur}). If the elements have a stronger binding to the surface than to the grain boundaries, it is expected that segregation of such elements causes grain boundary embrittlement. Otherwise, they are grain boundary strengthening elements [37]. Based on this criterion, a number of first-principles calculations have been conducted to study the effects of various solutes on grain boundaries in bcc Fe [27, 38, 39]. The results can be summarized as follows: hydrogen, oxygen, phosphorous, and sulfur act as embrittlers at grain boundary interstitial sites. Carbon and nitrogen increase the grain boundary cohesion, and are expected to be grain boundary strengthening elements. At different occupation sites, boron can either increase or decrease the grain boundary cohesion in Fe.

Using DFT, Momida *et al.* calculated the energy-strain curves of $\Sigma 3(112)$ grain boundaries with and without interstitial hydrogen [39]. In Figure 2.7, the energy difference is defined as the work of fracture, which can be calculated as the difference between the grain boundary energy and two fractured-surface energies. It is evident that the work of fracture decreases with increasing number of hydrogen, indicating that hydrogen is a grain-boundary embrittler.

To analyze these grain boundary weakening/strengthening phenomenons and elucidate the physical mechanisms of the impurity effects, electronic structure, charge density, excess volume, etc. have been extensively studied, and two major findings have been identified, i.e. contributions from chemical effects, and contributions from size effects.

In early studies, based on the charge density analysis, Freeman *et al.* reported that the chemical bonding of boron and carbon with iron atoms

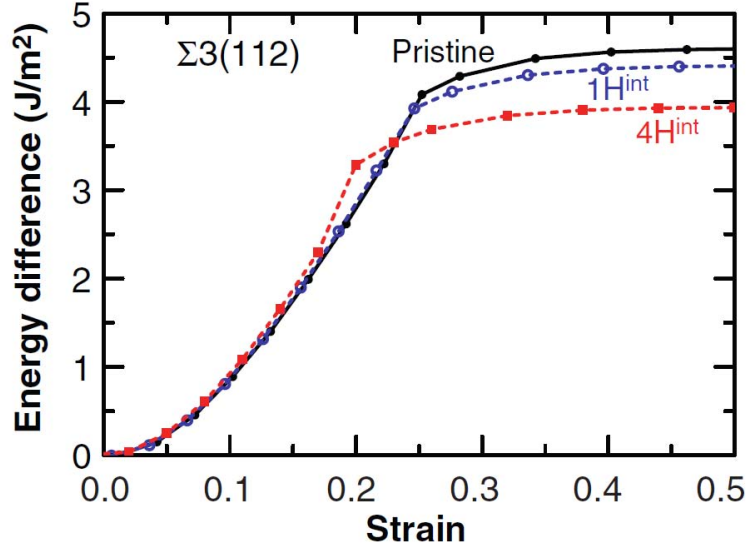


Figure 2.7: Results of energy difference relative to the equilibrium vs. uniaxial tensile strain for the pristine (solid line with closed circles (black)), 1 hydrogen atom- (broken line with open circles (blue)) and 4 hydrogen atoms-trapped (broken line with squares (red)) $\Sigma 3(112)$ grain boundaries [39].

at the grain boundary was strong, whereas it was dramatically weak for phosphorous and sulfur [14–17]. Similar results were also obtained by Juan *et al.* [33]. They found that when hydrogen or sulfur was present at the boundary site, all neighboring Fe-Fe bonds were weakened, which gives rise to grain boundary embrittlement. In these studies chemical bonding characteristic is concluded to be the key factor determining the embrittling or cohesion behavior of a segregated impurity at Fe grain boundaries.

In subsequent studies, Braithwaite *et al.* investigated the role of boron, nitrogen, and oxygen impurities at a $\Sigma 5$ grain boundary [38]. In disagreement with the chemical bonding proposal, they found no significant covalent bonding between the impurity and neighboring Fe atoms. This suggests that the grain boundary cohesion is simply related to the size of the impurity atom rather than the chemical bonding.

Recently, by separating the contributions from solute size and chemical

bonding, Wachowicz *et al.* pointed out that both chemical bonding and solute size can influence the grain boundary weakening/strengthening properties [25–27]. In their studies, the contributions from solute size tend to weaken the grain boundary cohesion, while the contribution from chemical bonding can either enhance or decrease the grain boundary cohesion depending on the species. Consequently, cohesion at the grain boundary is increased when large strengthening chemical contribution dominates. Such conclusions were later supported by Kiejna *et al.*, who systemically investigated the effects of several impurities (B, C, P, N, O, and S) on structure, energetic and mechanical properties of $\Sigma 5$ grain boundaries [27].

2.3 Solute Diffusion in Grain Boundaries

2.3.1 Overview

Interface diffusion controls the rates of many processes in materials at elevated temperatures, such as phase transformations, grain growth, and solid-state reactions that makes it a technologically important topic [3, 4, 40]. Quantification of solute grain boundary diffusion is therefore important to estimate and control the microstructure evolution. Unfortunately, due to the narrow width of grain boundary regions and the small amount of atoms involved in the diffusion process, its experimental measurement and determination is rather challenging. Thus, the understanding of basics of solute grain boundary diffusion is still limited. Recently, significant progress has been achieved through atomistic computer simulations [9, 11, 41–43], which has enabled a more detailed understanding of those diffusion processes.

2.3.2 Solute Diffusion in α -Fe

Before considering grain boundary diffusion, we first briefly review recent first-principle results for bulk diffusion. This is because: first, in recent years first-principle methods have been applied extensively in calculations of self- and solute-diffusivities in bulk α -Fe. Second, this provides a verification of

earlier intuitive atomistic models of diffusion and solute-interaction models, and it also provides an opportunity for a deeper understanding of the atomistic processes.

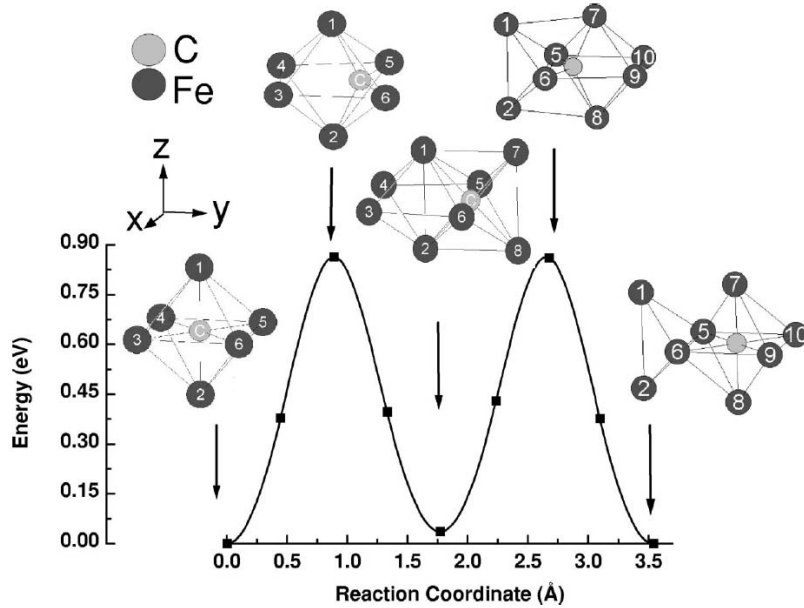


Figure 2.8: Minimum-energy path for carbon diffusion in α -Fe and the local structures of initial, intermediate, final, and transition states [9].

In previous studies, defect formation energies, defect-solute interaction energies and diffusion activation energies in Fe were systematic studied for a variety of impurities. Jiang *et al.* [9] used the nudged elastic band (NEB) approach in DFT simulations to investigate the activation energy of bulk diffusion of carbon in α -Fe. Figure 2.8 shows the minimum-energy path for carbon diffusion in α -Fe and the local structures of initial, intermediate, final, and transition states. The calculation results identify octahedral sites as the lowest energy position for carbon. The diffusion occurs via tetrahedral sites with the barrier of 0.86 eV, which agrees well with the experimental value of 0.87 eV [44]. In addition, the pre-exponential factor D_0 is also calculated by constructing and diagonalizing the Hessian matrix

Table 2.2: Calculated activation energies of fully ordered ferromagnetic state (Q_0) and pre-factor (D_0) in α -Fe vs. experimental data.¹

	Q_0 (eV)		D_0 (cm ² /s)	
	<i>DFT</i>	<i>Exp.</i>	<i>DFT</i>	<i>Exp.</i>
W	2.80 [11]	3.12±0.28 [47]	1.40 [11]	1.60 [48]
Mo	2.60 [11]	2.48 [49]	0.63 [11]	0.57 [50]
Cu	2.55 [51]	2.56 [52]		
Ni	2.71 [53]	2.68 [54]		
Cr	2.77 [55]	3.06±0.07 [47]		
Al	2.47 [56]	2.55 [57]		
C ²	0.86 [9]	0.87 [44]	1.44×10 ⁻³ [9]	1.67×10 ⁻³ [58]
H ²	0.10 [46]	0.14 [59]	1.37×10 ⁻³ [46]	1.40×10 ⁻³ [59]

¹ The model systems employed by above DFT calculations contain 54 or 128 atoms in the supercell, which corresponds to impurity concentration of 1.85% or 0.78%.

² H and C diffuse via interstitial sites

based on the frozen phonon approach [45]. Ramunni *et al.* [46] used the same approach to calculate the coefficient of interstitial hydrogen diffusion. The calculated diffusivity was found to be in good agreement with experimental data (see Table 2.2).

For the case of substitutional impurities in α -Fe, calculations of diffusivity have been performed for W, Mo, Cu, Ni, Cr, Al, etc. [11, 51, 53, 55, 56]. In addition, motivated by the question of whether any of the $5d$ solutes are slow diffusers in α -Fe, Asta *et al.* systematically investigated $5d$ transition metal elements, where experimental data was lacking [11, 43]. They found that Re had the lowest calculated impurity diffusion coefficient, approximately an order of magnitude lower than that for self-diffusion at temperatures near 1000 K. Recently, the effect of stress on self-diffusion in

bcc Fe was also investigated [60].

A summary of calculated diffusion parameters is given in Table 2.2. Good agreement is found for those cases where a comparison with experimental data is possible. These encouraging benchmark results provide an incentive to study solute diffusion in grain boundaries or interfaces, which is a much more complicated task than bulk diffusion.

2.3.3 Point Defects in Grain Boundaries

Recently, the structures of interstitials and vacancies in a variety of grain boundaries have been studied based on DFT and molecular statics calculations [41, 42, 61]. In these studies, the perfect grain boundary structure was first constructed based on the coincident site lattice theory, and then an atom was either added or removed at a selected boundary site to form an interstitial or a vacancy. The system was then relaxed to get the equilibrium structure. Note that there are only a few DFT calculations for such systems because the addition of point defects to a grain boundary requires much larger supercells and generally reduces the symmetry of the supercell. Both increase significantly the load on computing resources to the point that some calculations can not be conducted using modern software and hardware. Consequently, so far the results obtained by DFT are very limited. Therefore, the following section reviews mainly the results obtained by molecular statics and dynamics simulations.

It was found that formation energies of a point defect can be different at different boundary sites and depend on the grain boundary structure. Figure 2.9 shows an example of vacancy formation energies (E_v) in $\Sigma 5$ grain boundaries in fcc Cu obtained from molecular statics calculations [42]. It can be seen that at some sites the vacancy formation energy can be up to 10% lower as compared to the bulk, while at other sites, it may lie above the bulk value. Suzuki *et al.* pointed out that the observed spread of the point-defect energies could be attributed to the existence of alternating tension and compression regions in the grain boundary [41, 42]. Nevertheless, in general the vacancy formation energy in grain boundaries is on average lower as

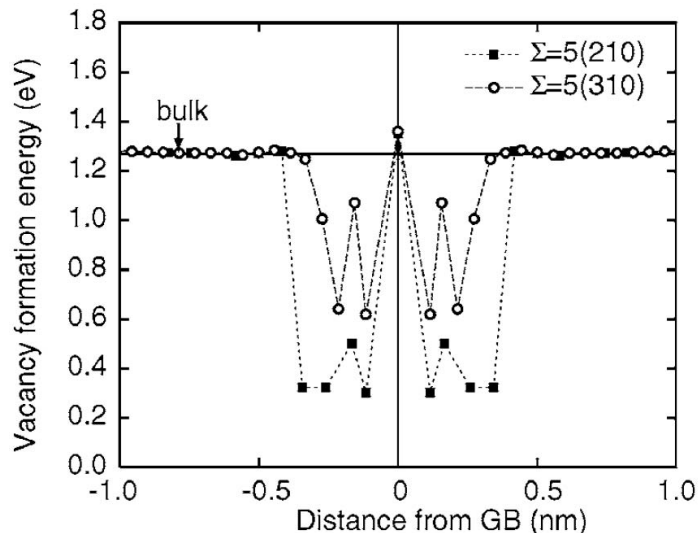


Figure 2.9: Molecular statics results for vacancy formation energy as a function of the distance from the grain boundary in Cu [42].

compared to that in the bulk [41, 42, 61, 62]. Similar to solute segregation at the grain boundary, the vacancy formation energy quickly approaches the bulk value as the distance from the boundary increases. Zhou *et al.* have studied local structural relaxations and formation energies of vacancies in various sites in the $\Sigma 5$ grain boundary in bcc Fe [62]. Using the DFT method, they found that the vacancy formation energy in the boundary region was 1.43~2.20 eV.

It should be emphasized that in the bulk, the relaxations around the vacancy are typically small, and the vacancy remains at the site where it is created. However, this may not be the case for grain boundaries. Brokman *et al.* and Kwok *et al.* reported that vacancies could produce considerably large relaxations of neighboring atoms. Moreover, some boundary sites were found to be unstable for vacancies [63, 64]. Similar findings were reported by Suzuki and Mishin [41, 42]. They systemically investigated a wide variety of configurations in Cu grain boundaries with one vacancy, and reported that the vacancy could delocalize in the grain boundary structure.

An example of this process is shown in Figure 2.10. In this case, a

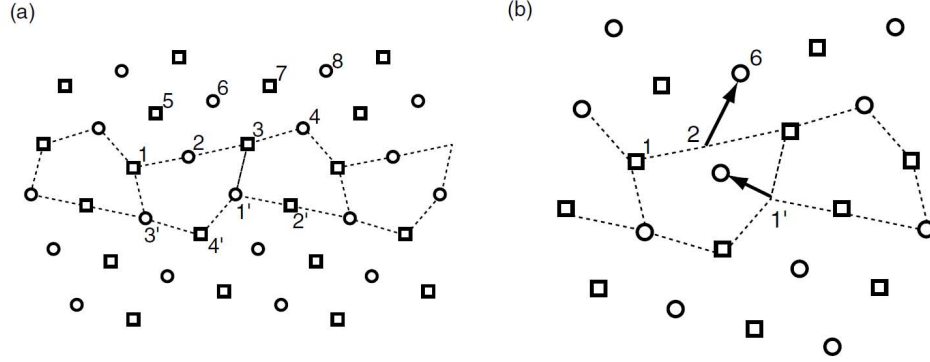


Figure 2.10: Examples of vacancy instability in Cu $\Sigma 9(1\bar{2}2)$ grain boundary. (a) Perfect grain boundary structure; (b) Unstable vacancy at boundary site 6 [42].

vacancy is created at site 6 in the $\Sigma 9(1\bar{2}2)$ grain boundary, however, this site is unstable for the vacancy and gets filled by atom 2. The vacancy at site 2 induces large relaxations, and as a result, the atom residing initially at site 1' moves to the midpoint between sites 1' and 2 after relaxation, which leads to a vacancy delocalization between these two positions. Note that if the vacancy is generated at site 1', one can get exactly the same configuration. Such vacancy delocalization phenomenon were also observed in $\Sigma 5$, $\Sigma 7$, $\Sigma 13$ grain boundaries in fcc Cu.

2.3.4 Diffusion Mechanisms in Grain Boundaries

Because of the complexity, the understanding of grain boundary diffusion is limited. Nevertheless, some progress has been achieved through DFT and molecular dynamics simulations, which reveal a number of generic properties of diffusion processes in grain boundaries [41, 42, 65, 66]. In these simulations, a single point defect (vacancy or interstitial) is created and its formation energy is evaluated at various positions in the grain boundary. The defect is then allowed to walk along the grain boundary, and the atomic trajectories are analyzed to determine the most typical diffusive events induced by the defect. The diffusion coefficient is then obtained for

various directions in the grain boundary.

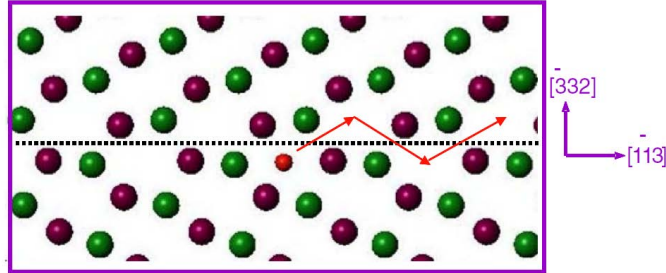


Figure 2.11: Possible migration path of He interstitial atom in the Fe $\Sigma 11$ grain boundary. Small sphere represents the He atom. Arrows indicate possible paths [65].

Figure 2.11 shows an example of a possible migration path of interstitial helium in the Fe $\Sigma 11$ grain boundary [65]. One can see that the interstitial helium migrates from the hexahedral position below the grain boundary plane (dotted line) to a similar position above the grain boundary plane, leading to helium diffusion along the $[1\bar{1}3]$ direction, as indicated by the arrows. Gao *et al.* reported strong binding between helium and the grain boundary with diffusion occurring within 3 atomic layers from the boundary plane. Liu *et al.* studied interstitial hydrogen diffusion in the $\Sigma 5$ grain boundary in Fe [67]. They found that in contrast to bulk diffusion, the diffusion coefficient perpendicular to the grain boundary plane is four orders of magnitude lower than that along the tilt axis. They also found a large binding energy of hydrogen to the grain boundary (see Table 2.1). The calculated diffusion coefficients of hydrogen atoms in the bulk, on the free surface and in a $\Sigma 5$ grain boundary are shown in Figure 2.12. The activation energies for hydrogen diffusion in bulk, surface, and grain boundary are 0.044 eV, 0.066 eV, and 0.31 eV, respectively. One can see that at low temperature, the diffusivity of interstitial hydrogen in the grain boundary is significantly lower than in the bulk.

In the case of vacancy migration, Ingle and Crocker studied self-diffusion in a $\Sigma 3$ (110) grain boundary in Fe [68]. It was shown that activation energies for a variety of vacancy jumps are substantially lower than in the bulk,

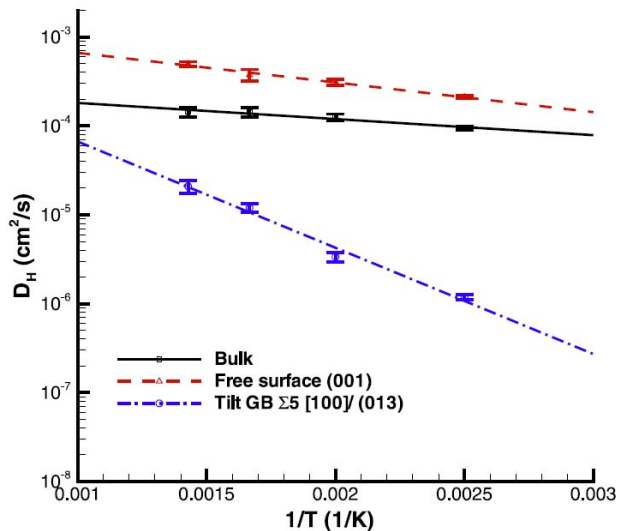


Figure 2.12: Diffusion coefficients of hydrogen atoms in bulk, on free surface and in a $\Sigma 5$ grain boundary. The activation energies for hydrogen diffusion in bulk, free surface, and grain boundary are 0.044 eV, 0.066 eV, and 0.31 eV, respectively [67].

suggesting faster boundary self-diffusion. Similar results were also reported by Kwok *et al.* [64]. They found that the vacancy propagation is almost entirely confined to the grain boundary region. Further, Lei *et al.* have calculated the activation energies for vacancy diffusion in $\Sigma 3$ (0001) grain boundaries of α -Al₂O₃ using DFT [66]. They found that the activation energies were up to 50% lower than in the bulk lattice, indicating faster diffusion in the boundary than in the bulk.

Generally, self-interstitials were found to be relatively immobile and not contributing to the fast grain boundary diffusion. Balluffi *et al.* reported that the activation energy for self-interstitials in Fe $\Sigma 5$ grain boundary was even larger than for self-diffusion in the bulk, suggesting that boundary self-diffusion was dominated by the vacancy exchange mechanism, and the interstitial mechanism could be ruled out [63]. Pontikis *et al.* investigated the self-diffusion mechanism in a $\Sigma 5$ grain boundary in fcc Cu [69]. Their results confirmed the immobility of the interstitial in the grain boundary,

which provided further support for the vacancy dominated mechanism of grain boundary diffusion.

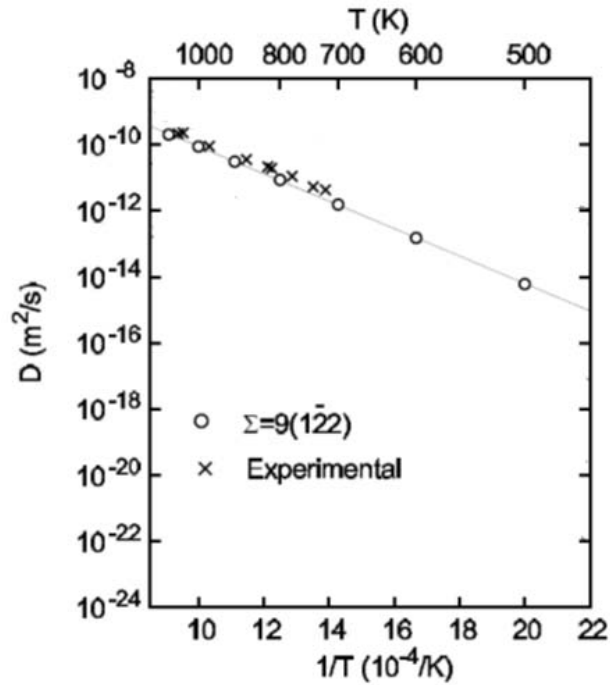


Figure 2.13: Calculated and measured self-diffusion coefficients in a $\Sigma 9$ Cu grain boundary [42].

In spite of the obvious complexity of diffusion processes in grain boundaries, both theoretical and experimental results show that grain boundary diffusion coefficients follow the Arrhenius law. Figure 2.13 shows the Arrhenius plot of calculated grain boundary self-diffusion coefficients in fcc Cu [42]. The experimental results are also shown for comparison. It can be seen that the calculations are in reasonable quantitative agreement with experimental measurements, which demonstrates that atomistic simulations are capable of predicting quantitative information on grain boundary diffusion.

2.4 Austenite (fcc) and Ferrite (bcc) Interface

2.4.1 Overview

To the best of our knowledge, no DFT simulations are available for the bcc-fcc interface in iron. The primary reason is the complexity of the magnetic state of fcc Fe since fcc Fe shows paramagnetic states, which creates a challenge for modeling bcc-fcc interface. In this section, we first review the magnetic properties of Fe within the framework of DFT. In the latter part of this section, DFT studies for heterophase interfaces are also discussed.

2.4.2 Approaches to Study Magnetism in γ -Fe

Magnetism plays an important role in understanding the physical properties of iron and iron alloys, including the relative stability of different phases [70]. There are many papers related to this research area. For example, in 1981 Kubler [71] investigated the total energies of nonmagnetic (NM), ferromagnetic (FM) and antiferromagnetic (AFM) states for bcc phases of iron by using the augmented-spherical-wave (ASW) method. He found that the ground state for the bcc structure is the ferromagnetic (FM) state. Such conclusion was confirmed by recent first-principle DFT calculations [9, 72, 73]. The magnetic moment per Fe atom in the bulk was predicted to be $2.20 \mu_B$ [9], which was in good agreement with the experimental value of $2.22 \mu_B$ [74].

The situation with γ -Fe (fcc) is much more uncertain. It is known that γ -Fe is stable in the temperature interval from $T=1173$ K and $T=1660$ K, and exists naturally in the paramagnetic (PM) state. Recent experiments also reported that thin films of γ -Fe could be anti-ferromagnetic or ferromagnetic [75, 76]. The complexity of the magnetic properties of γ -Fe presents significant challenge for DFT calculations. To identify the stable magnetic configuration for γ -Fe, an extensive search was performed based on first-principle DFT calculations [9, 72, 73].

The most straightforward approach to simulate the paramagnetic state within DFT is to use ordered magnetic arrangements, such as single-

layer antiferromagnetic (AFM) and double-layer antiferromagnetic (AFMD) states. The AFM and AFMD phases refer to the simple layered antiferromagnetic structure ($\uparrow\downarrow\uparrow\downarrow\dots$) and the bilayer AFM structure ($\uparrow\uparrow\downarrow\downarrow\dots$), respectively.

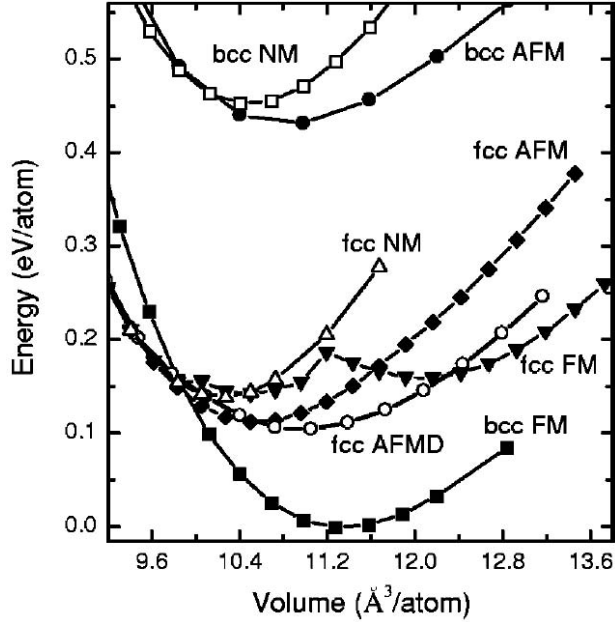


Figure 2.14: Phase diagram for bcc Fe and fcc Fe with different magnetic configurations [9].

In Figure 2.14, the calculated total energies of various magnetic configurations, i.e. non-magnetic (NM), ferromagnetic (FM), single-layer antiferromagnetic (AFM), and double-layer anti-ferromagnetic (AFMD), are shown as a function of lattice parameter. For fcc NM state, the minimum locates at 3.45 Å. Once the magnetism is included, the results change significantly. For the fcc FM phase, the curve displayed in Figure 2.14 presents two distinct and separate minima, a low-spin (LS) FM state with relatively small lattice constant and a high-spin (HS) FM phase with somewhat larger volume. In early work for carbon in γ -Fe, Jiang and Carter [9] took the HS FM state as a reference. A difficulty with this is that there is a discontinuous transition between the HS FM phase and the LS FM phase,

which could be triggered by defects. Here, the AFMD state has the lowest total energy for fcc Fe. Jiang *et al.* reported that the predicted lattice parameter for the AFMD state agrees well with those extrapolated from measured lattice parameters in γ -Fe alloys [9], which implied that AFMD is a good approximation for the fcc Fe. In addition, the calculated vacancy formation energy in the AFMD structure is 1.84 eV, which is relatively close to that concluded from experiment (1.71 eV) [77].

In recent years, based on the framework of DFT calculations, several new methodologies have been developed to treat disordered alloys. Several groups have applied these ideas in the studies of paramagnetic materials. The most widely used approaches can be summarized as follows:

Coherent Potential Approximation The coherent potential approximation (CPA) treats random $A_{1-x}B_x$ alloys by considering the average occupations of lattice sites by A and B atoms [78]. Since it is a mean field approach, local relaxations are not considered explicitly and the effects of alloying elements on the distribution of local environments cannot be taken into account, which is a major drawback to the application of this approach.

Cluster Expansions Approach In the case of Cluster Expansions (CE) Approach [79], the Ising model is used and the occupations of atoms A and B in the parent lattice are labelled as $+1$, and -1 . The configurational energetics of the system is characterized by using the effective cluster interactions (ECIs). In order to estimate the ECIs, the energies of multiple pre-selected ordered configurations have to be obtained in their fully relaxed geometries based on the DFT calculations, which is rather laborious work.

Special Quasi-random Structures The concept of Special Quasirandom Structure (SQS) was proposed first by Zunger *et al.* [80]. The basic idea of SQS is to mimic random solutions by using a small unit cell with only a few (4~32) atoms, which best satisfies near-neighbor pair and multisite correlation functions of random substitutional alloys. Compared with the

Coherent Potential Approximation and Cluster Expansions approaches, which treat the random alloys by considering average occupations and requires dozens of calculations, a single calculation is sufficient for the SQS approach to obtain the required properties of a random alloy.

In recent years, the SQS technique has been successfully applied to study the paramagnetic state of metals. For example, Shim *et al.* studied the magnetic transition for Fe_2O_3 using a 40-atom SQS supercell, and predicted that in the paramagnetic state, Fe_2O_3 is metallic, which is consistent with the experimental observation [81].

Recent DFT calculations also showed that the ground state of fcc Fe can be a spin-spiral state [82, 83]. However, the results indicate that the energy difference to the AFMD order is only a few meV/atom, and the lattice constant between these two structures differs by only 0.01 Å. Moreover, Ackland *et al.* found that most of the non-collinear calculations for γ -Fe with defects converged to collinear magnetic states [84]. Only few configurations retained non-collinear structures. However, the energy of the non-collinear configuration was only marginally lower than the collinear results. On the other hand, the non-collinear calculations are extremely time-consuming, such that only small periodic supercells (typically consisting of 4~32 atoms) can be considered.

2.4.3 Effects of Solutes on Magnetism of γ -Fe

The impurity effects on the magnetic properties of fcc Fe were also investigated by means of DFT. For substitutional elements, Kong and Liu reported that the ferromagnetic state of fcc Fe phase could be stabilized by Cu atoms, which was attributed to chemical pressure effects due to the larger atomic volume of Cu [85]. The magnetic moment per Fe atom of the fcc structured Fe-Cu alloys is shown as a function of Cu concentration in Figure 2.15. In agreement with experimental observations, the authors find that the magnetic moment of Fe increases with Cu concentration. Recently, Medvedeva *et al.* performed DFT calculations to study the effect of Mn

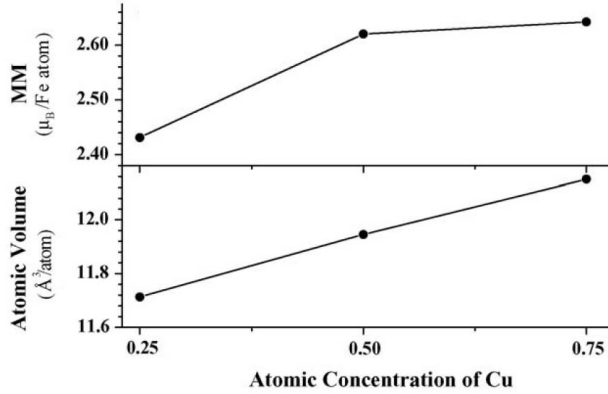


Figure 2.15: Variation of average atomic volume and magnetic moment (MM) per Fe atom of the fcc structured Fe-Cu alloys against the Cu concentration [85].

substitution on the structural and magnetic properties of fcc Fe [86]. Their results suggested that Mn favored the ferromagnetic coupling which, in principle, could lead to long range ferromagnetism.

In the case of interstitials, Boukhvalov *et al.* investigated the local perturbations of the crystal and magnetic structure of fcc Fe near a carbon interstitial impurity [73]. The fragment of crystal and magnetic structure of γ -Fe for the AFMD ordering is shown in Figure 2.16. By comparing the total energy and magnetic moments for FM, AFM, and AFMD structures, they found that the ferromagnetic state could be stabilized locally by the carbon interstitial. However, the global magnetic structure is still the AFMD state.

Hydrogen is especially important for steels since it can lead to hydrogen embrittlement. Nazarov and co-workers investigated the thermodynamics of hydrogen-vacancy interaction in fcc Fe. They studied several ordered collinear magnetic configurations. The results demonstrated that the ground state is a locally modified AFMD configuration [87]. It was found that hydrogen in interstitial positions significantly changed the local magnetization and increases the total magnetic moment of the system by $0.52 \mu_B$.

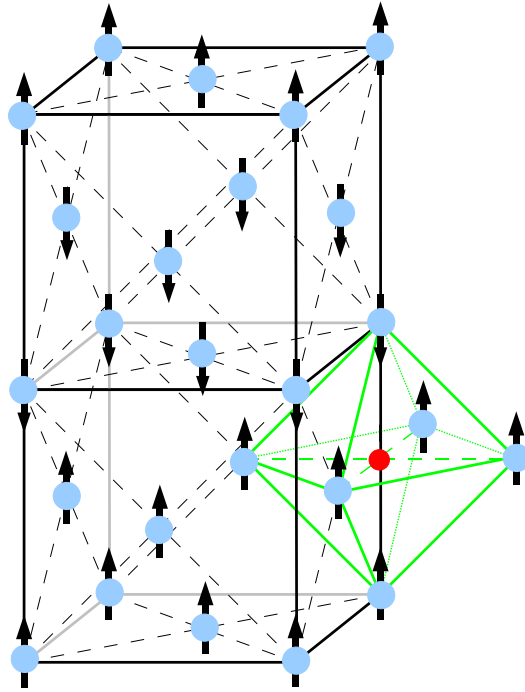


Figure 2.16: Fragment of crystal and magnetic structure of γ -Fe for the AFMD magnetic ordering [73]. Carbon interstitial impurity in octahedral position is shown by dark (red) circle.

2.4.4 DFT Studies for Heterophase Interfaces

Recently, DFT has been used to study solid-solid heterophase interfaces. Figure 2.17 shows the supercell used in a DFT study of an interface between bcc-Fe and fcc-Ag [88]. The interfaces were constructed according to the Nishiyama and Wassermann (N-W) orientation relationship. An important output of such calculations is the interfacial energy, which is a key parameter determining the nucleation barrier and also the shapes of precipitates. In addition, the interfacial energy obtained by DFT calculations can be used as the input parameter for mesoscopic simulations, such as phase-field models. Vaithyanathan *et al.* demonstrated how DFT and phase-field models can be

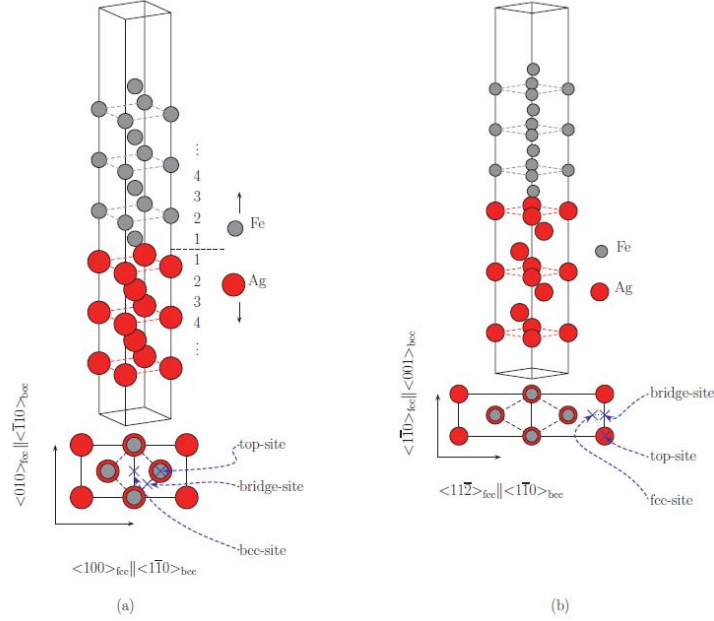


Figure 2.17: Schematic of the (a) Fe(001)-Ag(001) interface and the (b) Fe(110)-Ag(111) interface [88]. The cross symbols mark the high-symmetry sites with respect to the Ag plane for the successive Fe atom at interface. The layers around the interface are indexed by numbers.

combined to build a bridge between micro- and macro-scales [89, 90]. They constructed coherent (100) and semi-coherent (001) interfaces of θ' -Al₂Cu in fcc Al solid solution and then calculated interfacial energies using DFT. Using these energies in the phase field model, the authors demonstrated that the theoretical precipitate microstructure evolution is in good agreement with the experimental data.

Magnetic properties of the interfaces is another subject of recent DFT studies. Benoit *et al.* reported that the magnetic moments of the Fe atoms in the Au(001)/Fe(001) interface are enhanced by about 26% [91]. The layer projected magnetic moments are summarized in Figure 2.18, where the interface position corresponds to the index -1. It is observed that magnetic properties of the interfaces between magnetic and non magnetic materials

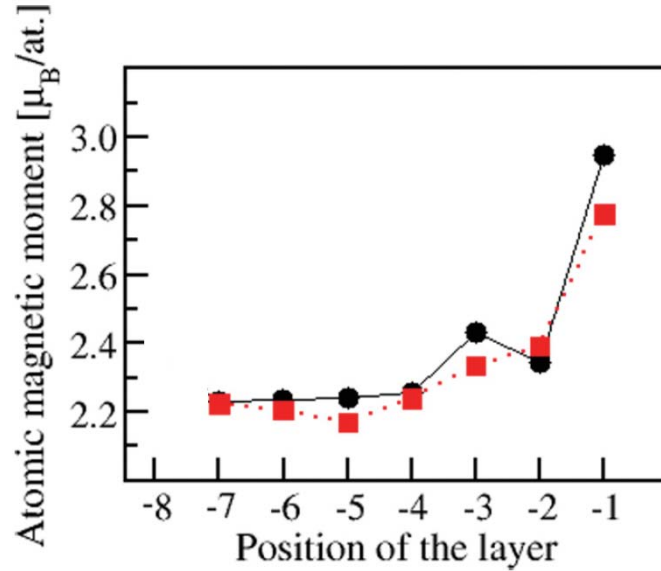


Figure 2.18: Evolution of the atomic magnetic moment of the Fe atoms as a function of the position of the layer in the Fe(001) slab (black circles) and in the Au(001)-Fe(001) interface (red squares) [91].

resemble very closely that of the surface of the magnetic material.

The electronic properties of the Au(001)/Fe(001) interface system were also investigated [91]. Figure 2.19 shows the projected densities of the d states (PDOS) of individual Fe atoms at the surface, in the center, and in the Au(001)/Fe(001) interface. Comparing the PDOS of Fe atoms at the surface or at the interface with the one in the center, one observes that the presence of the surface or interface shifts the spin-down states by around +2 eV down to 0-0.5 eV. In addition, due to the presence of the surface or interface, the spin-up states below the Fermi level shift down to lower energies.

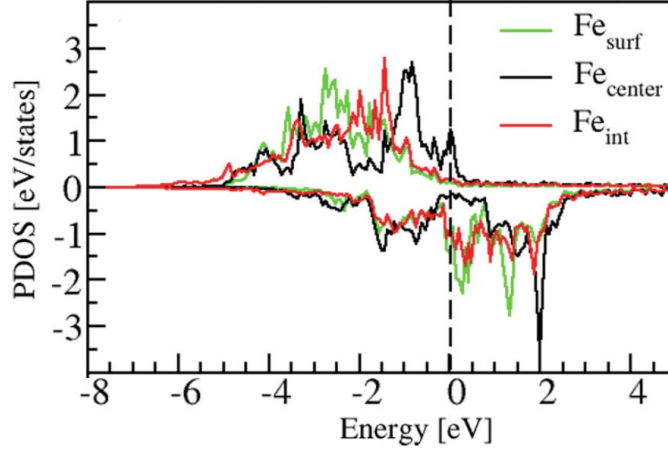


Figure 2.19: Projected densities of the d states of individual Fe atoms in the Au(001)/Fe(001) interface. Fe_{surf} , Fe_{center} , and Fe_{int} denote the Fe atoms at the surface, in the center, and at the interface, respectively [91].

2.5 Conclusions

Based on the first-principle studies, the segregation behavior of non-metallic elements, e.g. hydrogen, boron, carbon, phosphorous, etc., and their effects on special low Σ grain boundaries have been extensively studied. In addition, some general, e.g. high Σ and low angle, grain boundaries were also investigated through molecular dynamics simulations. However, the role of transition metals (TMs) such as V, Mn, Ti, Nb, etc. has received somewhat less attention. Experimentally, it is known that these TMs actually play rather important roles in microstructure evolution and mechanical properties of materials through the solute-drag effect. So far, the quantitative knowledge of the effect of these TMs on the Fe grain boundaries is still limited. Hence, it is necessary to advance our knowledge on the interactions between TMs and grain boundaries and interfaces using first-principle DFT simulations.

Previous studies indicated that fast grain boundary diffusion is governed by a vacancy mechanism in the vast majority of boundaries. The activation energy of a vacancy jump is found to be substantially lower than in the bulk.

Despite these encouraging results, the understanding of grain boundary diffusion is still limited. To the best of our knowledge, no work has been done for substitutional solute atom diffusion in grain boundaries due to the expensive computational costs for first-principle calculations and the lack of suitable interatomic potentials for molecular dynamics simulations. Nevertheless, previous theoretical simulations have already demonstrated that atomistic simulations are capable of predicting quantitative information about diffusion in metals. So there is a strong motivation to understand more about the diffusion mechanisms in grain boundaries in Fe based on cutting edge modeling tools.

So far, the AFMD configuration is considered as a good approximation for the magnetic ground state of γ -Fe. Previous studies have also shown that the substitutional and interstitial elements could influence the local magnetic state, however, the global magnetic structure is still AFMD state. In addition, the new developed special quasi-random magnetic structures provide an opportunity to deal with the paramagnetic state of γ -Fe in a more realistic manner. In the current state, AFMD and quasi-random structures are promising approximations to simulate the magnetic states of γ -Fe.

Chapter 3

Scope and Objectives

The aim of this work is to quantify how solute atoms interact with interfaces in Fe. For this purpose, we use first-principle DFT combined with kinetic Monte Carlo simulations. The critical solute drag parameters such as binding and activation energies will be determined and the coefficient for interface diffusion will be calculated. Special grain boundaries, e.g. $\Sigma 5$ (013) symmetrical tilt grain boundaries in bcc Fe, will be investigated in detail. This kind of special boundary has a small periodic unit cell, which makes our proposed DFT calculations feasible. The studies will then be extended to more complex interfaces, i.e. selected bcc-fcc Fe interfaces to study the solute-interface interaction and the diffusion mechanisms. More specifically, the objectives of this work can be divided into five main goals:

1. Investigate special grain boundaries, e.g. the $\Sigma 5$ (013) symmetrical tilt grain boundary, containing commonly used alloying elements, e.g. Mn, Mo, Nb and V, etc. to determine the binding energies of these solutes to the grain boundary and their activation energies for diffusion along the boundary.
2. Select the proper magnetic configurations for fcc Fe and determine the basic properties of a selected bcc/fcc interface, including the geometric, electronic and magnetic structures.
3. Investigate the interactions between alloying elements and the fcc grain boundaries and determine the binding energies of these solutes.

4. Quantify the interactions of solutes with a selected bcc-fcc interface and determine the binding energies of these solutes.
5. Develop a KMC model to determine the diffusion coefficients in grain boundaries and bcc-fcc interfaces.

Chapter 4

Methodology

4.1 Density Functional Theory

4.1.1 Fundamentals

Theoretically, an exact treatment of solids can be obtained by solving the many-body Schrödinger equation involving both the nuclei and the electrons:

$$\hat{H}\Psi(\vec{R}_1\vec{R}_2\dots\vec{R}_N, \vec{r}_1\vec{r}_2\dots\vec{r}_n) = E\Psi(\vec{R}_1\vec{R}_2\dots\vec{R}_N, \vec{r}_1\vec{r}_2\dots\vec{r}_n) \quad (4.1)$$

where \vec{R}_i are the nuclei coordinates, \vec{r}_i are the electron coordinates, \hat{H} is the Hamiltonian operator, Ψ is the wave function, E is the total energy of the system, N is the total number of nuclei, and n is the total number of electrons in the system. The Hamiltonian operator \hat{H} is the sum of the kinetic energy operator \hat{T} and the potential energy operator \hat{V} . The wave function Ψ is a measure for the probability of finding the particle at a certain position. The probability density of a particle is the square of the amplitude of the wave function, $|\Psi|^2$. However, it is extremely difficult to solve the many-body Schrödinger equation. In fact, the only system that can be solved analytically is the single-electron hydrogen atom. In general, the Schrödinger equation has to be solved numerically.

Hohenberg and Kohn have shown that the total energy of a system can

be uniquely defined by the electron charge density and has a minimum corresponding to the ground state density [92], i.e.

$$E_0 = \min(E[\rho(\vec{r})]) \quad (4.2)$$

Within the framework of Kohn and Sham, the many-body problem of interacting electrons in a static external potential is reduced to a problem of non-interacting electrons moving in an effective potential, and the original many-electron Schrödinger equation is then converted into a set of Kohn-Sham equations [93]:

$$\left(\hat{T}[\rho(\vec{r})] + \hat{H}_H[\rho(\vec{r})] + \hat{U}_{ext}[\rho(\vec{r})] + \hat{V}_{xc}[\rho(\vec{r})] \right) \Phi_i(\vec{r}) = \xi_i \Phi_i(\vec{r}) \quad (4.3)$$

where $\hat{T}[\rho(\vec{r})]$ is the non-interacting kinetic energy, $\hat{H}_H[\rho(\vec{r})]$ is the electrostatic interactions between electrons, $\hat{U}_{ext}[\rho(\vec{r})]$ is the potential energy from the external field due to positively charged nuclei, and $\hat{V}_{xc}[\rho(\vec{r})]$ is the so-called exchange-correlation energy. So far, the exact form of exchange-correlation energy is still unknown. For this reason, suitable approximations have been introduced.

4.1.2 Exchange-correlation Energy

The most widely used approximation is the so-called Local Density Approximation (LDA), which assumes that the exchange correlation energy is a function of the local charge density [94]. LDA has been demonstrated successful when employed to solids. However, one significant limitation of LDA is its overbinding of solids: lattice parameters are usually underpredicted while cohesive energies are usually overpredicted. In addition, LDA calculations predicted the hexagonal para-magnetic structure are the most stable state in Fe, whereas it is well known that the ground state of Fe should be the bcc ferromagnetic state.

In an effort to rectify the inaccuracies of LDA, the Generalized Gradient Approximation (GGA) was introduced [95]. GGA is a natural improvement on LDA by considering not only the local charge density, but also its

gradient. The results calculated by GGA generally agree noticeably better with experiments than LDA. It also gives a better description of $3d$ transition metals [96]. For example, the ground state of Fe is correctly predicted within the GGA calculations. For these reason, in this project, the GGA proposed by Perdew, Burke, and Enzerhof (PBE) will be adopted rather than LDA for the exchange-correlation energies.

4.1.3 Structure Optimization

The crucial point when performing DFT calculations is to find the electronic ground state of the system, which is usually referred as structure optimization (or “relaxation”). In principle, when searching for the optimal geometry, the DFT code performs several ionic relaxation steps. It moves all nuclei in appropriate directions (according to energy gradients), in which each nucleus should have lower potential energy. After each ionic step, the ground state energy of this particular atomic arrangement has to be evaluated by a self-consistent cycle of electronic relaxation steps. Once the difference of any 2 consecutive energy values is lower than a given threshold value, the self-consistent cycle is finished. Then the energy gradients (or forces on atoms) are evaluated. If they are lower than pre-defined threshold values, the optimized structure is achieved. Otherwise, new positions of atoms are proposed and repeat from the start. For finding the ground state according to the energy and its gradients, the following numerical algorithms are widely used in DFT codes:

- (1) Steepest descent method
- (2) Conjugate-gradient (CG) method

The scheme of search paths for locating the minimum of the energy by an iterative process using the steepest descent and conjugate gradient methods is shown in Figure 4.1. In the steepest descent procedure, the minimization procedure starts at an arbitrary point (e.g. point 1 in Figure 4.1) and evaluates the gradient of the energy [97]. The negative of the gradient vector gives the direction of the steepest descent which is followed until a minimum is reached along this line. At that point, the procedure is repeated until the

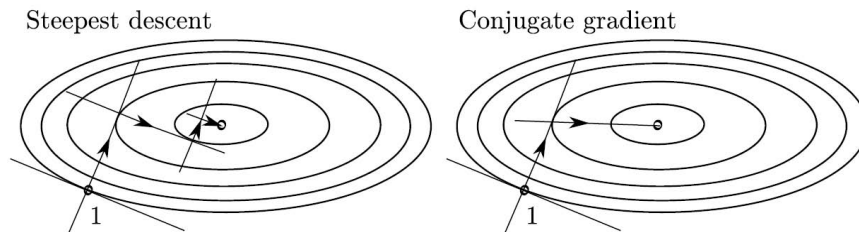


Figure 4.1: Sketch of the search paths for the minimum of a function (i.e. energy) using the steepest descent (left) and conjugate-gradient approach (right). In both cases, the search begins at point 1. The conjugate-gradient method converges faster [97].

value can no longer be lowered within a given convergence threshold. It is evident that this procedure is reasonable, but not efficient.

A more efficient approach is the conjugate gradient method, which first also starts a steepest descent step with line minimization. However, in the following step, the search direction contains information not only from the gradient at the current point, but also “conjugated” to the previous search directions. Sheppard *et al.* reported that the convergence based on the conjugate-gradient algorithm is four times faster than that of steepest descent method [98]. Therefore, in this project, we will use conjugate-gradient algorithm to find the optimized structure.

4.1.4 Simulation Software Package

There are many DFT codes currently available, among which the widely used software packages are Wien2k, Siesta, FIREBALL, VASP, CASTEP, PWSCF, and ABINIT. Wien2k employs the so-called all-electron DFT method, which means all electrons are treated in the same framework. This treatment can provide highly accurate band structure, total energy, etc. However, it is also computationally demanding. In contrast, Siesta and FIREBALL use atomic orbitals as basis set, which are much more efficient. The main disadvantage is incompleteness of the smallest basis set which means the calculated properties often show extreme sensitivity to small changes in the basis set. To balance the computational load and accuracy,

VASP, CASTEP, PWSCF, and ABINIT codes were developed based on the plane wave basis set and pseudopotential approximations.

In these DFT codes, the wave functions are expanded in terms of plane wave basis set, i.e.:

$$\Phi_i(\vec{r}) = \frac{1}{\sqrt{\Omega_0}} \sum_{\vec{G}} c_i(\vec{G}) e^{i(\vec{k}+\vec{G})\cdot\vec{r}} \quad (4.4)$$

where \vec{G} is the vector of the reciprocal lattice, \vec{k} denotes the momentum, and Ω_0 represents the primitive cell volume. In practice, only a finite set of plane waves is used for a given system. The completeness of the basis set is controlled by the cut-off energy (E_{cut}), i.e.

$$\frac{(k+G)^2}{2} < E_{\text{cut}} \quad (4.5)$$

where $\frac{(k+G)^2}{2}$ denotes the kinetic energy of a plane wave. Only those plane-waves with a kinetic energy smaller than E_{cut} are included in the basis set. The main disadvantage of a plane wave basis set is that a large number of basis functions is required to describe atomic wave functions near the nucleus. To overcome this problem, the pseudopotential approximation is employed. This approximation is based on the assumption that only the valence electrons have significant effect on the physical and chemical properties of the system. Therefore, the core electrons do not need to be treated explicitly any more. This approximation provides usually a sufficiently good result, while it is much more efficient when compared with the all-electron DFT calculations.

It is noticeable that the pseudopotentials for PWSCF and ABINIT codes are still not available for some elements, which limit the application of these two codes. Fortunately, the pseudopotentials for VASP and CASTEP codes are complete and reliable. However, the CASTEP code does not support searching transition states, and therefore is not suitable for diffusion studies. Consequently, VASP is used as the DFT algorithm in this work.

VASP, i.e. Vienna Ab initio Simulation Package, is a computer program

for atomic scale materials modelling, e.g. electronic structure calculations from first principles. It computes an approximate solution to the many-body Schrödinger equation within density functional theory, solving the Kohn-Sham equation. The optimized structures, ground state energy, transition states, etc. can be obtained based on the VASP calculations. In previous studies, VASP has been successfully applied to investigate grain boundary segregation and diffusion of solutes [11, 25–27]. Note that the computational load of DFT calculations is expensive. A simple structure relaxation calculation for $\Sigma 5$ Fe grain boundary containing 120 atoms takes 3 days using 32 CPU cores. As a result, the calculation domain is usually small for VASP simulations, which is limited to about 100~200 atoms. In the present work, the calculations are performed using Westgrid supercomputing resources.

4.1.5 Domain Size

The Influence of the Energy Cut-Off

As has been discussed in subsection 4.1.4, the cut-off energy is an important and sensitive variable, which determines the plane wave basis set. The influence of the cut-off energy on the convergence of the total energy of the conventional bcc Fe unit cell has been evaluated with a fixed k -point mesh of $20 \times 20 \times 20$. The testing results are shown in Figure 4.2. It is evident that the total energy is well converged with kinetic energy cut-offs over 350 eV. Therefore, in this work, the cut-off energy is set to be 350 eV.

The Influence of the k -Point Sampling

For a periodic system, integrals in real space over the infinite system are replaced by summing the values at a finite number of points in the Brillouin zone, i.e. the k -point mesh. Choosing a sufficiently dense mesh of k points is crucial for the convergence of the results. Based on the scheme proposed by Monkhorst and Pack, k -points are distributed homogeneously in the Brillouin zone [99]. The distance between two k points in reciprocal space

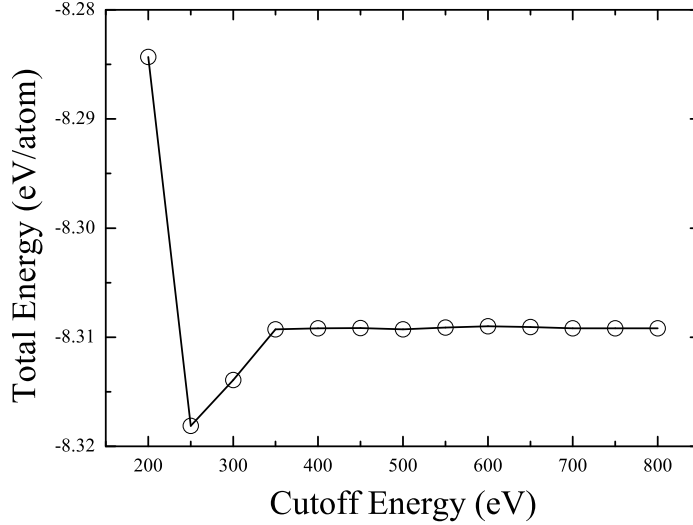


Figure 4.2: Convergence test of the total energy with respect to energy cutoff.

is given as:

$$d_{k\text{-points}} = 1/k_i l_i \quad (4.6)$$

where l_i is the supercell dimension in i direction. k_i determines number of k -points in i direction. For example, $k_1=k_2=k_3=3$ indicates a $3\times 3\times 3$ k -point mesh. In order to check the influence of the k -point mesh in reciprocal space on the convergence of energy values, grids of $1\times 1\times 1$ up to $20\times 20\times 20$ k -point mesh are evaluated. This gives the k -points spacing from 0.352 \AA^{-1} to 0.018 \AA^{-1} for the conventional bcc Fe unit cell with the lattice constants of 2.84 \AA . In Figure 4.3, the total energy of the conventional bcc Fe unit cell is well converged to 0.1% with a $8\times 8\times 8$ k -point mesh (i.e. the separation is 0.05 \AA^{-1}). In the following calculations, the k -points spacing is set to be equal or smaller than 0.05 \AA^{-1} within the first Brillouin zone.

Size of the Supercell

In this work, the convergence with respect to number of atoms is also evaluated. We have adopted four sizes of Fe bcc supercell from 16 atoms $2\times 2\times 2$ supercell, 54 atoms $3\times 3\times 3$ supercell, 128 atoms $4\times 4\times 4$ supercell,

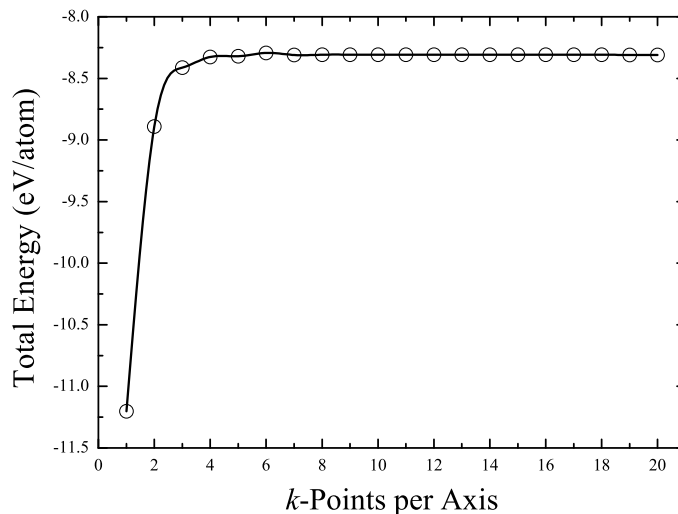


Figure 4.3: Convergence test of the total energy with respect to k -point mesh for the conventional bcc Fe unit cell.

and 250 atoms $5 \times 5 \times 5$ supercell. The cohesive energy for Nb, which is the largest and least elastically favorable solute studied in this work, is shown in Figure 4.4. The Nb cohesive energies are converged for system sizes of 54 atoms and larger to within 0.01 eV. Therefore, in the following calculations, a $3 \times 3 \times 3$ or an equivalent supercell is adopted.

Special Quasirandom Structure Calculations

As discussed in the previous sections, the special quasirandom structure (SQS) is proposed to determine properties of random solid solutions through a periodic structure, which is employed here to simulate the paramagnetic state of γ -phase Fe. In order to characterize the statistics of a given atomic arrangement, the correlation functions are introduced.

Using the language of Ising models, each site i of the configuration is assigned a spin variable \hat{S}_i , which takes the value -1 if it is occupied by $\text{Fe}\uparrow$ (i.e. Fe atom with spin-up state), or +1 if occupied by $\text{Fe}\downarrow$ (i.e. Fe atom with spin-down state). Furthermore, all the sites can be grouped in figures $f(l, m)$ of l vertices, where $l = 1, 2, 3, \dots$ corresponds to a shape: point,

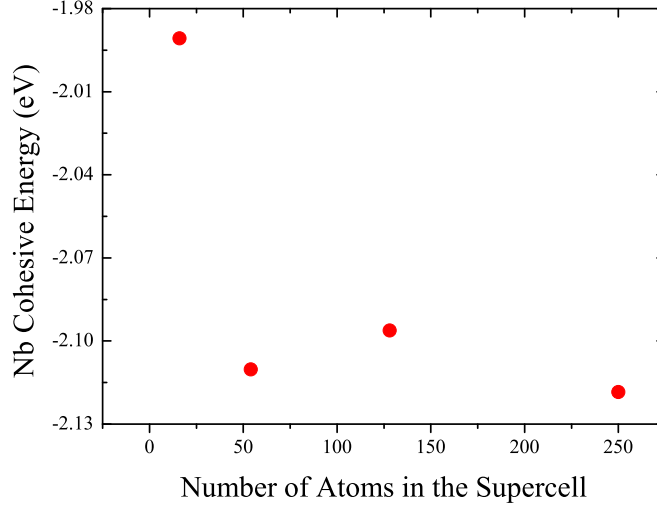


Figure 4.4: Convergence test of Nb cohesive energy with respect to supercell size.

pair, and triplet... respectively, spanning a maximum distance of m , where $m = 1, 2, 3, \dots$ is the first, second, and third-nearest neighbors, and so forth. For example, pairs of atoms (a figure with $l=2$ vertices separated by an m^{th} neighbor distance), triangles ($l=3$ vertices), etc. The correlation functions, $\overline{\prod}_{l,m}$, are the averages of the products of site occupations of figure k at a distance m . The optimum SQS for a given composition is the one that best satisfies the condition:

$$(\overline{\prod}_{l,m})_{SQS} \cong \langle \overline{\prod}_{l,m} \rangle_R \quad (4.7)$$

where $\langle \overline{\prod}_{l,m} \rangle_R$ is the correlation function of a real paramagnetic γ -phase Fe. Since there is no correlation for the real paramagnetic γ -phase Fe, the correlation function is simply zero.

In the present work, the Alloy Theoretic Automation Toolkit (ATAT) [100] has been used to generate SQS for the fcc structure. In general, the smaller the unit cell, the worse the correlation functions that match those of the real γ -phase Fe with paramagnetic state. Note that the algorithm used in this work is to enumerate every possible supercell and every possible

atomic configuration, which becomes prohibitively expensive as the size of the SQS increases. Hence, we use a SQS supercell consisting of 32 atoms to simulate the paramagnetic state of γ -phase Fe.

Grain Boundary Energy

In order to obtain reliable results, it is necessary to consider a supercell with reasonable size. In particular, the distance between two adjacent grain boundaries should be sufficiently large to decouple them from each other. For this purpose, the supercell size for grain boundary is determined from calculation of the grain boundary energy as a function of inter-boundary distance. In this work, the grain boundary energy (σ_{gb}) is calculated as the difference between the total energy of the supercell with (E_{gb}) and without (E_{bulk}) grain boundaries, which can be expressed as:

$$\sigma_{gb} = \frac{1}{2A_S}(E_{gb} - E_{bulk}) \quad (4.8)$$

where A_S is the area of the boundary, which is chosen to be comparable with a $3 \times 3 \times 3$ bulk supercell, i.e. $8.52 \times 8.52 \text{ \AA}^2$. Note that there are two grain boundaries in the supercell that is imposed by the periodic boundary conditions. Therefore, the grain boundary energy is corrected by the factor of 2.

α - γ Interface Energy

In a similar manner, the α - γ interface energy is calculated as follows:

$$\sigma_{\alpha-\gamma} = \frac{1}{2A_S}(E_{\alpha-\gamma} - E_{\alpha} - E_{\gamma}) \quad (4.9)$$

where E_{α} and E_{γ} are the total energies of the supercell for bcc and fcc grains, respectively. $E_{\alpha-\gamma}$ is the total energy of the supercell consisting of bcc grain, fcc grain, and the α - γ interfaces.

4.1.6 Parameter Setup and Formulas for DFT Calculations

As has been discussed above, all of the DFT calculations are carried out using VASP [101, 102], with the projector augmented wave (PAW) method [103], and the Perdew-Burke-Ernzerhof (PBE) generalized gradient approximation (GGA) to the exchange correlation functional [104]. Since Fe is a magnetic element, its spin-up density (ρ_{\uparrow}) and spin-down density (ρ_{\downarrow}) are not the same. Therefore, the spin-polarized DFT calculations were performed. Note that compared with the non-spin polarized calculations, the accuracy is the same on both levels. Which solution is more reasonable only depends on whether the system is magnetic or not. If it is (either FM or AFM), the calculation has to be done spin-polarized, and the total energy of the cell will be more negative than for the non-polarized calculation. If it is not, the results should be the same for both calculations.

In this work, a cutoff energy of 350 eV is used to truncate the plane-wave expansion of the wave functions. Full relaxation of the atomic positions is allowed to an energy convergence of 10^{-4} eV and force convergence of 10^{-2} eV/Å in each case, using a conjugate gradients routine to find the local minimum.

4.1.7 Simulation Procedure for Solute Segregation

To study the solute-interface interactions, the binding energy (also referred as segregation energy) of the solutes with the grain boundaries is calculated. A straightforward way to calculate segregation energies would be to compare the energies of a system with a grain boundary and a solute atom where in one case the solute is located at the boundary and in another case in the bulk sufficiently far away from the boundary to avoid any elastic coupling with the boundary. The required large supercell would lead to prohibitive computational cost such that an alternative approach is employed by executing separate grain boundary and bulk simulations using smaller supercells. Hence, the binding energy is expressed as:

$$E_{seg}^i = (E_{X+gb}^i + E_{ref}) - (E_{gb} + E_X) \quad (4.10)$$

where E_{gb} and E_{ref} are the total energies of the pure Fe system calculated with and without grain boundaries, whereas E_{X+gb}^i and E_X are the total energies of the supercell with and without grain boundaries and one solute atom. The superscript i denotes the substitutional sites in the grain boundary. A negative value for E_{seg}^i indicates an attractive segregation energy of the solute atom to the considered grain boundary site.

The segregation energy for the second solute is calculated as:

$$E_{seg}^{i,j} = (E_{X+Y+gb}^{i,j} + E_{ref}) - (E_{Y+gb}^j + E_X) \quad (4.11)$$

where $E_{X+Y+gb}^{i,j}$ is the total energy of the supercell containing solutes X and Y occupying boundary sites i and j , respectively. E_{Y+gb}^j is the total energy of the supercell with solute Y placed at boundary site j .

To analyze the solute-solute interaction, the effective interaction (E_{eff}) is calculated, which is defined as:

$$E_{eff} = (E_{X+Y} + E_{ref}) - (E_X + E_Y) \quad (4.12)$$

where E_X (E_Y) is the total energy of a configuration containing one single solute atom and E_{X+Y} is the total energy of a supercell with two solute atoms. E_{ref} is the total energy of the solute free supercell. A positive value of E_{eff} corresponds to repulsive interaction.

4.1.8 Simulation Procedure for Diffusion

The simulation procedure for diffusion employed in this work is outlined as follows: first, a single point defect is introduced at various positions in the system and its formation free energy is calculated using DFT. The vacancy formation energy can be calculated as:

$$E_v = E_{\square} - E_{ref} + E_{ref}/N \quad (4.13)$$

where E_{\square} and E_{ref} are the total energies of the pure system calculated with and without a vacancy, respectively.

In case of solute substitution, one should also calculate the binding

energy for the vacancy-solute pair which can be expressed as:

$$E_b = (E_{\square+X} + E_{ref}) - (E_{\square} + E_X) \quad (4.14)$$

where $E_{\square+X}$ (E_X) is the total energy of the supercell with (without) vacancy and one solute. We define E_b such that favorable binding is negative.

At the next step, migration energies (E_m) of the atomic jumps, which are the energy difference between the saddle-point barrier and the equilibrium position, are computed using nudged elastic band (NEB) method with the climbing image algorithm [105, 106]. In implementing this method, $N + 2$ configurations are considered, where N configurations are from intermediate states along the transition path and the other two are the initial and final states of migration, both of which are local minima on the potential energy surface. It is started by minimizing a transition path as a chain of images that connect the initial and a final state. A minimization algorithm is applied, and the energy is minimized in all directions except for the direction of the reaction path. The images are moved in the direction to minimize the forces, which gives the minimum energy path, with the highest point on the path being a best guess of the saddle-point (SP). The atom migration energy (E_m) is then determined based on the NEB calculations.

The activation energy at 0K (Q_0) is then given as the sum of the vacancy formation, migration and solute-vacancy binding energies in the fully ordered ferromagnetic state:

$$Q_0 = E_v + E_b + E_m \quad (4.15)$$

In order to model rate phenomena, harmonic transition-state theory (TST) is used in this work. Harmonic TST offers a straightforward approximation to a rate constant, at which atoms move from one site to a neighboring one. In Harmonic TST, the jump frequencies are given by [107]:

$$\Gamma = \nu_0 \exp\left(-\frac{E_m}{k_B T}\right) \quad (4.16)$$

where ν_0 denotes the ‘‘attempt frequency’’ telling how often an attempt

is made to exceed the barrier. Typically it is of the order of the Debye frequency, i.e. $10^{12} \sim 10^{13} s^{-1}$. The attempt frequency (ν_0) is calculated as:

$$\nu_0 = \prod_{i=1}^{3N-3} \nu_i^{eq} / \prod_{i=1}^{3N-4} \nu_i^{sp} \quad (4.17)$$

where ν_i^{eq} and ν_i^{sp} are the frequencies of the equilibrium and saddle-point configurations. In this work, the vibrational frequencies were computed from the Hessian matrix (see next section for details). In previous studies, Asta *et al.* explicitly calculated vibrational spectrums for Mo, W, and Fe-self diffusion, and found that the attempt frequencies were very similar [11], which can be ascribed to the same diffusion mechanism (vacancy mediated) and the same host. And consequently, in their later studies, they assumed the attempt frequencies (ν_0) were constant for all of the jump rates (Γ) [43]. Since $\Sigma 5$ grain boundary is a simple and ordered structure, we assume the values of attempt frequencies in $\Sigma 5$ grain boundary are comparable to the bulk values. Therefore, in the present work, we only calculate the attempt frequencies for Fe self-diffusion in the bcc and fcc bulk, and apply these values to the grain boundary diffusion.

The rate constants (Γ) are then tabulated in a rate catalogue and used as input data for the kinetic Monte Carlo (KMC) simulations.

4.1.9 Hessian Matrix and Vibrational Frequencies

The Hessian matrix is the matrix of second derivatives of the energy with respect to geometry. To calculate the Hessian matrix, finite differences are used, i.e. each ion is displaced in the direction of each Cartesian coordinate, and from the forces the Hessian matrix is determined. In the harmonic approximation, the elements of the Hessian matrix is given by:

$$H_{i,j} = \frac{\partial^2 E}{\partial x_i \partial x_j} \quad (4.18)$$

In order to calculate the vibrational frequencies, the Hessian matrix is

first mass-weighted:

$$H_{i,j}^m = \frac{H_{i,j}}{\sqrt{m_a^l * m_a^m}} \quad (4.19)$$

where m_a^i are the atomic mass. Diagonalization of this matrix yields eigenvalues, ε (force constants), from which the vibrational frequencies can be calculated:

$$\nu_i = \frac{1}{2\pi} \sqrt{\varepsilon_i} \quad (4.20)$$

In this work, we calculate the vibrational frequencies of the pure Fe system (ν_i), bulk Fe with one vacancy at the equilibrium position (ν_i^{eq}), and bulk Fe with one vacancy at the saddle-point (ν_i^{sp}).

4.2 Kinetic Monte Carlo Simulations

Unlike the bulk situation, the activation energies of the solutes in the interfaces depend on the positions. Consequently, there are a multiple of jump rates. To investigate solute diffusivities, a kinetic Monte Carlo (KMC) model is developed based on the detailed input from DFT calculations. KMC is an efficient method for carrying out dynamical simulations for a wide variety of stochastic and/or thermally activated processes. In contrast to the MD method which can generally only be carried out on a time scale of nanoseconds or less, KMC simulations can effectively overcome the time scale limitation, and the diffusion coefficients can be calculated at interfaces.

In the KMC model atoms are located on a rigid lattice. Diffusion occurs by vacancy exchange with a first nearest neighbor atom. At each KMC step, there are z possible vacancy jumps, where z is the coordination number. These jumps form a Markov process, which is simulated by the residence-time algorithm. In the present study, the residence time associated with the KMC step is given by [108]:

$$\tau_{kmc} = -\ln(u_{rand})/R_N \quad (4.21)$$

where u_{rand} is a random number uniformly distributed between 0 and 1, and R_N is the summation of the jump rate, i.e. $R_N = \sum_{j=1}^z \Gamma_j$. Here Γ_j is

the jump rate, which can be obtained according to Equation 4.16 based on the DFT calculations. The algorithm for KMC is outlined as the following procedure:

0. Set the time $t = 0$
1. Initialize the lattice structure by assigning the type of atoms to each lattice site.
2. Insert the vacancy into the lattice sites.
3. Start KMC loop over $N_{itermax}$ steps.
4. Define the local atomic configuration in each direction for the vacancy and extract the value of the energy barrier from the predefined table. Form a list of the rates Γ_j of all possible transitions in the system.
5. Calculate the cumulative function $R_N = \sum \Gamma_j$ for $j = 1 \dots z$.
6. Get a random number $x_{rand} \in (0, 1)$
7. Find the event to carry out j by finding the j for which $R_{j-1} < x_{rand}R_N \leq R_j$.
8. Carry out event j
9. Get a new random number $u_{rand} \in (0, 1)$
10. Update the time with $t_{kmc} = t_{kmc} + \tau_{kmc}$, where τ_{kmc} is determined by Equation 4.21.
11. Set $N_{iter} = N_{iter} + 1$. If $N_{iter} < N_{itermax}$, return to step 4.

For grain boundary diffusion, a thin boundary model is constructed. The vacancy moves randomly. At each step, the residence time of the vacancy at the current site is calculated from its jump rates in all possible directions. The clock is advanced after the vacancy leaves the site. As the vacancy walks, it also moves atoms around and induces their diffusion. Once the simulation is complete, the apparent diffusion coefficients (D_{app}) of the solute atoms are recorded according to the Einstein equation:[109]

$$D_{app} = \frac{\langle r^2(t) \rangle}{6 \cdot t} \quad (4.22)$$

where $\langle r^2(t) \rangle$ is the mean square displacement (MSD) of the diffusing solute atoms during time t .

According to the analysis of Porter and Easterling, if the grain boundary

has an effective thickness δ and the grain size is d_{gs} , the apparent diffusion coefficient (D_{app}) is expressed as [110]:

$$D_{app} = \left(1 - \frac{\delta}{d_{gs}}\right)D_l + \frac{\delta}{d_{gs}}D_b \quad (4.23)$$

where D_l and D_b are the bulk and grain boundary diffusivities. Since the bulk diffusivities D_l are calculated directly from DFT, the grain boundary diffusivities D_b can thus be determined. In this work, the results are obtained based on the 10^5 independent calculations at each temperature.

4.3 Molecular Statics Simulations

In this work, to extend our simulation of special grain boundaries using DFT calculations to more general grain boundaries, the molecular statics (MS) simulations are employed, which are performed using the LAMMPS code [111]. To obtain a reliable and accurate results, it is critical to choose suitable potentials U of the system.

The most widely used potential theories is embedded atom method (EAM) [112]. So far, there are several EAM based potential available for pure Fe, e.g. Johnson 1989 [113], Ackland *et al.* 1997 [114], and Mendeleev *et al.* [115]. Recently, Malerba *et al.* systematically compared the performance of these potentials for bcc and fcc iron [116]. They found that the results (e.g. lattice constants, bulk modulus, etc.) obtained by Mendeleev-type potentials were closer to DFT results than others, which make them currently the best choice in order to “extend density functional theory” to larger scales. Therefore, the EAM potential derived by Mendeleev *et al.* for pure iron has been employed in this work [115]. Although MS simulation are much more efficient than DFT calculations, they are still limited in their applications to only a few pure metals, and very few binary and ternary systems due to the lack of suitable interatomic potentials [36, 41, 42].

Similar to the DFT calculations, the models are relaxed using the conjugate gradient method to obtain the equilibrium structures.

Chapter 5

Interaction of Solutes with the $\Sigma 5$ (013) Tilt Grain Boundary in Iron

5.1 Grain Boundary Structure

The $\Sigma 5$ (013) tilt grain boundary is constructed according to the coincidence site lattice (CSL) theory by rotating two bcc grains by 36.9° about the $\langle 100 \rangle$ axis [63]. This grain boundary has mirror symmetry with respect to the (013) boundary plane. The grain boundary structure is shown in Figure 5.1. As in the bulk calculations, periodic boundary conditions are employed such that the supercell contains two grain boundaries. Solutes are placed at the substitutional sites within one grain boundary only. In Figure 5.1, the letters *a*, *b*, and *c* refer to different boundary positions.

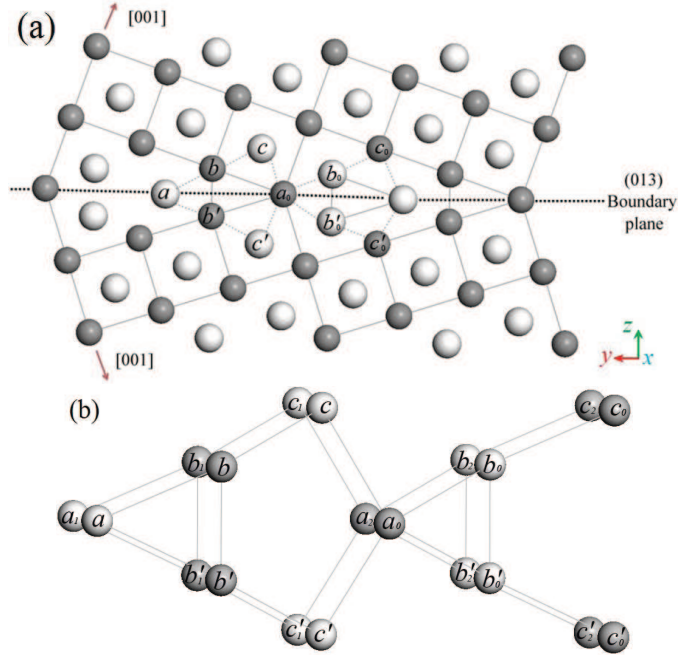


Figure 5.1: (a) Side view of the $\Sigma 5$ (013) symmetrical tilt grain boundary. The lighter and darker circles represent Fe atoms in different (100) atomic planes. (b) Atomic structure of the boundary sites. The letters a , b , and c refer to different boundary positions. The superscript ($'$) indicates the symmetric position with respect to the (013) boundary plane. The subscript identifies different boundary unit cells of the $\Sigma 5$ (013) grain boundary.

5.2 Grain Boundary Energy

As discussed in Chapter 4, the supercell size was determined from calculation of the grain boundary energy as a function of inter-boundary distance. In Figure 5.2, it is clear that the grain boundary energy is converged when the distances are larger than 9.0 Å. In order to balance accuracy of results and computational load, we adopt a supercell of 120 lattice sites with the dimensions of $8.52 \times 8.98 \times 18.0$ Å³. The calculations were performed using a $4 \times 4 \times 2$ Monkhorst-Pack k -point mesh.

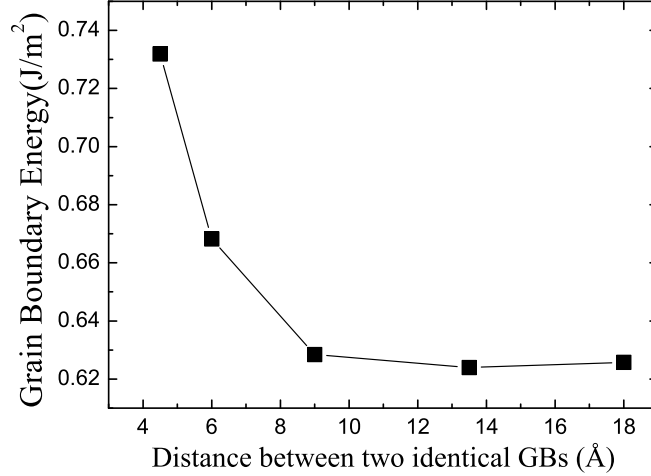


Figure 5.2: Grain boundary energy as a function of distance between grain boundaries.

5.3 Single Solute Segregation Energies

We first investigate the solute segregation behavior in the $\Sigma 5$ tilt grain boundary in bcc Fe. The binding energy of solutes with the grain boundaries (i.e. segregation energy) is calculated according to Equation 4.10. The calculated binding energies for various grain boundary positions are summarized in Figure 5.3. We find that segregation to the grain boundary is energetically favorable for all solutes and boundary sites considered in this work. Furthermore, interactions between solute atoms and grain boundary are short-range and limited to about 2~3 atomic layers. On the other hand, different solutes prefer different positions at the grain boundary. For example, the binding energy for Nb, Ti, and Mo atoms are the largest in position *a*, whereas other elements such as Si, V, Cr, Mn, Co, Ni, and Cu prefer position *b*.

In order to compare with the experimental results, it would be useful to average the binding energy. In this work, two different ways of finding the average binding energies are employed, i.e. the simple numerical averaging

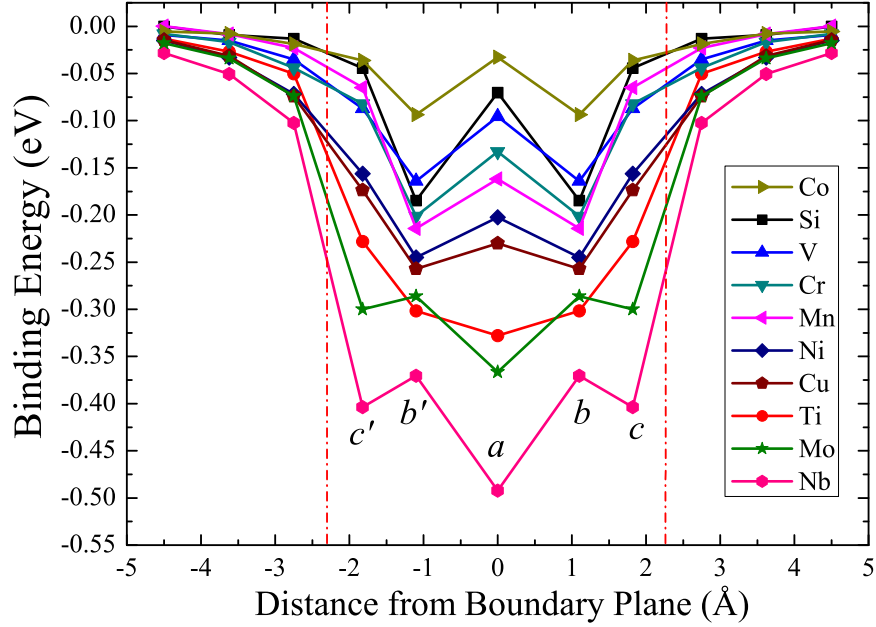


Figure 5.3: Binding energies for substitutional solutes at the $\Sigma 5$ (013) tilt grain boundary as a function of distance from the boundary plane; a , b , c , b' , and c' refer to the boundary sites as labeled in Figure 5.1.

method and the Langmuir-McLean approach. The numerical method simply averages the binding energies over the five boundary sites, i.e. a , b , c , b' , and c' , whereas the Langmuir-McLean approach is a more sophisticated method, which would be more relevant for solute segregation.

Based on the Coghlan-White approach, if the grain boundary has multiple types of site, the segregation to each type of site is calculated individually, then a weighted average is performed to get the total grain boundary segregation. So for a number of different types of site (i), each with binding energy, E_{seg}^i , the segregation to that type of site is found through simple Langmuir-McLean equation [117, 118]:

$$\frac{c_{gb}^i}{1 - c_{gb}^i} = \frac{c_{bulk}}{(1 - c_{bulk})} \exp\left(-\frac{E_{seg}^i}{k_B T}\right) \quad (5.1)$$

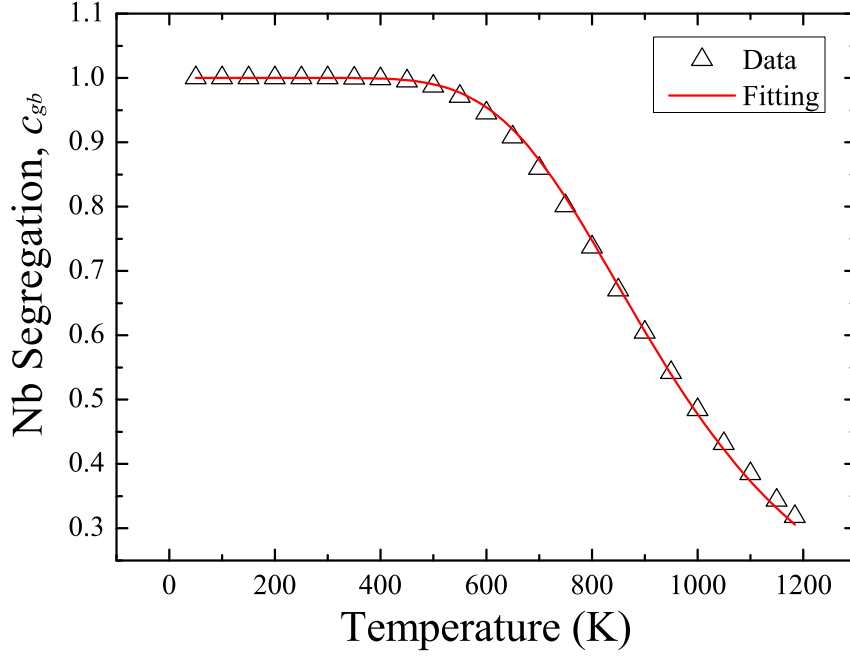


Figure 5.4: Total grain boundary segregation of Nb as a function of temperature in $\Sigma 5$ grain boundary in Fe. The symbols are calculated according to Equation 5.3, while the line is the Langmuir-McLean fit.

where c_{gb}^i is the solute concentration at the boundary site i , and c_{bulk} is the solute concentration in the bulk. Coghlan and White rewritten Equation 5.1 as:

$$c_{gb}^i = \frac{c_{bulk} \exp\left(-\frac{E_{seg}^i}{k_B T}\right)}{1 - c_{bulk} + c_{bulk} \exp\left(-\frac{E_{seg}^i}{k_B T}\right)} \quad (5.2)$$

Then the total grain boundary segregation is a weighted average summed over all grain boundary sites, which is expressed as:

$$c_{gb} = \sum_i (F_i c_{gb}^i) \quad (5.3)$$

where F_i is the fraction of the grain boundary sites that have binding

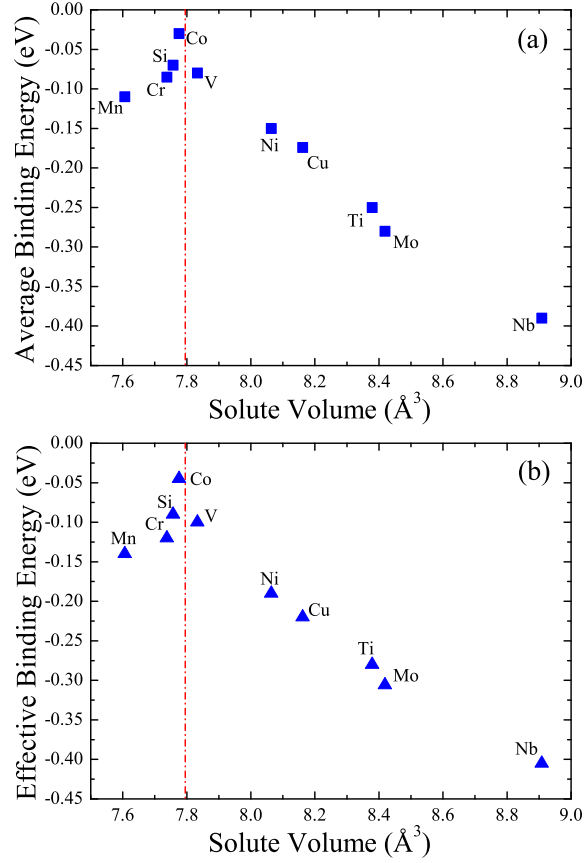


Figure 5.5: (a) The average binding energies, and (b) the effective binding energies of solutes as a function of solute atomic volume. The dotted line indicates the atomic volume of Fe in the bcc lattice.

E_{seg}^i . In Figure 5.4, the total segregation (c_{gb}) of Nb as a function of temperature is plotted. It is clear that c_{gb} decreases with the increase of temperature. We then fit these data according to Langmuir-McLean equation and obtain the effective binding energies, i.e. E_{seg}^{eff} .

Figure 5.5a shows the simple numerical averaged binding energies. The results are plotted as a function of solute volume (V_s). In Figure 5.5b, the effective segregation energies of solutes, which are obtained based on the Langmuir-McLean approach, are shown as a function of solute volume.

The two averaging approaches lead to very similar characteristics of solute segregation in the $\Sigma 5$ grain boundary.

In this work, the solute volume was computed from relaxed atomic positions in the bulk lattice according to the touching hard-sphere model: the radius of Fe is defined as half of the Fe-Fe nearest neighbor (NN) distance; solute radii are found by subtracting the Fe radius from the solute-Fe nearest neighbor distance [119]. In Figure 5.5, there is a distinct correlation between the average segregation energy and solute volume, i.e. the magnitude of E_{seg} and thus the tendency for segregation increase with solute size. Evidently, for large solute, such as Nb, Mo, etc. the elastic strain induced by the substitutional solutes in the bulk lattice can be partially relieved at the grain boundary where the packing density is reduced. In contrast, solutes whose size is similar than that of Fe do not introduce large lattice distortions and hence exhibit much smaller segregation energies. Similar size dependent trends were reported for vacancy-solute binding and diffusion in Mg [119, 120].

To further illustrate the influence of the solute volume on segregation, we show in Figure 5.6 the change in electron density in the (100) plane as calculated from the difference between the electron density of the pure system and the system containing one solute atom in position a . The plots are shown for Co and Nb because they represent the two extremes of lattice distortion that the investigated substitutional solutes introduce in the bulk. The bulk lattice distortion due to Co is very small (less than 0.003\AA decrease in Co-Fe distance with respect to Fe-Fe distances in the bulk). As compared to Fe, Co has one extra nuclear charge which is screened by the electron density within about 1.0\AA radius from the nucleus (see Figure 5.6(a)). In contrast, Nb $4d$ orbitals are much more spatially extended leading to significant and rather asymmetric leakage of charge towards neighboring Fe atoms (see Figure 5.6(b)). The complexity of this charge distribution demonstrates the difficulty in defining an effective solute volume at the grain boundary where the symmetry constraints are lifted. This could be exceptionally problematic when the valence states of the solute and the host are of very different origin.

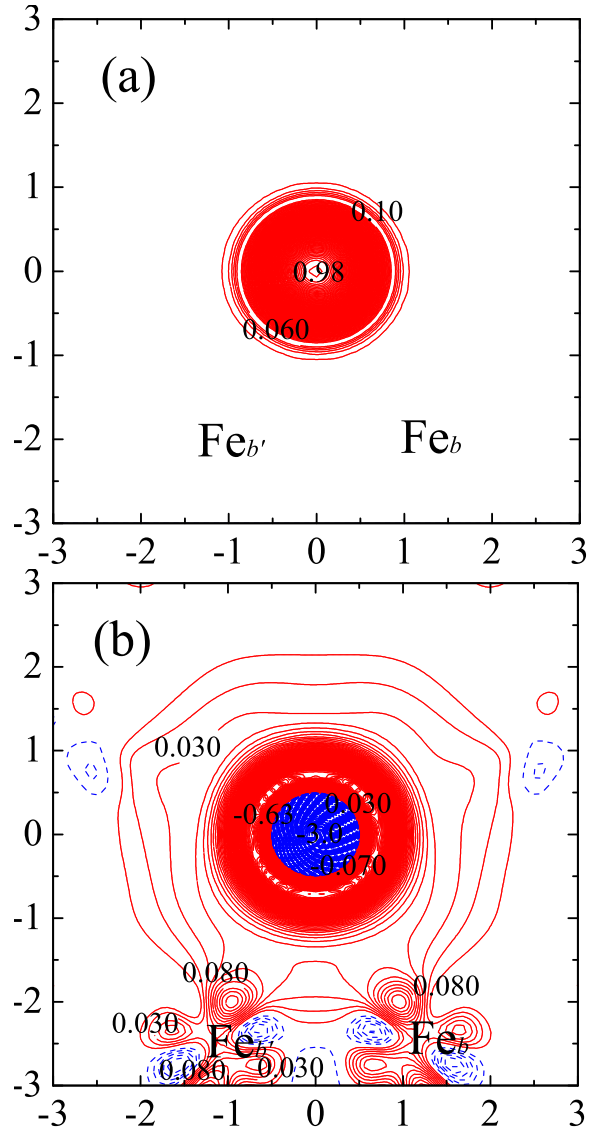


Figure 5.6: Valence electron density difference contour maps in the (100) plane for (a) Co-, and (b) Nb- segregated at boundary position a with respect to the non-segregated grain boundary (in units of $e/\text{\AA}^3$ with a contour spacing of $0.01 e/\text{\AA}^3$). The solid red and dashed blue lines indicate gains and losses in electron density, respectively.

A comparison between theory and experiments is limited by the lack of experimental data (especially for the $\Sigma 5$ (013) tilt boundary). Nonetheless, the reported segregation enthalpy for Si ($-9 \pm 3.5 \text{ kJ/mol}$) [121] agrees well with our calculation of -8.7 kJ/mol for the effective binding energy based on the Langmuir-McLean approach. The experimental segregation energies of Mn and Nb to random grain boundaries are -11 kJ/mol and -29 kJ/mol [122, 123], respectively. These values are comparable with our predictions of -14 kJ/mol and -39 kJ/mol , respectively, for the $\Sigma 5$ boundary. In addition, our calculation indicates that the binding energies of Nb, Mo, and Ti with the grain boundary are comparatively large, and the segregation of Nb is the most pronounced among all investigated cases. Overall larger binding energies indicate stronger interactions with the grain boundary. Such strong interactions are expected to delay grain growth and recrystallization. All these effects are actually observed in the case of Nb and Mo in agreement with our prediction of rather large binding energies for these elements [123, 124].

5.4 Solute-solute Interactions at the Grain Boundary

After having considered segregation of a single solute atom, let us now turn to solute-solute interaction and its contribution to the grain boundary segregation energies. As has been discussed above, the size difference between smaller and larger solutes is reflected in their preference to segregate at particular sites. Smaller solutes prefer to occupy b positions whereas larger solutes segregate at position a (Figure 5.3). Therefore, we select these two positions for detailed analysis of solute-solute interactions at the grain boundary.

Figure 5.7 shows the calculated segregation energies according to Equation 4.11 for various solutes segregating at boundary site a (Figure 5.7(a)) or b (Figure 5.7(b)) while the same kind of solute is already present at another boundary position. The segregation energies of a single solute are also shown for comparison. The predicted trends are similar in both scenarios, i.e.

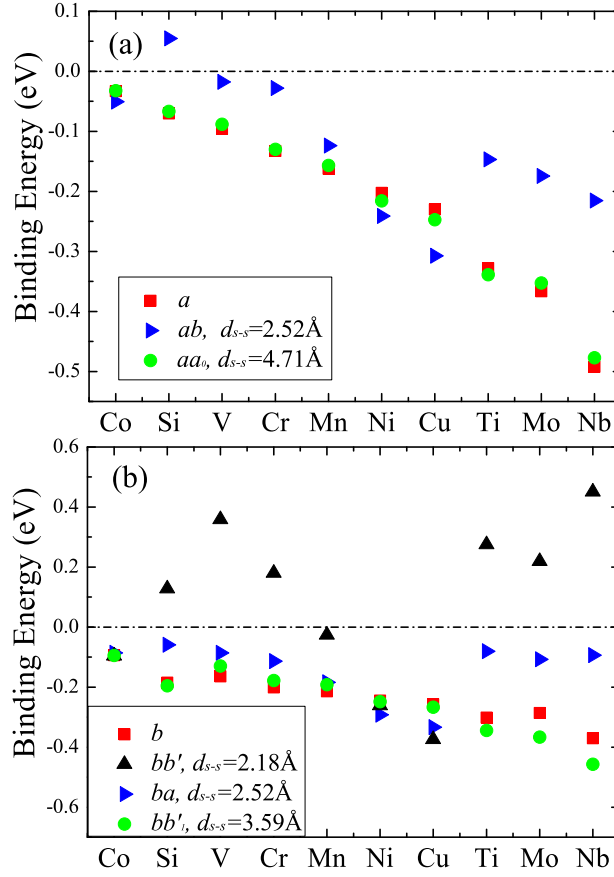


Figure 5.7: Binding energies for a second solute atom segregating at (a) boundary position *a*, and (b) boundary position *b* when the same solute is already present at another boundary site. The square symbols indicate the binding energies of a single solute atom.

Figure 5.7(a) and 5.7(b). For Co, Ni and Cu, co-segregation energies are very close to the segregation energies of individual solutes. For all the other investigated cases, the presence of one solute atom decreases the solute-grain boundary segregation energies for the second solute atom when two solute atoms occupy nearest neighbour positions.

For short solute-solute distances, i.e. 2.18\AA , which is about 90% of the nearest neighbor distance in the pure bulk lattice, the repulsive interaction

may be strong enough to make segregation of the second solute atom unfavorable (Figure 5.7(b)). Nonetheless, for spacing of 2.52 Å and larger, the segregation energies for the second solute atom are negative except for Si at 2.52Å, suggesting that these positions remain favorable for solute segregation albeit with a reduced tendency of segregation. An exception to this tendency are the larger solutes (Nb, Ti, Mo) which show an increase of up to 30% in the magnitude of the segregation energy when they occupy two neighboring *b*-sites (Figure 5.7(b)). As the solute pair distance becomes larger, the influence of the first solute on the segregation energies of the second solutes gradually vanishes. As shown in Figure 5.7(a), when the two solutes occupy neighboring sites *a* separated by a distance of 4.71 Å, the segregation energies of the second solute atoms are, within the accuracy of the calculations, the same as the segregation energies of a single solute atom at the same site. These results suggest that even a high symmetry grain boundary, such as $\Sigma 5$, can support a rather significant solute enrichment.

To analyze the solute-solute interaction in more detail, we calculate the effective interaction (E_{eff}) as a function of solute-solute distance for both the bulk and the grain boundary according to Equation 4.12. Evidently, full mapping of such interactions for the grain boundaries involves a rather large number of permutations. To minimize the number of calculations, we fix one solute atom in position *b* while the other solute atom occupies other boundary positions. The results for solute-solute interactions as a function of solute pair distance in the grain boundary are shown in Figure 5.8. For comparison, the effective interactions between these solute pairs in the bulk lattice from first to fifth nearest-neighbor positions are also plotted.

In Figure 5.8, Cu shows attractive interactions. While for all the other investigated cases, repulsive interactions are observed. Overall, we find four major solute-specific contributions to the effective interactions: contributions from the elastic energy induced by atomic size misfit, contributions from competing magnetic interactions, contributions from magnetically driven clustering, and contributions from chemical bonding.

The elastic contribution to solute-solute interaction can be estimated using the classical elasticity theory [125, 126]. According to the Eshelby

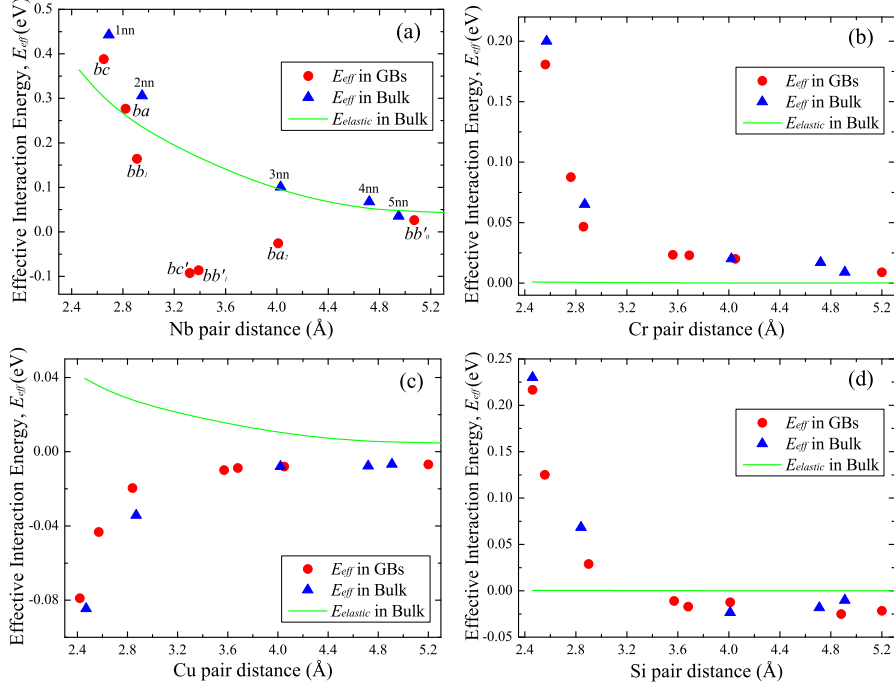


Figure 5.8: Pair interactions for (a) Nb, (b) Cr, (c) Cu, and (d) Si in the Fe bulk and at the $\Sigma 5$ (013) grain boundary.

model, the elastic interaction energy between two solute atoms as a function of their distance d is given by:

$$\varepsilon_{elast} = \frac{0.3}{\gamma_{el}} \Delta V^2 \left(\frac{\alpha_{el}}{d^3} \right) \quad (5.4)$$

where ΔV is the volume difference between solute and Fe atom. The parameters α_{el} and γ_{el} are related to the elastic constants C_{ij} of pure Fe: $\alpha_{el} = C_{11} - C_{12} - 2C_{44}$, and $\gamma_{el} = (C_{11} + 2C_{12})/3C_{11}$. The following elastic constants were obtained from DFT calculations for bcc bulk Fe: $C_{11} = 243.6$ GPa, $C_{12} = 137.4$ GPa, and $C_{44} = 120.9$ GPa. Then, the bulk modulus $K = (C_{11} + 2C_{12})/3 = 172.8$ GPa is obtained which agrees well with the experimental value of 171.6 GPa [127] and the previous DFT result of 175.0 GPa [128]. The calculated elastic interactions for solute pairs in the bulk are depicted in Figure 5.8 by the solid lines.

The elastic contribution to the solute-solute interaction is determined by the relative size of solutes with respect to Fe. As the size of solutes increases, the elastic contribution to solute-solute interactions becomes increasingly more important. As shown in Figure 5.8(a), Nb-Nb interactions in the bulk are comparable to those predicted by the classical elasticity theory. They are, however, different at the grain boundary. When two Nb atoms occupy grain boundary positions at intermediate pair distances (bb'_1 and bc' pairs), the effective interaction between Nb becomes attractive. This is because the packing density is low at these boundary positions, which gives rise to large excess volume. As a result, the substantial elastic strain can be efficiently relieved thereby favoring the Nb-Nb binding. Similar trends were also found for other larger solute atoms, i.e. Mo-Mo and Ti-Ti (see Figure 5.7(b)).

From elastic considerations alone, one would expect to find rather small effective interactions between Mn, Cr, V, Co and Si in Fe. However, a strong repulsion between two Cr atoms is clearly evident in our DFT calculations (see Figure 5.8(b)). In fact, it is only a factor of two smaller than the Nb-Nb nearest neighbor repulsion, which is predominantly elastic. Such a strong repulsion can be attributed to magnetic frustration. To better show the influence of the competing magnetic interactions, the magnetic moments for each solute atom in Fe matrix are calculated. Since solute-matrix magnetic interaction varies from one solute to another, the single solute bulk and grain boundary calculations were performed with ferro- and antiferro- initial spin arrangements between solute and matrix.

In agreement with previous work, we find anti-ferromagnetic (AFM) ground state for Ti, V, Cr, Mn, Nb and Mo [129, 130]. For Co, Ni and Cu, the ferromagnetic (FM) state has the lowest total energy. In systems with two solutes and for large solute-solute distances, the initial magnetic configurations are chosen according to the solute-matrix coupling found in the bulk calculations. However, we check if other possible magnetic configurations can be converged for the short solute-solute distances. In cases where several magnetic solutions are found, we use the one with the lowest total energy.

The calculated magnetic moments for solute atoms in grain boundaries

Table 5.1: Magnetic moments (μ_B) for single solute in grain boundary (GB) and bulk sites.¹

	<i>a</i>	<i>b</i>	<i>c</i>	<i>average</i>	<i>bulk</i>
Si	-0.12	-0.14	-0.11	-0.12	-0.10
Nb	-0.70	-0.60	-0.69	-0.66	-0.75
Mo	-0.81	-0.66	-0.69	-0.70	-0.77
Ti	-0.79	-0.64	-0.69	-0.70	-0.77
Cu	0.09	0.14	0.11	0.12	0.17
Ni	0.78	0.77	0.81	0.79	0.84
Co	1.65	1.60	1.69	1.65	1.71
Mn	-2.40	-1.81	-1.85	-1.94	-1.77
Cr	-2.33	-1.68	-1.71	-1.82	-1.79
V	-1.41	-1.09	-1.21	-1.20	-1.25

¹ The sign of the solute magnetic moment is positive (negative) if the magnetic moment is parallel (anti-parallel) to that of Fe

and the bulk structure are listed in Table 5.1. Note that the predicted magnetic moments are essentially the same in the bulk and in the grain boundary. Further, they change by less than 1% if two solute atoms are brought close to each other. Thus, magnetic moments of single solute atoms as shown in Table 5.1 can be used to infer magnetic interactions.

The magnetic moments for Cr (Mn and V) are large compared with those of other alloying elements, suggesting that the effects due to magnetic frustration are of significance for Cr (Mn and V). In the dilute limit, this AFM coupling increases the energy of the system when two solutes occupy adjacent sites in an otherwise ferromagnetic (FM) host material. Olsson *et al.* reached similar conclusions in recent bulk calculations [130]. Moreover,

Levesque *et al.* showed that by constraining the Cr local moments to zero, one can reduce Cr-Cr interactions to negligible values [131]. Our findings demonstrate that the interactions between 3d TMs in the grain boundary are similar to those in the bulk.

Compared to Nb and Cr, the Cu case appears at first surprising as one would expect relatively weak repulsive Cu-Cu interactions due to its moderate size and a lack of local magnetic moment. As shown in Figure 5.8(c), however, Cu shows an attractive interaction indicating possible clustering, which is consistent with the observations that Cu impurities have a pronounced tendency to segregate from the matrix [132, 133]. Since all Cu *d*-orbitals are occupied, it is natural to think of Cu as non-magnetic solute. By employing the simple Heisenberg model, one can estimate that a single Cu impurity would cost the magnetic energy by $8J_1$ in bcc iron, where J_1 is the exchange parameter in the first coordinate shell. Evidently, it is doubled when two Cu impurities are far apart. By combining them in a pair, one can reduce the penalty in magnetic energy by $2J_1$ that accounts for about 70% of the interaction energy using the value calculated by Ruban *et al* [134]. This is, of course, a rather crude estimate since it only accounts for the nearest neighbor exchange interactions. Nonetheless, we find that Cu-Cu interaction energy is reduced by an order of magnitude when the magnetism is switched off in the calculations. Thus, the attractive Cu-Cu interaction can be viewed as a magnetically driven clustering.

From Figure 5.8(d), it is evident that a short-range repulsive interaction occurs when Si atoms come sufficiently close to each other, within 3 or 4 Å. Unlike the TMs, the origin of this repulsive force is based on the fact that Si atoms prefer to bond with Fe atoms instead of with other Si atoms. In fact, the binding energy per one Si atom in bulk Si is -1.14 eV, which is appreciably smaller (absolute value) than those in Fe-Si alloys, i.e. -1.87 eV. This indicates that the electronic levels of Fe-Si bonding are formed in an energetically deeper range than those of Si-Si bonding. In this case, most electrons of Si are expected to contribute to Fe-Si bonds rather than Si-Si bonds. As a result, a short-range repulsive interaction occurs for Si-Si pair in the Fe matrix.

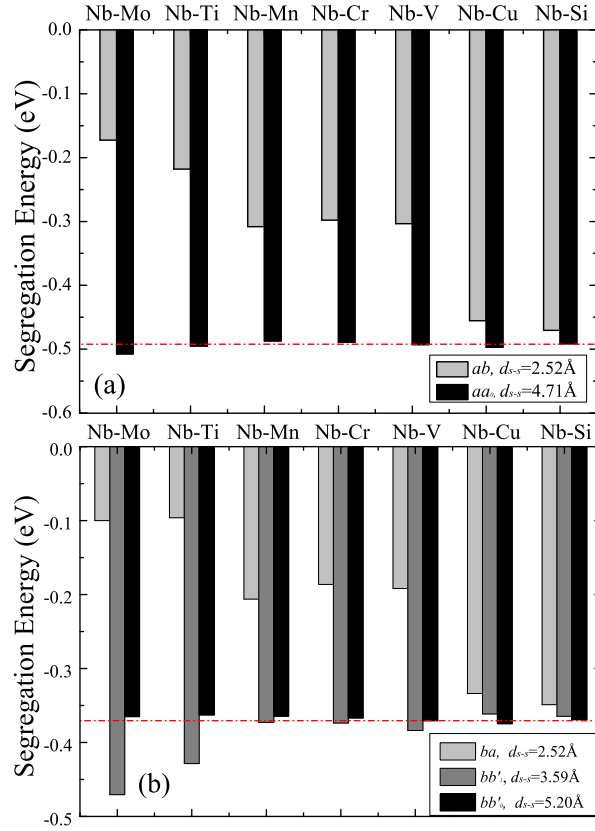


Figure 5.9: Binding energies for the grain boundary with Nb segregating at (a) boundary position *a*, and (b) boundary position *b* when another solute (i.e. Mo, Ti, Mn, Cr, V, Cu, or Si) is already present at a neighboring site indicated by the second letter. The dotted line indicates the binding energies for a single Nb atom.

Steels usually contain several alloying elements each intended to affect microstructure and properties in specific ways. Here, we study the segregation energy of Nb, the largest solute in our set, to sites *a* and *b* in the grain boundary when another solute of a different type is already present at a neighboring site. As shown in Figure 5.9, the segregation energy is strongly dependent on the relative solute positions. The variation is particularly pronounced when the other solute is of large size, i.e. for the Nb-Mo and

Nb-Ti combinations. For a solute-solute distance of 2.52 Å, the magnitude of the Nb segregation energy is reduced in these two cases by about 60% (Figure 5.9(a)) and 75% (Figure 5.9(b)), respectively, as compared to the case of a single Nb atom. The reduction is about 50% for Mn, Cr, or V. For the Si-Nb and Cu-Nb cases the segregation energy of Nb is only marginally affected (by less than 30 meV). When the separation distance between the two sites is increased, the Nb segregation energy quickly approaches that for a single Nb atom. For intermediate distances, however, an increase in the magnitude of the segregation energy is predicted for selected cases, in particular for Ti-Nb and Mo-Nb (see Figure 5.9b). These findings are similar to those for the Nb-Nb co-segregation (see Figure 5.7).

5.5 Molecular Statics Simulations

The above DFT calculations indicate that the excess volume at boundary sites is an important parameter to predict the segregation tendency of solutes at grain boundaries. This is in particular of significance for large solute atoms (i.e. Nb, Mo, and Ti) that are crucial alloying or microalloying elements in advanced high-strength steels. Since most steels and other polycrystalline materials are primarily composed of random boundaries rather than special Σ boundaries, it is useful to evaluate to what extent DFT calculations for these special boundaries remain of merit for more general grain boundaries. Here, we consider the excess volume of boundary sites as an indicator for this evaluation. For this purpose, a series of molecular statics (MS) simulations were performed.

As in DFT calculations, the symmetrical [100] tilt grain boundaries were constructed by rotating two bcc grains about the [100] axis with the rotation angles ranging from 10° to 44° to obtain higher order Σ boundaries. In this work, nine different tilt grain boundaries, i.e. $\Sigma 5$, $\Sigma 13$, $\Sigma 17$, $\Sigma 25$, $\Sigma 29$, $\Sigma 37$, $\Sigma 41$, $\Sigma 53$, and $\Sigma 61$, are employed to study the excess volume at the boundary region. For all these investigated cases, two identical grain boundaries were included in the MS simulation block to maintain the periodic boundary conditions. The length between two grain boundaries

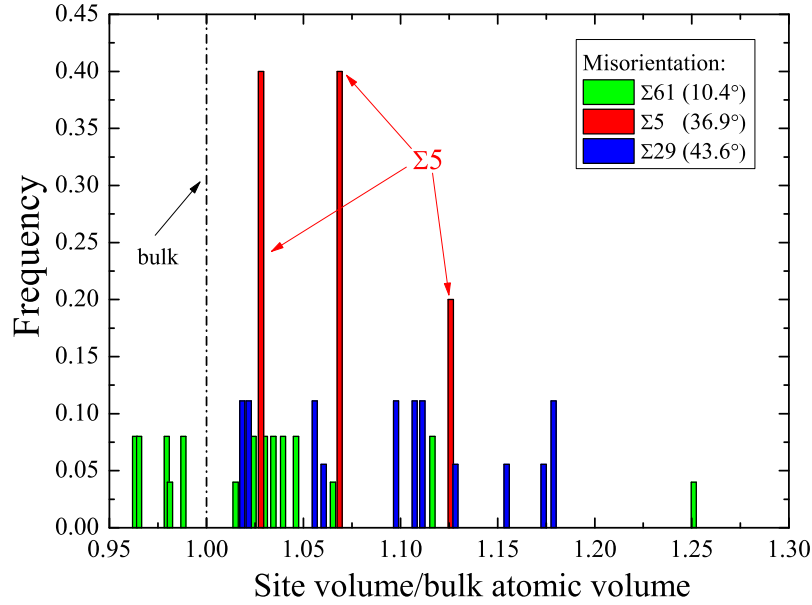


Figure 5.10: Site volume distribution in $\Sigma 5$ (36.9°), $\Sigma 29$ (43.6°) and $\Sigma 61$ (10.4°) grain boundaries.

is separated by at least 20 nm, which is sufficient large to eliminate the interaction effects from each other.

The atomic volumes are calculated by constructing Voronoi polyhedra (VP) for each site in the grain boundary. For a particular center atom, VP is defined as the volume of space containing all points closer to this center atom than to any other atoms. The faces of this polyhedron are perpendicular bisectors of the vectors connecting the center atom to its nearest neighbors. Figure 5.10 shows the site volume distributions for $\Sigma 5$ (36.9°), $\Sigma 29$ (43.6°) and $\Sigma 61$ (10.4°) grain boundaries. The $\Sigma 29$ boundary is selected because it has the largest misorientation angle in our set. On the other hand, the $\Sigma 61$ boundary has the least number of coincident sites in our set and hence is the most random boundary considered. The site volumes are given in units of the atomic volume in the bulk. One can see that these distributions are asymmetric and extend to up to 25% increase in volume with respect to the bulk value.

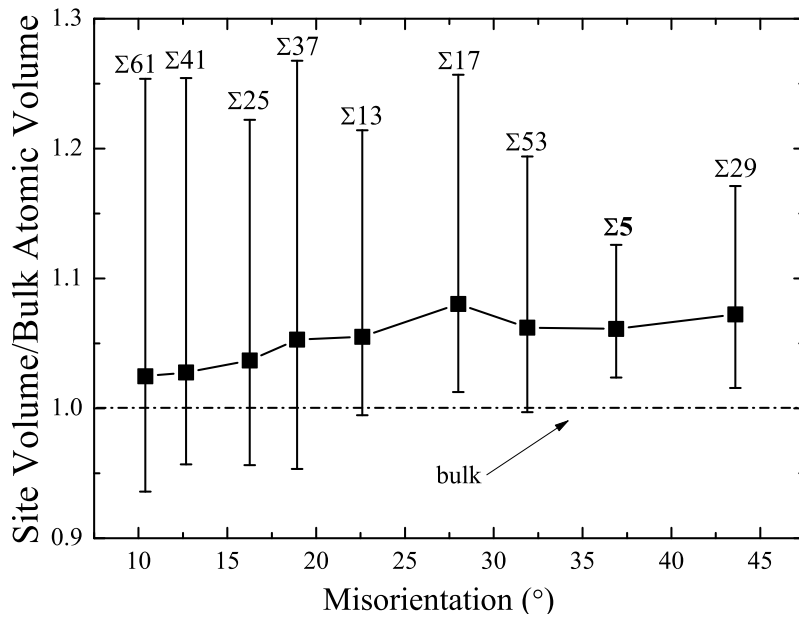


Figure 5.11: Averaged atomic volume as a function of grain boundary misorientation angle. The bars indicate the maximum and the minimum atomic volume of the boundary sites.

The average volumes for all nine boundaries are shown in Figure 5.11 as a function of misorientation angle with the vertical lines representing the range of values for each boundary. The average excess volume for the $\Sigma 5$ grain boundary is similar to that of more general boundaries but the range is narrower. Nevertheless, based on the data shown in Figure 5.10 and 5.11, it is reasonable to assume that, in a first approximation, calculations for the $\Sigma 5$ grain boundary provide trends which remain applicable to random grain boundaries. This is also consistent with the predicted trend of segregation energies that matches general observations of the role of the investigated solutes on overall recrystallization and phase transformation behavior in low-carbon steels.

Chapter 6

First-Principles Study of Face-Centered Cubic γ -Iron

6.1 Bulk and Grain Boundary Structures in γ -Fe

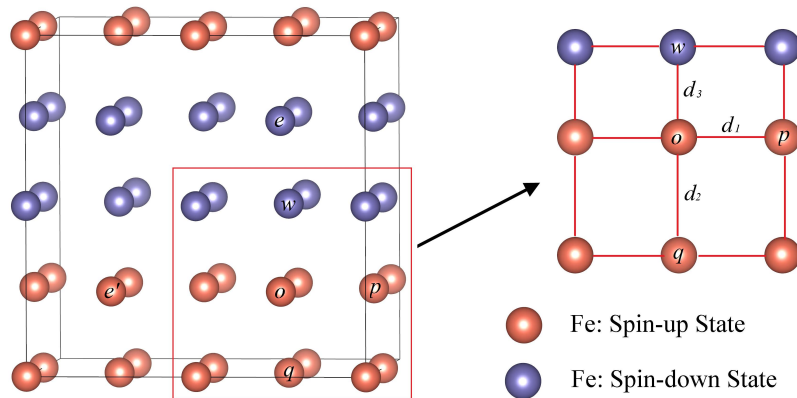


Figure 6.1: Fe fcc lattice structure with AFMD magnetic configurations. Red and blue circles indicate spin-up and spin-down magnetic states. The letters o , p , q , w , e , and e' are used to label the different positions in the fcc bulk.

For fcc bulk simulations, the calculations are performed using a supercell of 256 lattice sites for fcc Fe with double-layer anti-ferromagnetic (AFMD)

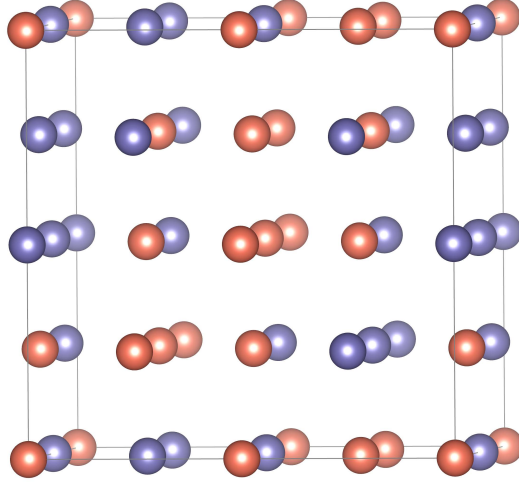


Figure 6.2: SQS-32 structure for fcc Fe lattice. The red and blue ball indicate spin-up and spin-down states.

arrangement. For this supercell, the Monkhorst-Pack $2 \times 2 \times 2$ k -point mesh is used [99] to sample the Brillouin zone. Figure 6.1 shows the fcc bulk structure with AFMD magnetic configurations. It is noticeable that there exists local structure distortions. As illustrated in Figure 6.1b, each site (o) has three types of nearest neighbors, namely p , q , and w . The distance between $\text{Fe}^\uparrow\text{-Fe}^\downarrow$, i.e. d_3 is 0.1 \AA shorter than the distance between $\text{Fe}^\uparrow\text{-Fe}^\uparrow$ ($\text{Fe}^\downarrow\text{-Fe}^\downarrow$), i.e. d_2 , while d_1 keeps the same value before and after relaxation. Such distortion only occurs within the first nearest neighbor separation. For the second nearest neighbors, we get $d_{oe} = d_{oe'}$.

In this work, the non-magnetic (NM), ferromagnetic (FM), and anti-ferromagnetic (AFM) states are also studied to check the relative stability of the collinear magnetic configurations. For this purpose, a conventional fcc Fe unit cell containing 4 lattice sites with a k -point mesh of $8 \times 8 \times 8$ is employed.

To investigate the special quasi-random structure (SQS) and non-collinear magnetic arrangement, a supercell of 32 lattice sites is used in this work. The optimum SQS-32 configuration is shown in Figure 6.2, which is identical with Pezold's work [135]. The non-collinear configuration is

employed from the work of Antropov *et al.* [136]. The calculations are performed using a $4 \times 4 \times 4$ Monkhorst-Pack k -point mesh.

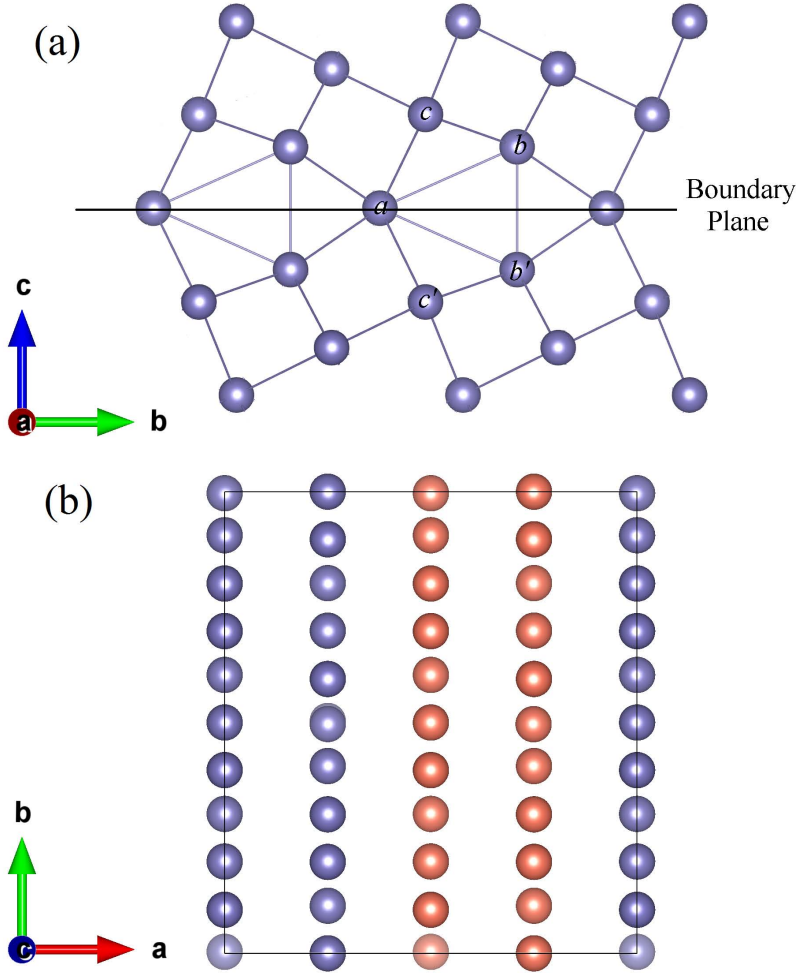


Figure 6.3: (a) Side view of the Fe $\Sigma 5$ fcc grain boundaries with AFMD magnetic configurations. (b) Top view of the supercells. Red and blue circles indicate spin-up and spin-down magnetic states.

In a similar manner to the bcc grain boundary, the $\Sigma 5$ fcc Fe grain boundary is constructed according to the coincidence site lattice (CSL) theory by rotating two bcc grains about the $\langle 100 \rangle$ axis [63]. The grain

boundary structure is shown in Figure 6.3. To describe the magnetic state of fcc phase, AFMD magnetic configuration is employed. As illustrated in Figure 6.3b, along a -axis, i.e. $\langle 100 \rangle$ direction, the AFMD phase has two layers spin up and the next two layers spin down. In this work, we adopt a supercell of 80 lattice sites with the dimensions of $7.1 \times 7.94 \times 16.0 \text{ \AA}^3$. The calculations are performed using a $4 \times 4 \times 2$ Monkhorst-Pack k -point mesh.

6.2 Magnetic Configurations for γ -Fe

Previous DFT calculations indicate that the double-layer anti-ferromagnetic (AFMD) state has the lowest total energy for fcc Fe (see Chapter 2 for details). Therefore, in the following calculations, we mainly focus on the AFMD magnetic configuration. In Figure 6.4, the AFMD, special quasi-random structure (SQS), and non-collinear (NC) configurations vs. the atomic volume for Fe are displayed. The calculated lattice parameters (a_l), and local magnetic moments (MM) for various magnetic phases of bulk α - and γ -Fe at 0 K are shown in Table 6.1. For comparison, the previous DFT calculations and experimental results are also listed.

In this work, we have not only concentrated on (001) magnetic layered structures, i.e. AFMD_[001], but also considered other planar structures, such as AFMD_[111] and AFMD_[110] (i.e. stacked along [111] and [110] direction). In agreement with previous work, the AFMD_[001] state was found to possess the lowest total energy among all investigated collinear states. In this study, the SQS magnetic configuration is considered to represent the paramagnetic arrangements in the same way as one deals with random alloys. In SQS structure, the spin-up and spin-down states are quasi-randomly distributed, which can give more realistic results for paramagnetic γ -Fe.

According to the Heisenberg model, it is possible to use non-collinear magnetism and start by setting up randomized initial spins, which was considered in earlier studies of the non-collinear magnetism in γ -Fe [82, 83]. In agreement with the previous work [82], our results indicate that the ground state of γ -Fe is a non-collinear state. However, in Figure 6.4, the energy difference between non-collinear state and the AFMD_[001] order is

Table 6.1: Predictions of lattice parameters (a_l), and magnetic moments (MM) for magnetic phases of α and γ -Fe at 0 K. Earlier DFT and experimental results are also shown for comparison.

System	a_l (\AA)			MM (μ_B)	
	Our results	Previous work	Exp. ¹	Our results	Previous work
α -Fe					
FM	2.84	2.84 [137]	2.85 [138]	2.20	2.20 [74]
γ -Fe					
NM	3.45	3.45 [137]			
LS FM	3.48	3.48 [137]		1.04	1.00 [137]
HS FM	3.64	3.64 [137]	3.65 [138]	2.56	2.60 [137]
AFM ² _[001]	3.49	3.49 [137]		1.34	1.33 [137]
AFMD ² _[001]	3.55	3.54 [137]		1.98	1.94 [137]
AFMD ³ _[111]	3.47			0.91	
AFMD ⁴ _[110]	3.51			1.70	
SQS	3.52			1.61 ⁵	
NC (PM)	3.55	3.55 [82]	3.56 [138]		

¹ The lattice constants are extrapolated to 0K according to the linear thermal expansion

² Stacked along [001] orientation

³ Stacked along [111] orientation

⁴ Stacked along [110] orientation

⁵ Averaged results for Fe with spin-up (or spin-down) states

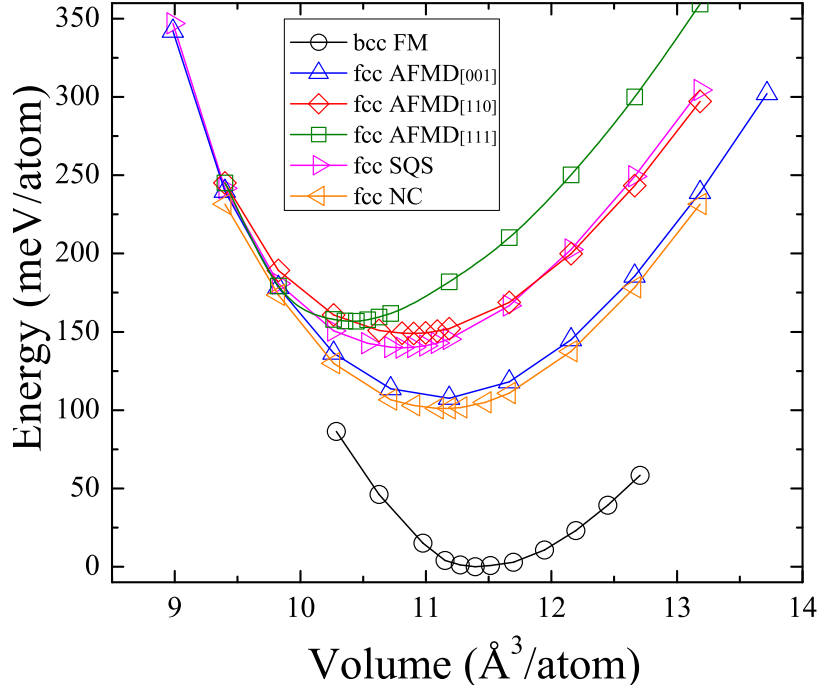


Figure 6.4: Various magnetic configurations vs. lattice constant in fcc Fe. The bcc ground state is set to be the reference (zero) state.

only a few meV/atom, and the lattice constants for these two structures are found to be the same. Moreover, Ackland *et al.* found that most of the non-collinear calculations for the γ -Fe with defects converged to collinear magnetic states [84]. Only few configurations remain non-collinear structures. However, the energy of the non-collinear configuration was only marginally lower than the collinear results. On the other hand, the non-collinear calculations are extremely time-consuming. For these reasons, we have not used it for the further calculations. In the following calculations, we use the AFMD_[001] and SQS configurations to describe the magnetic states of the fcc Fe.

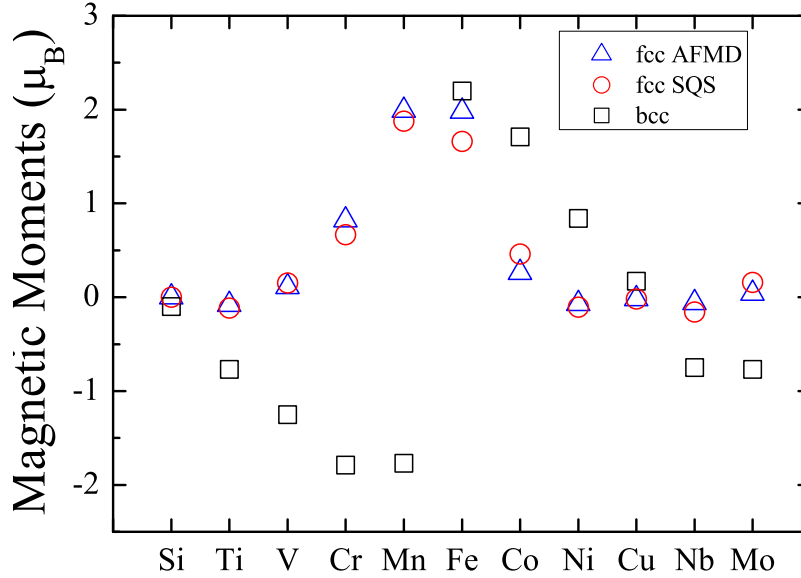


Figure 6.5: Magnetic moments for solute atoms in bcc and fcc Fe matrix. The x -axis is arranged in ascending order of atomic number.

6.3 Single Solute in γ -Fe

In this section, we examined single solute atom substituted in bulk γ -Fe. In the calculations, one Fe atom with spin-up state (i.e. positive magnetic moment) is replaced by the solute atom. Note that the results are independent of the spin state of the replaced Fe atom. The magnetic moments for solute atoms in fcc Fe with AFMD and SQS arrangements are shown in Figure 6.5. The values in the bcc phase are also presented for comparison. Except for Si and Cu, whose magnetic moments are found to be close to zero in both phases, for all the other investigated cases, the magnetic moments in the fcc phase differ from the values in the bcc phase. In general, these elements can be categorized into three groups: the non-magnetic elements, i.e. Ti, V, Nb, and Mo; elements that have the opposite spin state with the Fe atoms in the bcc phase, i.e. Cr, and Mn; and elements that have the same spin state with the Fe atoms in the bcc phase, i.e. Co, and Ni.

It is noticeable that Ti, V, Nb, and Mo atoms have remarkable magnetic moments in the bcc phase, even though these alloying elements are non-magnetic elements. Previous studies have shown that these large magnetic moments are induced by the neighboring iron atoms. By contrast, the magnetic moments for Ti, V, Nb, and Mo in the fcc phase become negligible.

For Cr and Mn, the magnetic moments show opposite behavior in bcc and fcc phase. It is known that these two solutes prefer anti-ferromagnetic coupling. As a result, in ferromagnetic host material, i.e. bcc Fe phase, they are antiferromagnetically coupled to the iron with large intrinsic magnetic moments. While in the fcc phase, since the nearest-neighbor Fe atoms have either spin-up or spin-down states, they maintain the same magnetic arrangement with the replaced Fe atom.

In the case of Co and Ni, the local magnetic moments are positive and are coupled ferromagnetically to the host Fe in the bcc phase. Whereas in the fcc phase, the magnetic moments for Co and Ni are heavily suppressed relative to their pure reference state value ($\mu_{Co}^{ref} = 1.63$ and $\mu_{Ni}^{ref} = 0.59 \mu_B$), which is consistent with previous DFT results, i.e. $0.08 \mu_B$ for Ni [84].

In Figure 6.6, the partial density of states (DOS) of $3d$ -orbital for solutes in the fcc phase with AFMD and SQS configuration are presented. For comparison, the partial DOS for solutes in the bcc phase are also shown. We select Ti, Cr, and Ni because these elements represent three different groups as has been discussed above. For Fe in the bcc phase, Figure 6.6a shows that the spin-up states (also called majority states) are mostly occupied. The spin-down states (also called minority states), on the other hand, are only partially filled. Unequal occupancy of the spin states gives rise to large magnetic moments, which are consistent with previous results [139, 140]. Comparing the projected local DOS of Fe atoms in the fcc phase with the one in the bcc phase, one observes that the peaks of the spin-down states at around $+2$ eV are shifted to $-0.5 \sim 1.0$ eV, and more $3d$ electrons filled the spin-down states in the fcc phase.

With the substitution of Ti, the valance $3d$ electrons are mainly accommodated in the spin-down states in bcc, which contribute to the induced magnetic moments of Ti. By contrast, both spin-up and spin-

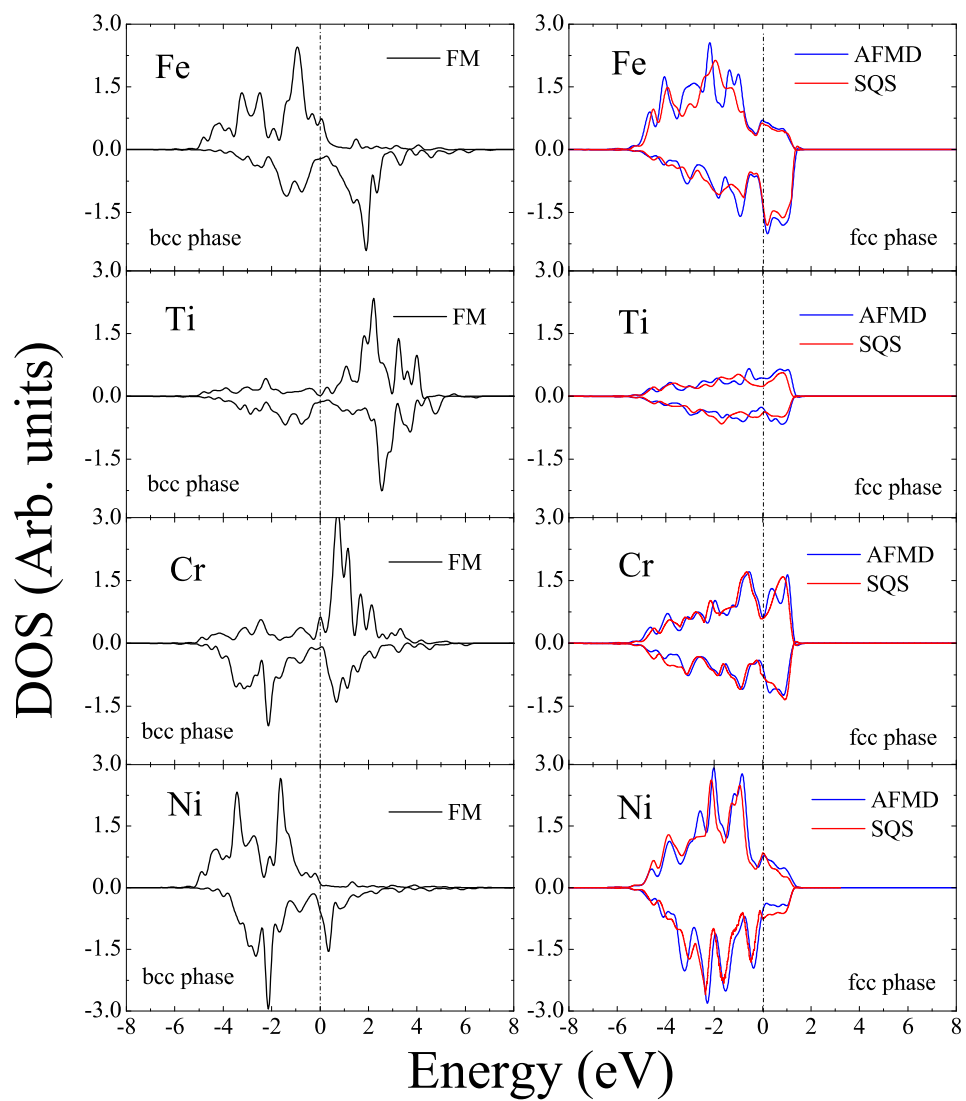


Figure 6.6: Calculated partial density of states (DOS) of 3d-orbital for solutes in the bcc (left) and fcc (right) phases. The Fermi levels (E_F) are set to zero

down states are almost equally occupied by the $3d$ electrons, which gives rise to zero magnetic moment in fcc (see Figure 6.5). Compared with Ti, the spin down states of the Cr $3d$ -orbital are shifted toward lower energy in the bcc phase. Thus, by adding electrons, the unoccupied states move closer to E_F . In addition, the $3d$ electrons mainly occupy the spin-down states, and align their magnetic moments in an opposite sense to the host magnetic moments. This AFM coupling increases the energy of the system when two Cr atoms occupy adjacent sites in the ferromagnetic host material, which leads to the magnetic frustration. In fcc, both spin-up and spin-down states are occupied, and a positive magnetic moment for Cr is obtained (see Figure 6.5).

The results for Ni indicate that the spin-up states are almost completely filled and couple ferromagnetically to the host Fe atoms in bcc. By contrast, in fcc, the occupation of electrons in spin-up and spin-down states are almost equal, resulting in a small magnetic moment.

In Figure 6.5 and Figure 6.6, it is evident that the results obtained by AFMD and SQS magnetic configurations are remarkably close to each other. The largest deviation of the magnetic moments obtained by two different magnetic configurations is less than 16%, suggesting that the AFMD structure is a good representative and can be used to predict solute segregation and diffusion properties in fcc Fe as an alternative to the SQS magnetic structure.

6.4 Solute-solute Interactions in γ -Fe

In this section, we investigated the solute pair interactions in γ -Fe with the AFMD configuration. The solute-solute interactions are calculated according to Equation 4.12. Due to the asymmetric structure of fcc Fe with AFMD magnetic configuration, each site (o) has three types of nearest neighbors, namely p , q , and w , as shown in Figure 6.1. Therefore, three types of solute-solute interactions are calculated at the first nearest neighbor separation. The calculated effective interactions as a function of solute-solute distance are shown in Figure 6.7.

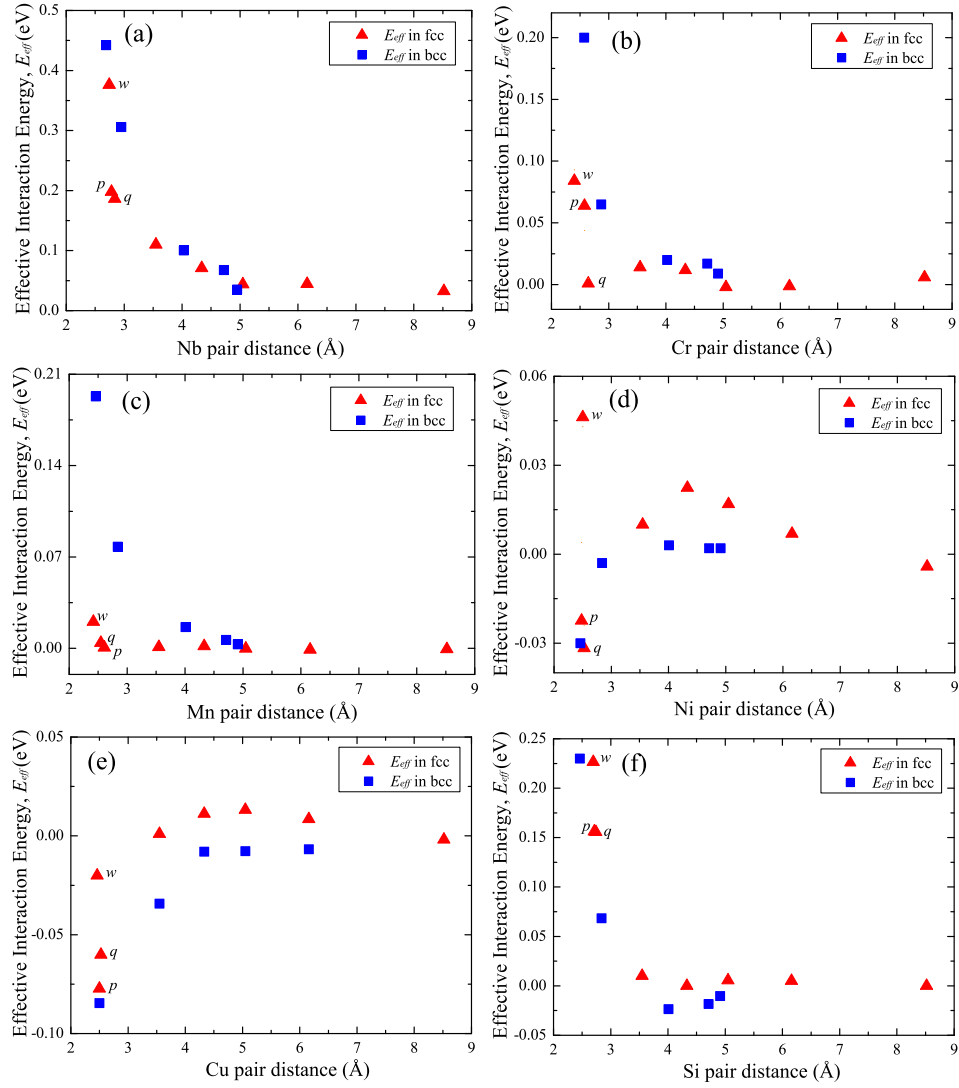


Figure 6.7: Pair interactions for (a) Nb, (b) Cr, (c) Mn, (d) Ni, (e) Cu, and (f) Si in γ - and α -phase Fe matrix.

A strong repulsive interaction between Nb atoms is observed in γ -Fe. The repulsive energy is up to 0.4 eV at the first nearest-neighbor distance, which is comparable with the case in the bcc α -Fe lattice. Such strong repulsive interaction can be ascribed to the elastic strain induced by the large size mismatch. Similar trends are also found for other large solute atoms, i.e. Mo-Mo, and Ti-Ti.

The solute-solute interactions between Cr (Mn) atoms are repulsive. However, compared with the case of Nb, the values are much smaller. In Figure 6.7b, the repulsive interaction between Cr atoms is less than 0.1 eV at first nearest neighbor separation. For Mn atoms, the repulsive energy for the Mn-Mn pair is found to be negligible in fcc γ -Fe, in contrast to the modest repulsive interaction in bcc α -Fe. This is because the strong repulsive interaction is caused by the magnetic frustration in ferromagnetic bcc Fe. When the magnetic arrangements have been changed, i.e. AFMD in fcc Fe, the influence of the magnetism on the solute pair interactions becomes smaller. Consequently, weak repulsive interactions are observed for Cr (Mn). In addition, we also analyse the structure distortion induced by the substitutional Cr (Mn) atom in fcc γ -Fe. The results indicate that bond lengths from single Cr (Mn) solute to its nearest-neighbor shell, i.e. d_{Cr-Fe} (d_{Mn-Fe}) differs from pure Fe, i.e. d_{Fe-Fe} by at most 0.015 (0.01) Å. This less than 1% effect exists only for the first nearest neighbor shell and decays rapidly with distance. So one would expect rather small effective interactions from elastic aspects.

Figure 6.7d shows that the Ni-Ni interaction depends on the occupation sites. Specifically, when two Fe atoms with different spin states are replaced by the Ni atoms, the Ni pair interaction behaves repulsive, otherwise, it shows attraction. This is because Ni prefers ferromagnetic coupling. This ferromagnetic coupling increases the energy of the system when two Ni solutes occupy adjacent sites with opposite spin states. Recall that the magnetic moments for Ni are small (see Figure 6.5). As a result, the effects of magnetism to the repulsive interactions are much smaller as compared with the effects for Cr (Mn, V) in the bcc lattice.

Cu shows an attractive interaction in the fcc lattice (see Figure 6.7e),

indicating possible clustering similar to that predicted in the bcc lattice. As discussed in Chapter 5, such attractive Cu-Cu interaction can be viewed as a magnetically driven clustering. The Si-Si interactions as a function of Si pair distance is shown in Figure 6.7f. It is clear that a short-range repulsive interaction occurs between Si atoms. The origin of this repulsion is based on the fact that Si atoms prefer to bond with Fe atoms instead with other Si atoms.

6.5 Solute Segregation in $\Sigma 5$ Grain Boundaries in fcc γ -Fe

In this section, we describe the simulation results for the solute segregation behavior in the $\Sigma 5$ tilt grain boundary in fcc γ -Fe. The binding energies of solutes with the grain boundaries are calculated according to Equation 4.10. In the calculations, one Fe atom with spin-up state is replaced by the solute. Note that the results are independent of the spin states of the replaced Fe atom. In Figure 6.8, the calculated binding energies for different solutes at various grain boundary positions are presented. The results indicate that similar to the cases in the bcc phase, the influence of the grain boundary on the binding energies of solutes are short ranged and limited to about 2~3 atomic layers in the fcc phase. In addition, different solutes prefer different positions at the grain boundary. For example, the binding energy for Nb and Mo atoms have the largest segregation energies in position *a*, whereas other elements such as Si, Cr, and Mn prefer position *b*.

Despite of these similarities, we found positive binding energies for some relatively small solute atoms, such as Cr and Si in fcc phase grain boundaries. In addition, no segregation tendency is found for Ni. By contrast, for big solute atoms, such as Nb and Mo, large segregation energies are obtained.

According to Langmuir-McLean equation, we calculate the effective binding energies, E_{seg}^{eff} (see Chapter 5 for details). Note that in some cases, e.g. Cr and Si, only a few boundary sites may be available for grain boundary

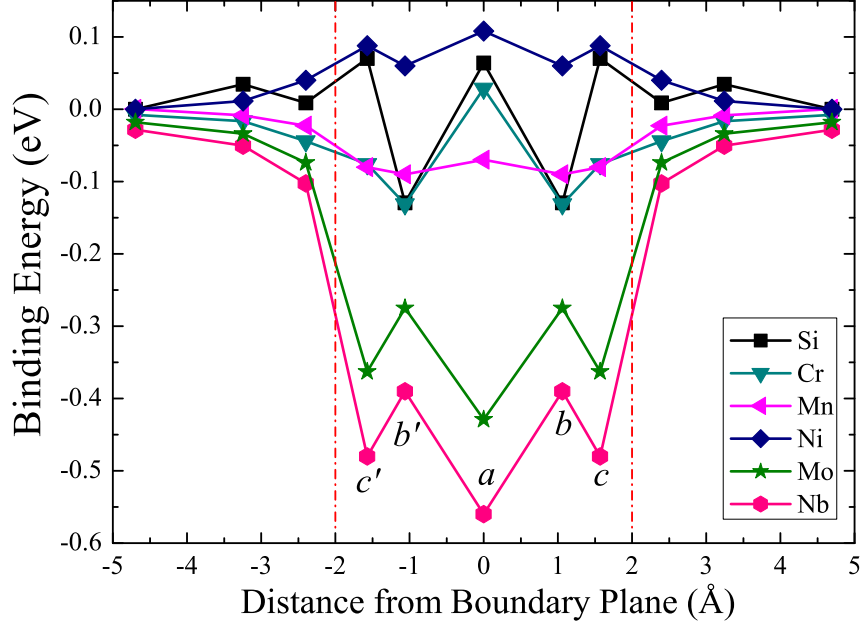


Figure 6.8: Binding energies for substitutional solutes at the $\Sigma 5$ fcc grain boundary as a function of distance from the boundary plane; a , b , c , b' , and c' refer to the boundary sites as labeled in Figure 6.3.

segregation. As a results, Equation 5.1 should be modified as:

$$\frac{c_{gb}^i}{c_{gb}^0 - c_{gb}^i} = \frac{c_{bulk}}{(1 - c_{bulk})} \exp\left(-\frac{E_{seg}^i}{k_B T}\right) \quad (6.1)$$

where c_{gb}^0 is the fraction of boundary sites with favourable binding. For example, $c_{gb}^0=0.8$ for Cr, whereas $c_{gb}^0=0.4$ for Si (see Figure 6.8). The effective segregation energies of selected solutes in $\Sigma 5$ grain boundary in bcc and fcc Fe are listed in Table 6.2.

It can be seen that for large solutes, i.e. Nb and Mo, the interactions between these solute atoms and the grain boundary in fcc are even stronger than that in the bcc phase, which demonstrated that segregation of these solute atoms to the grain boundary in fcc are more favorable. For example, the binding energies of Nb at boundary site a in fcc increase by 15% (see

Table 6.2: Effective binding energies (E_{seg}^{eff}) for selected solutes in $\Sigma 5$ bcc and fcc grain boundary. Unit is eV.

	Si	Cr	Mn	Ni	Mo	Nb
bcc	-0.09	-0.12	-0.14	-0.19	-0.31	-0.40
fcc	-0.10	-0.10	-0.08	–	-0.35	-0.47

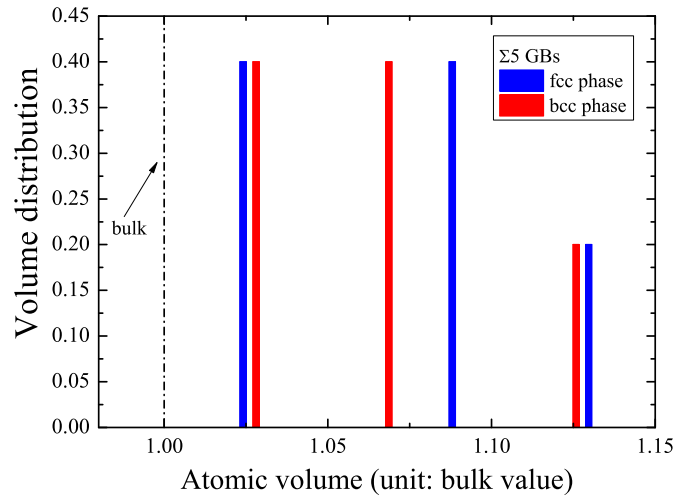


Figure 6.9: Volume distribution per periodic unit cell for $\Sigma 5$ grain boundaries in bcc and fcc Fe.

Figure 5.1 and Figure 6.8). This can be understood based on the fact that fcc Fe is the closest-packed structure. Evidently, the elastic strain induced by these big solutes in fcc bulk are larger than that in bcc bulk. Therefore, when the grain boundary is present where the packing density is significantly reduced, substantial strains can be partially relieved, which give rise to larger segregation energies.

We also plot the site volumes for bcc and fcc grain boundaries. The results are shown in Figure 6.9. The site volumes are given in units of the atomic volume in the bulk, which is an important parameter to predict the segregation tendency of large solutes at grain boundaries as discussed in

Chapter 5. It is clear that the site volumes in the fcc grain boundary have larger values when compared with the bcc grain boundary. Especially at site *c*, it shows the biggest increase in size when comparing fcc and bcc and the binding energies increase accordingly by 20% (see Figure 5.1 and Figure 6.8). As a result, remarkable attractive interactions between large solutes and the fcc $\Sigma 5$ grain boundary are achieved

For Ni, it prefers to stay at the bulk position rather than at the boundary sites. A possible explanation is that Ni prefers to bind with the host atoms, and consequently, it is unfavorable for Ni to be placed at the boundary site, since this will result in longer distance between nearest neighbors due to the excess volume. This finding is consistent with Enomoto *et al.*'s report that no appreciable segregation of Ni to fcc boundaries is observed [141]. The experimental binding energy of Mn to austenite grain boundaries is -9 ± 3 kJ/mol [141], which is also comparable with our predictions of -7.7 kJ/mol for the fcc $\Sigma 5$ grain boundary.

Chapter 7

Interaction of Solutes with α - γ Iron Interface

7.1 Structure of Ferrite-Austenite (bcc-fcc) Interface

The structure and orientation of austenite-ferrite interfaces has been studied extensively by experiments because of its significance in controlling the microstructure of steels [142]. The most frequently detected orientation relationships for fcc and bcc lattices are those derived by Kurdjumov and Sachs (K-S) in 1930 and by Nishiyama and Wassermann (N-W) in 1935 [143, 144]. The orientations can be described by a set of planes that are parallel in the lattices, i.e.:

N-W orientations: $(111)_\gamma \parallel (110)_\alpha$ and $[1\bar{1}0]_\gamma \parallel [001]_\alpha$

K-S orientations: $(111)_\gamma \parallel (101)_\alpha$ and $[10\bar{1}]_\gamma \parallel [11\bar{1}]_\alpha$

Both models assume unanimously that a close packed $\{110\}$ plane of the bcc lattice is arranged parallel to a closed packed $\{111\}$ of the fcc lattice. However, the alignment of the planes to each other is different. It seems that these two relationships are quite different from each other, however, in fact, they are only 5.26° apart. In this work, we describe the bcc-fcc interface using a selected K-S orientation relationship.

Note that the domain of DFT calculations is relatively small. To minimize the lattice mismatch and construct a coherent interface, we carefully studied the interface structure and select the $(1\bar{2}1)$ plane as the habit plane. This habit plane is also observed in a number of experimental studies [145, 146]. Accordingly, the three orthogonal directions for the fcc grain, x , y , and z , are chosen along the $[10\bar{1}]$, $[111]$, and $[1\bar{2}1]$ crystal directions, respectively. The z -direction is perpendicular to the interphase boundary, i.e. $(1\bar{2}1)$ is the habit plane. At the atomic level, the $(1\bar{2}1)$ habit plane is not flat, but consists of structural ledges composed of $(1\bar{1}1)$ and $(0\bar{2}0)$ facets [147].

The periodicity in the x - and y -directions for the bcc crystal is chosen close to those of the fcc crystals to ensure coherency. Thereby, x and y are chosen along $[11\bar{1}]$ and $[1\bar{5}4]$ crystal directions, respectively. The orientation of the bcc grain perpendicular to the interface, i.e. along z -direction, is $[3\bar{1}2]$. In order to maintain periodic boundary conditions, two interphase boundaries were included in the simulation block. The structure of the fcc-bcc Fe interface with AFMD and SQS magnetic configurations are shown in Figure 7.1.

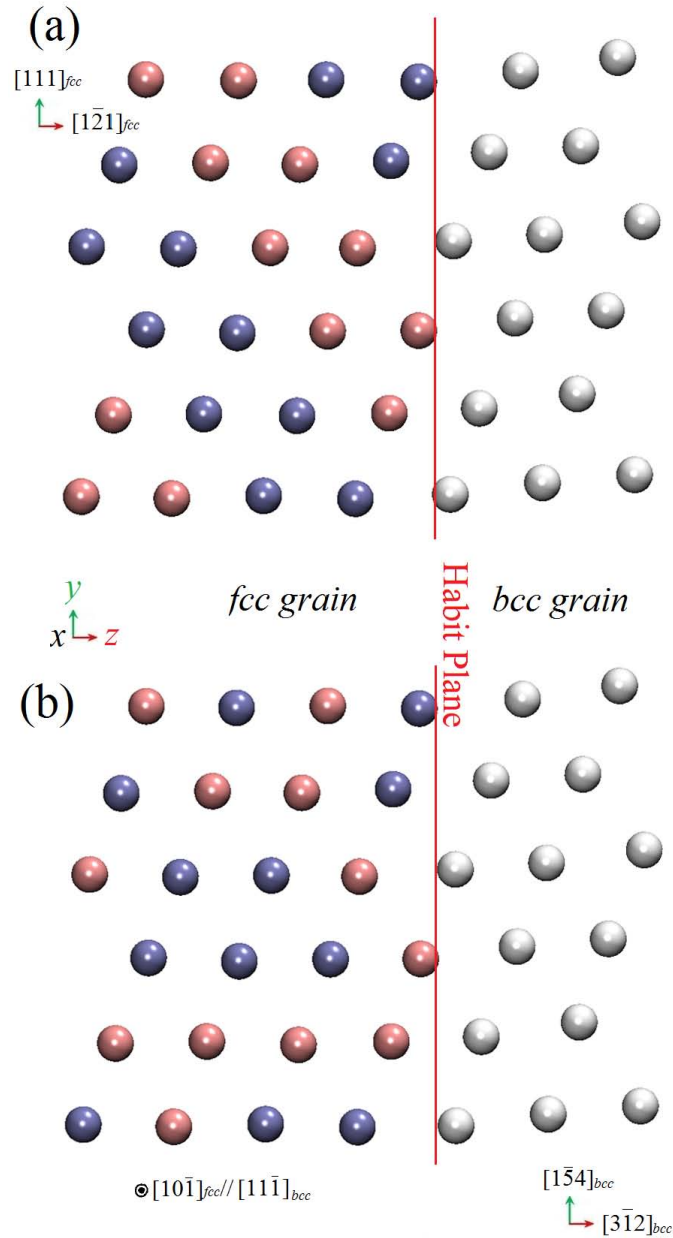


Figure 7.1: Structure of bcc-fcc interface with K-S orientation relationship. (a) AFMD and (b) SQS configuration for fcc. The white circles represent atoms in the bcc Fe grain, and the red (blue) circles indicate atoms in the fcc Fe grain with spin up (down) states.

7.2 Interface Energy

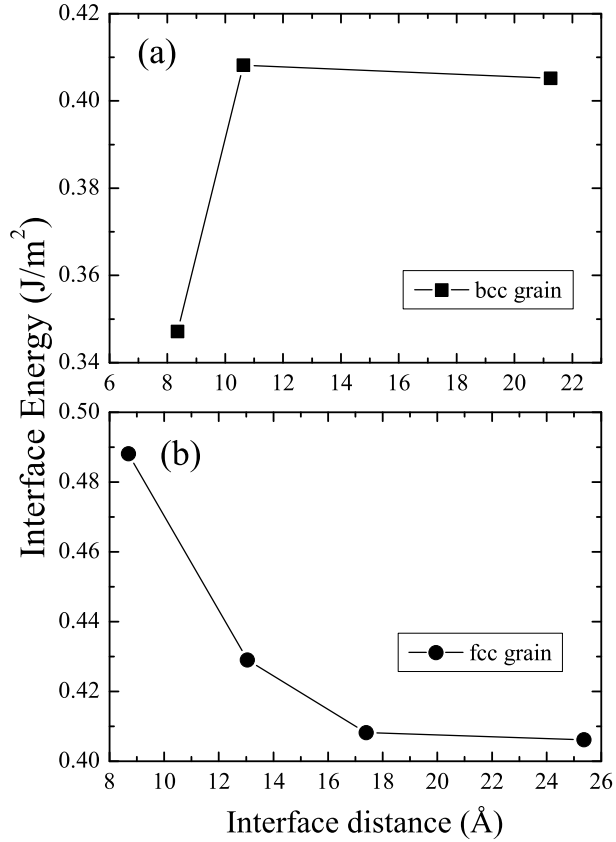


Figure 7.2: bcc-fcc interface energy as a function of (a) the bcc grain size while the length of the fcc grain is fixed to 25.4 Å; and (b) the fcc grain size while the length of the bcc grain is fixed to 21.3 Å.

The supercell size was determined from calculation of the interface energy as a function of interface distance (see Chapter 4). The results are shown in Figure 7.2. Note the fcc grain is described by the AFMD magnetic configuration.

Since the interface structure is asymmetric, we check the fcc and bcc grain size separately. Figure 7.2a shows the interface energy as a function of the thickness of the bcc grain. In order to minimize the influence of the

fcc grain, we fix the length of the fcc grain to 25.4 Å. The results show that the interface energy is converged when the bcc grain thickness is 10.6 Å and larger. We then fix the length of the bcc grain to 21.3 Å and systematically increase the thickness of the fcc grain. Figure 7.2b shows that the interface energy is converged when the fcc grain is 17.4 Å and larger. The $\alpha - \gamma$ interface energy ($\sigma_{\alpha-\gamma}$) is determined to be 0.41 J/m² (see Table 7.1).

In this work, we also calculated the surface energies for different equilibrium bcc and fcc surfaces. This is because the surface energies can be more accurately measured than interface energies, which provide a good benchmark for our simulations. In Table 7.1, the surface energies for bcc (3 $\bar{1}2$) and fcc (1 $\bar{2}1$) are only slightly (around 5%) larger when compared to their closest-packed surface, i.e. bcc (110) and fcc (111) surface. In addition, our calculations agree well with the experimental measurements [148, 148]. These results suggest that our calculations are reasonable and reliable.

Table 7.1: Surface and interface energies for the equilibrium bcc and fcc surfaces, and bcc-fcc interface, in units of J/m².*

	Present	Previous theoretical work	Exp.
Fe(110) _{bcc}	2.44	2.43 [149]	2.41 [148]
Fe(3 $\bar{1}2$) _{bcc}	2.59		
Fe(111) _{fcc}	2.21	2.18 [150]	2.11 [151]
Fe(1 $\bar{2}1$) _{fcc}	2.30		
Interface	0.41		~0.5 [152]

* The magnetic structure of the fcc Fe is described using AFMD configuration.

It is known that fcc Fe exists in paramagnetic state. In order to check the influence of magnetic structure on the interface energy, the SQS magnetic configurations are employed to describe the fcc phase. The calculated $\alpha - \gamma$ interface energy is 0.45 J/m². The results indicate that the interface energies

obtained by these two different magnetic structures (i.e. AFMD and SQS) are close to each other, and they are comparable with the experimental estimates [152].

7.3 Magnetic and Electronic Properties for bcc-fcc Interface

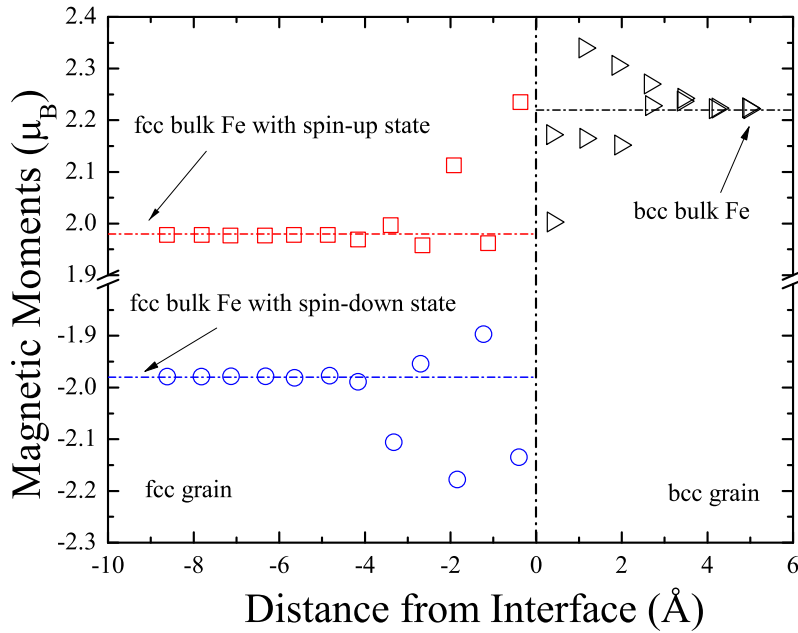


Figure 7.3: Magnetic moments of Fe atoms across the bcc-fcc interface.

We now turn to the analysis of the magnetic profile around the fcc-bcc interface. Figure 7.3 shows the local magnetic moments of the Fe atoms as a function of their positions in the bcc-fcc interface. The results indicate that the oscillations of magnetic moments occur in the vicinity of the fcc-bcc interface. In addition, the magnetic moments of the Fe atoms in both phases are enhanced at the interface, and the highest magnetic moment is $2.35 \mu_B$ in the bcc phase. At a distance of 3.0 \AA away from the interface, the local magnetic moment converges to the bulk value in both phases, suggesting

the influence of the interface on the magnetic moments is short-ranged.

Similar fluctuations in the local magnetic moments are observed not only in the bcc-fcc Fe interface, but also in Fe grain boundaries [28, 153], Fe surfaces [154], and Fe nanowires [155]. The origin of the high magnetic moments of the Fe interface atoms has been discussed earlier [25, 156, 157]. Čák *et al.* attributed such high magnetic moment at the boundary or surface to the magnetovolume effect, i.e. magnetic transition leads to volume change [153].

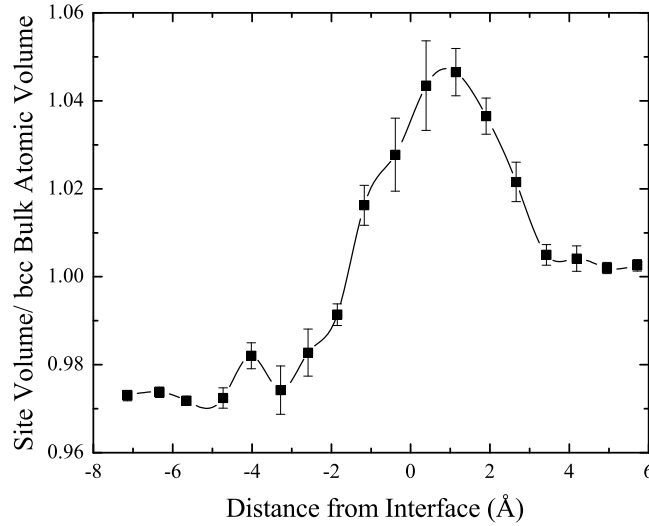


Figure 7.4: Averaged site volume distribution across the bcc-fcc interface. The bars indicate the range of values of site volumes for Fe atoms with spin-up or spin-down states.

In Figure 7.4, the local atomic volume for each Fe atom is calculated by constructing a Voronoi polyhedron around each site. The calculated atomic volume is 11.4 \AA^3 and 11.1 \AA^3 for bcc and fcc phases, respectively. While at the interface, the atomic volume is increased up to 12.0 \AA^3 . In general, the high local magnetic moments are associated with increased Voronoi volumes, which is similar to what has been reported for Fe bcc tilt grain boundaries [28, 153]. In addition, from Figure 7.4, it is evident that the thickness of the pure bcc-fcc interface is about 7.0 \AA .

7.4 Binding Energies of Solutes with bcc-fcc Interface

In this section, the segregation behavior of different solutes at various interface positions is investigated. The relative energy of solutes with the bcc-fcc interfaces is calculated as:

$$E_{rel}^i = (E_{I+X}^i + E_I) - (E_{\alpha+X} + E_{\alpha}) \quad (7.1)$$

where E_{I+X}^i and E_I are the total energies of bcc-fcc interface with and without solute. $E_{\alpha+X}$ and E_{α} are the total energies of bcc bulk with and without solute. The superscript i denotes the substitutional sites in the interface. A negative value for E_{rel}^i indicates an attractive interaction between solute and the considered interface site.

Since Nb has the largest segregation energy among our investigated cases, while Mn is one of the most common alloying elements in steels, we first select these two elements for detailed analysis. The calculated relative energies for Nb and Mn across the bcc-fcc interface are shown in Figure 7.5. Both AFMD and SQS magnetic configurations are employed to describe the magnetic states of the fcc grain.

Despite some deviations, the segregation behavior obtained by the SQS magnetic configuration is comparable with the AFMD results. For Nb, strong interactions between Nb and the bcc-fcc interface are obtained. Based on the SQS magnetic configuration, the energy difference between austenite and ferrite for Nb is 0.18 eV, which is close to the AFMD results, i.e. 0.21 eV. In addition, the energy difference between Nb in the interface and in ferrite is 0.18 eV, which differs from the AFMD result by 0.01 eV. For Mn, both SQS and AFMD results indicate that there exist large chemical potential differences between ferrite and austenite. The energy difference between Mn in the interface and in austenite is 0.10 eV, which is the same with the value obtained by using the AFMD arrangement. Therefore, one can conclude that AFMD and SQS magnetic configurations for fcc-Fe lead to very similar characteristics of solute segregation in the bcc-fcc interface. Thus, in the following calculations, we focus on the computationally less costly AFMD

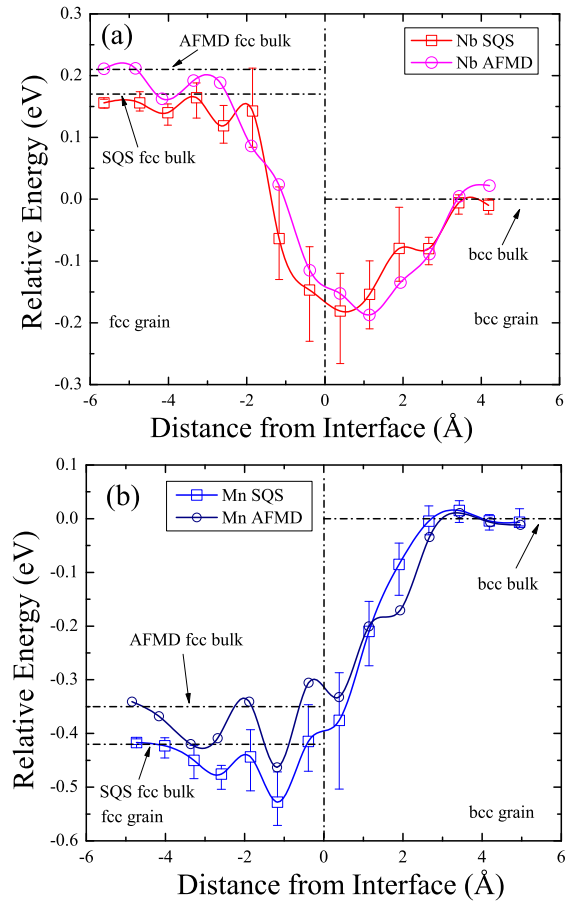


Figure 7.5: Relative energies for (a) Nb, and (b) Mn across the α - γ interface as a function of distance from the habit plane. The bars indicate the range of energies for the SQS simulations, where the replaced Fe atom has spin-up or spin-down states.

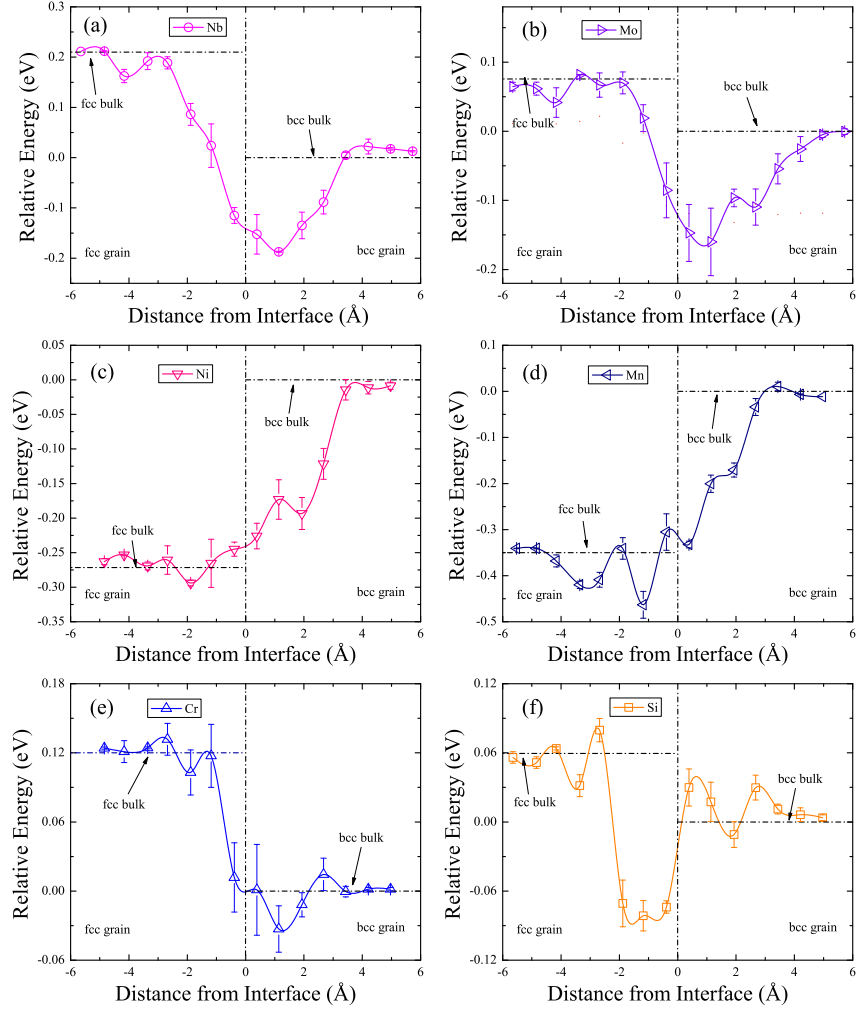


Figure 7.6: Relative energies for substitutional solutes across the bcc-fcc interface as a function of distance from the habit plane. The bars indicate the range of energy values, where the replaced Fe atom has spin-up or spin-down states. The fcc grain is described by the AFMD configuration.

magnetic configurations.

In Figure 7.6, the relative energies for Nb, Mo, Ni, Mn, Cr, and Si across the bcc-fcc interface are shown. These alloying elements are crucial for steels by controlling the austenite to ferrite transformation. We find that

different solutes prefer different phases. Mn and Ni are austenite stabilizer and prefer the γ -phase, whereas Nb, Mo, Cr, and Si are ferrite stabilizer and prefer the α -phase. As a result, a chemical potential difference exists for the substitutional elements between ferrite and austenite. Figure 7.6 shows that the energy difference between ferrite and austenite for Mo and Si are small, i.e. less than 0.06 eV. This difference becomes much larger for Mn and Ni, i.e. up to 0.35 eV. Consequently there is a considerable driving force for Mn and Ni transfer from ferrite to austenite, which is expected to result in a ‘spike’ in austenite [158]. These predictions are consistent with the role of these alloying elements in stabilizing austenite and ferrite, respectively. For example, Ni is a critical alloying element for austenitic stainless steels and Cr for ferritic stainless steels.

As shown in Figure 7.6, a deep valley is found for Nb, Mo, and Si, indicating strong binding of these elements with the bcc-fcc interface. On the other hand, there is a gradual change between ferrite and austenite for Ni, Mn, and Cr, and no obvious binding is observed. To give a more realistic representation of the binding energy, we use the average values between the bulk values as the reference point [158, 159].

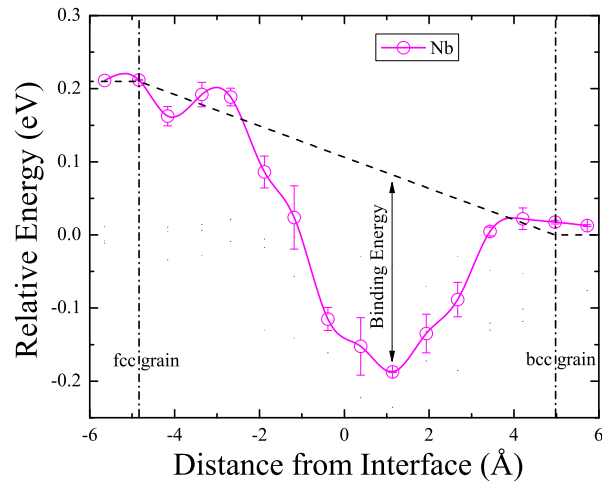


Figure 7.7: Definition of the binding energy using linear interpolation from the bulk energies.

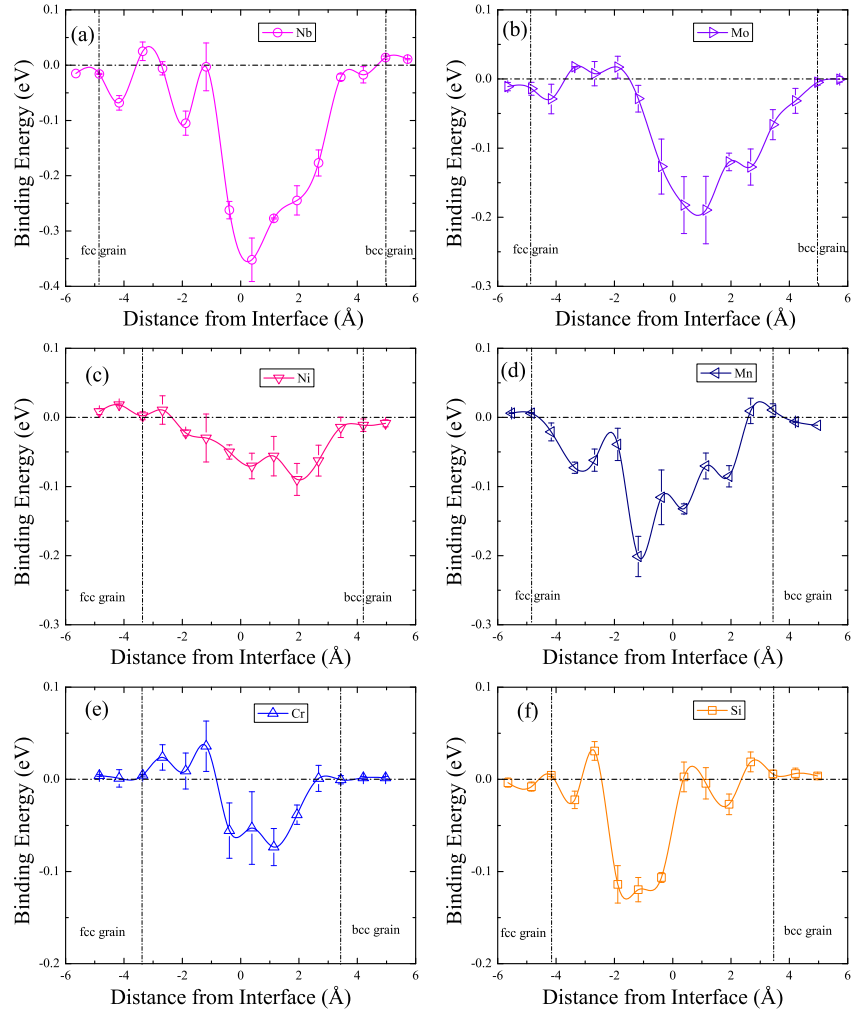


Figure 7.8: Binding energies for substitutional solutes at the bcc-fcc interface as a function of distance from the habit plane. The bars indicate the actual values of binding energies. The fcc grain is described by the AFMD configuration. The interface width is indicated by two dashed lines.

For each interface position, we calculate the average energy using linear interpolation between the two bulk values. Then the binding energy for each position is defined as the difference between the DFT results (as shown in Figure 7.6) and the interpolation from the bulk energies. Figure 7.7 shows an example of this analysis for Nb. Note that the widths of the bcc-fcc interface depend on the substituted solute atoms, which vary from 7.0 Å to about 9.0 Å, and show certain asymmetric behaviour. In this work, the boundaries of the interface are defined as the positions where the variation of the relative energies due to magnetism (i.e. spin-up and spin-down) is less than 0.01 eV (see the bars in Figure 7.6). Using this procedure, we calculate the binding energies of selected solutes across the bcc-fcc interface. The results are shown in Figure 7.8.

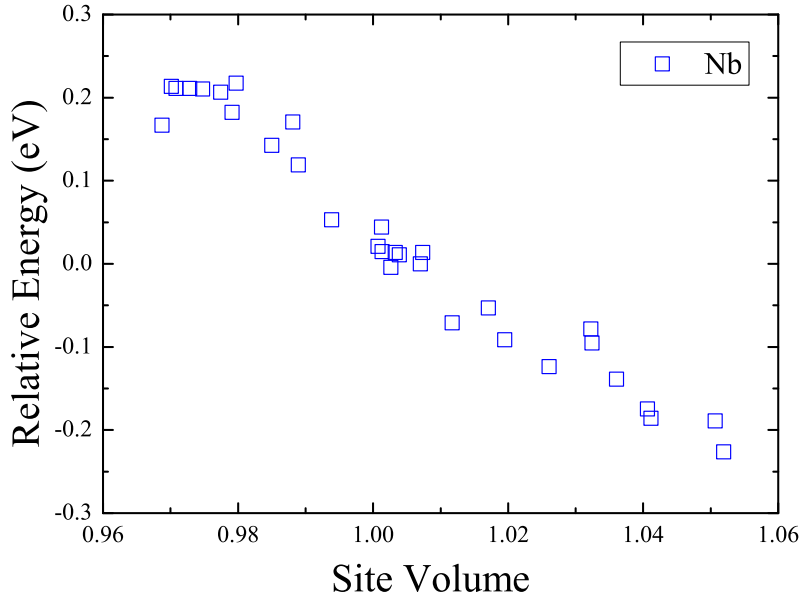


Figure 7.9: Relative binding energies of Nb at the bcc-fcc interface as a function of the site volume.

Significant binding energies are found for large, elastically dominated solutes (Nb, Mo). The maximum energy difference between the interface and the reference point for Nb (Mo) is 0.39 eV (0.24 eV). Such strong

binding energies indicate that bcc-fcc interface positions are favorable for large solute elements segregation. In particular, we find the larger binding energy of Nb (Mo) corresponds to the larger excess volume of the interface sites. Figure 7.9 plots the relative energies of Nb as a function of the site volume. It is evident that there is a distinct correlation between E_{rel}^i and the site volume, i.e. E_{rel}^i increasing with the site volume. This trend can be understood in terms of a strain-relief argument, whereby the elastic strain induced by the large substitutional solutes (e.g. Nb, Mo, etc.) in the bulk lattice can be partially relieved at the interface due to the excess volume.

In the case of Ni, however, the interaction between Ni and bcc-fcc interface is found to be rather weak, which is consistent with previous experimental observations [141, 158]. Recall that there is no segregation trend for Ni in the fcc $\Sigma 5$ grain boundary (see Chapter 6). A possible explanation is that Ni prefers to bind with Fe atoms. From ferrite to austenite, the coordination number is increased from 8 to 12, resulting in lower values for Ni in austenite than in ferrite and at the interface positions. For Mn, the energy difference between the interface and the reference point is -0.20 eV, which is comparable with the values at the $\Sigma 5$ bcc and fcc grain boundaries. For Cr, relatively small binding energies are observed, whereas moderate binding energies are found for Si.

In Figure 7.8, the bars indicate the actual values of binding energies, where the replaced Fe atom has spin-up or spin-down states. It is evident that the spin states play an important role in binding energies. This is because the distance between two Fe atoms with the same spin states is larger than those with opposite spin states (see Chapter 6, Figure 6.1), which give rise to larger excess volume. For large solutes, e.g. Nb and Mo, the larger excess volume favors the solute-interface binding. For magnetic elements, i.e. Ni, Mn, and Cr, the binding energies are influenced by the magnetic interactions between solute and the host atoms. As discussed in Chapters 5 and 6, the Cr-Fe (Mn-Fe) and Ni-Fe interactions are anti-ferromagnetic and ferromagnetic, respectively. At the interface, there exist different magnetic arrangements, which contribute to the variation of the binding energies. For Si, however, the influence of the spin states on the

binding energies is small.

In a similar manner with the grain boundary, we calculate the effective binding energies of solutes in the bcc-fcc interface. Based on the Coghlan-White approach, the segregation to different sites i in the bcc-fcc interface, each with the binding energy E_{seg}^i , is given by [117, 118]:

$$\frac{c_{int}^i}{1 - c_{int}^i} = \frac{c_{bulk}}{(1 - c_{bulk})} \exp\left(-\frac{E_{seg}^i}{k_B T}\right) \quad (7.2)$$

where c_{bulk} is the solute concentration in the bulk, and c_{int}^i is the solute concentration at the interface site i . Equation 7.2 can be rewritten as:

$$c_{int}^i = \frac{c_{bulk} \exp\left(-\frac{E_{seg}^i}{k_B T}\right)}{1 - c_{bulk} + c_{bulk} \exp\left(-\frac{E_{seg}^i}{k_B T}\right)} \quad (7.3)$$

c_{int}^i is calculated for each interface site. Then the total segregation c_{int} is a weighted average summed over all interface sites, which is given by:

$$c_{int} = \sum_i (F_i c_{int}^i) \quad (7.4)$$

where F_i is the fraction of the interface sites that have binding E_{seg}^i . In Figure 7.10, the calculated total segregation for Nb in Fe bcc-fcc interface are plotted. We fit these data according to the Langmuir-McLean equation and obtain the effective binding energies (E_{seg}^{eff}). Here three fitting equations are employed in this work, i.e.:

$$\text{Fitting 1: } \frac{c_{int}}{c_{int}^0 - c_{int}} = \frac{c_{bulk}}{(1 - c_{bulk})} \exp\left(-\frac{E_{seg}^{eff}}{k_B T}\right) \quad (7.5a)$$

$$\text{Fitting 2: } \frac{c_{int}}{1 - c_{int}} = \frac{c_{bulk}}{(1 - c_{bulk})} \exp\left(-\frac{E_{seg}^{eff}}{k_B T}\right) \quad (7.5b)$$

$$\text{Fitting 3: } c_{int} = c_{bulk} \exp\left(-\frac{E_{seg}^{eff}}{k_B T}\right) \quad (7.5c)$$

In Equation 7.5a, c_{int}^0 is the fraction of interface sites with favourable

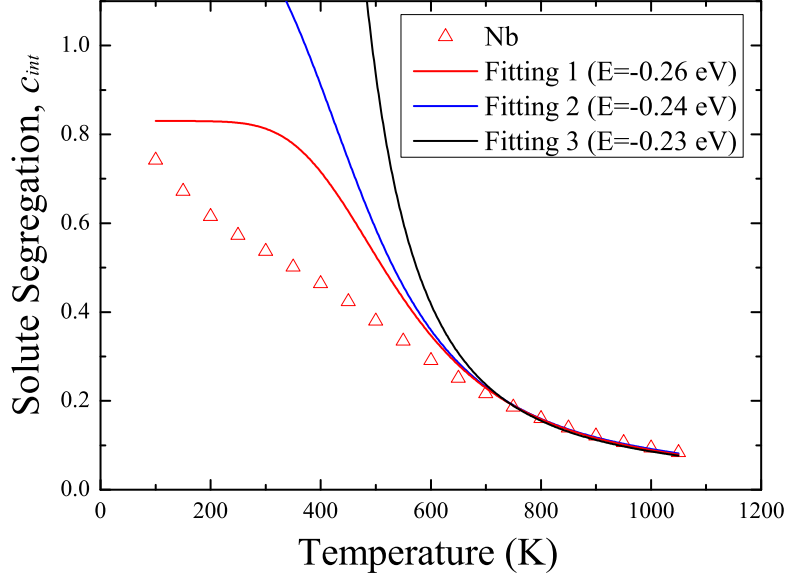


Figure 7.10: Calculated effective binding energies for selected alloying elements as a function of solute volume in bcc-fcc interface. The dotted line indicates the volume of Fe calculated from the first nearest neighbor distance in the bcc bulk Fe.

binding. For example, 20 of 24 interface sites have the favourite binding for Nb, i.e. $c_{int}^0=0.83$. Though Equation 7.5a is the most rigid expression, it can not be used in the experiments. This is because it is extremely difficult to obtain c_{int}^0 based on the experimental measurements. Note that the data cannot be fitted perfectly across the whole temperature region using one binding energy since there are unlike for the $\Sigma 5$ boundaries rather large fluctuations in the individual binding energies for different interface sites. Since we are interested in $\alpha-\gamma$ transformation temperature, i.e. 773~1184K, we focus on this high temperature range. The results based on the different fitting equations are essential the same at high temperature. To make our results, i.e. E_{seg}^{eff} , more comparable with those measurements, Equation 7.5b is employed in the following study.

The effective binding energies by fitting Equation 7.5b of selected solutes are summarized in Figure 7.11. The results are plotted as a function of

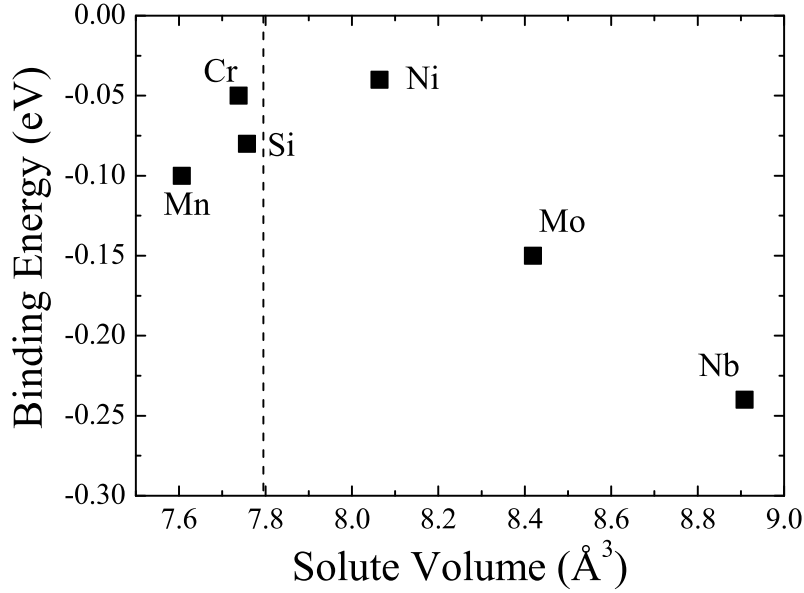


Figure 7.11: Calculated effective binding energies for selected alloying elements as a function of solute volume in bcc-fcc interface. The dotted line indicates the volume of Fe calculated from the first nearest neighbor distance in the bcc bulk Fe.

solute volume (V_s), which was computed from relaxed atomic positions in the bcc bulk according to the hard sphere model. Similar with the case of bcc $\Sigma 5$ grain boundary, there is a distinct correlation between the effective binding energy and solute volume, i.e. the magnitude of E_{seg}^{eff} and thus the tendency for segregation increase with solute size. Compared with the values in bcc and fcc grain boundaries, the binding energies of large solute, i.e. Nb and Mo, are smaller in the bcc-fcc interface. This can be ascribed to the smaller excess volume in the bcc-fcc interface than in the $\Sigma 5$ bcc or fcc grain boundaries (see Figure 6.9 and Figure 7.4). On the other hand, the binding energies of relatively small alloying elements, e.g. Si and Mn, are comparable with the values in bcc and fcc grain boundaries.

The experimental results for interaction parameters between Fe and solutes in the interface are limited. Nevertheless, Zurob *et al.* estimated the binding energies for several alloying elements with the phase boundary using

controlled decarburization experiments. The experimental binding energies for Cr and Mo are $-3\sim-6$ kJ/mol ($-0.03\sim-0.06$ eV) and $-15\sim-24$ kJ/mol ($-0.16\sim-0.25$ eV) [152, 158, 160], which are comparable with our predictions, i.e. -5.8 kJ/mol (-0.06 eV) and -15.4 kJ/mol (-0.16 eV), respectively. In addition, our calculations indicate that the binding energies of Nb and Mo with the interface are relatively large. Overall, such large binding energies indicate strong interactions with the interface, and are expected to delay ausenite-to-ferrite transformation, which is consistent with experimental observations [158, 161, 162].

In general, the solute segregation behavior is illustrated in Figure 7.12. For large solute elements, e.g. Fe-Nb and Fe-Mo systems, the interactions are rather strong, which can be rationalized with the elastic strains, where these large solute elements bind to the interface as a means of relieving strain on the Fe matrix. For Fe-Mn and Fe-Ni systems, the energy difference between ferrite and austenite is comparatively large, which provides considerable driving force for solute transfer from ferrite to austenite. The interaction between Ni and the interface is weak, while it becomes much larger for Mn. For ferrite stabilizers with similar atom size than Fe, relative small (Cr) to moderate (Si) binding energies are predicted.

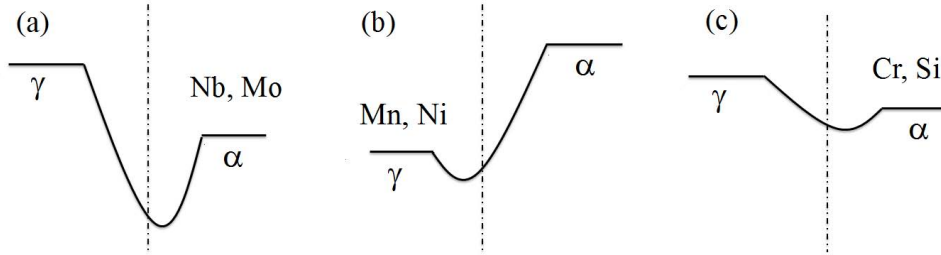


Figure 7.12: Illustrations of interaction profiles between solute atoms and bcc-fcc interface.

7.5 Solute-solute Interactions in bcc-fcc Interface

In order to analyze the segregation characteristics of solutes in more detail, we calculate the effective interaction (E_{eff}) as a function of solute-

solute distance according to Equation 4.12. To minimize the number of calculations, we fix one solute atom in its favorite position based on the single solute segregation profile while the other solute atom occupies other interface positions.

The results for Nb-Nb, Cr-Cr, and Mn-Mn are shown in Figure 7.13. We select these solutes because they are some of the most common alloying elements in steels. In addition, these examples represent two major solute-specific contributions to the effective interactions: contributions from the elastic energy induced by atomic size misfit, and contributions from competing magnetic interactions.

The elastic contribution to the solute-solute interaction is determined by the relative size of solutes with respect to Fe. As the size of solutes increases, the elastic contribution to solute-solute interactions becomes increasingly more important. In Figure 7.13a, the repulsive energy for Nb-Nb pair is up to 0.4 eV within the first nearest neighbor distance, which is comparable with the values of bcc and fcc Fe bulk. In addition, we find apparent negative binding energies (about -0.1 eV) at intermediate pair distance. Such attractive interactions occur when two Nb atoms belong to different grains. Similar with the case of $\Sigma 5$ tilt grain boundaries, the attractive interaction can be ascribed to the excess volume at the interface (see Figure 7.4), whereby the elastic strain at these positions can be partially relieved.

In chapter 5, we have discussed that strong repulsive interactions between Cr atoms can be attributed to magnetic frustration. According to the model of Moriya [129], the Cr-Fe and Cr-Cr interactions are antiferromagnetic (AFM). In the dilute limit, this AFM coupling increases the energy of the system when two Cr atoms occupy adjacent sites in an otherwise ferromagnetic (FM) host material. Figure 7.13b shows that in the bcc-fcc interface, when two Cr atoms occupy adjacent sites in the bcc phase, strong repulsive energy is obtained. By contrast, when the second Cr atom occupies the fcc grain position and has the opposite spin states than the first Cr atom, the repulsive interactions for Cr solute pair becomes weaker, i.e. less than 0.1 eV within the first nearest neighbor distance.

Similar results are also found for Mn-Mn interactions. In Figure 7.13c,

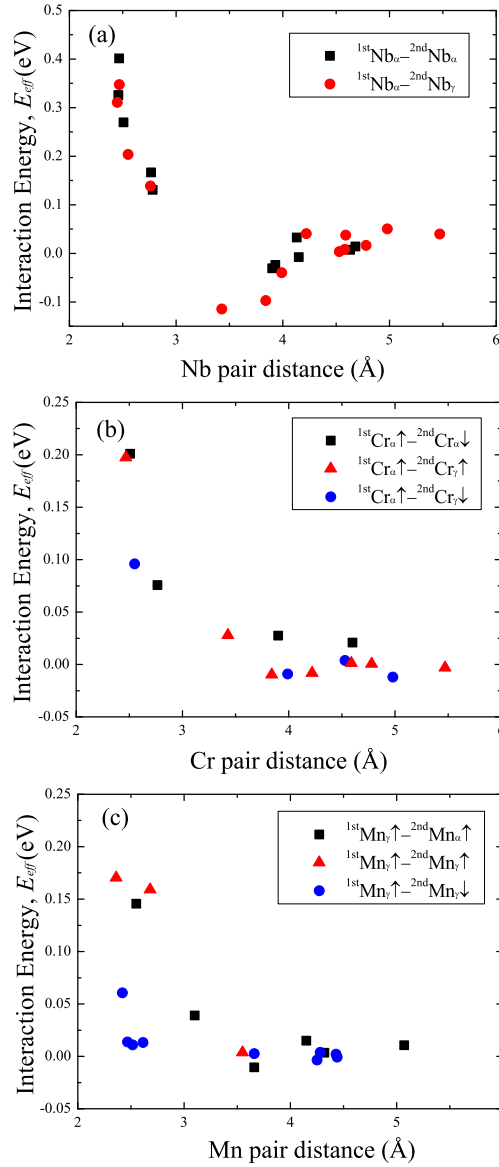


Figure 7.13: Pair interactions for (a) Nb, (b) Cr, and (c) Mn in bcc-fcc Fe interface. The first solute occupies its favorite position. The subscripts α and γ indicate solute atom occupies bcc α - or fcc γ -phase grain, respectively. The superscripts ‘1st’ and ‘2nd’ denote the first and the second substitutional solute atom, respectively. The arrow \uparrow (\downarrow) represents solute atom has spin-up (spin-down) state.

remarkable repulsive interactions are obtained when two Mn atoms occupy adjacent sites with the same spin states. On the other hand, when two Mn atoms occupy positions in the fcc phase with opposite spin states, the interaction between the Mn pair becomes much smaller, i.e. less than 0.06 eV. This can be ascribed to the AFMD magnetic arrangements that reduces the influence of the magnetic frustration.

Chapter 8

Simulation of Self- and Solute-diffusion in Fe

8.1 Diffusion in Fe bcc Lattice

In this work, we consider diffusion occurring through vacancy mediated, thermally activated lattice jumps. The mechanism of vacancy diffusion in bcc Fe is illustrated in Figure 8.1. For pure Fe, the calculated vacancy formation energy (E_v) and migration energy (E_m) are 2.21 eV and 0.63 eV, respectively, which are consistent with the range of values of $E_v=2.18\sim 2.23$ eV and $E_m=0.63\sim 0.68$ eV from previous DFT calculations [11, 163, 164]. The calculated vacancy formation, migration and binding energies, as well as the associated activation energies for self- and solute-diffusion in the ferromagnetic and paramagnetic state are summarized in Table 8.1.

Table 8.1 shows that for all investigated cases, the binding energies of solute-vacancy pairs are negative (attractive). Compared with other solute elements, Nb is found to display the largest binding energy to a neighboring vacancy, which can be understood in terms of a strain-relief argument. The distortion of the Fe lattice due to the oversized atomic radius of Nb results in large attractive interactions between Nb atoms and vacancies.

The migration energies for the solutes in Table 8.1 correspond to a nearest-neighbor exchange with a vacancy. All of the solutes considered here

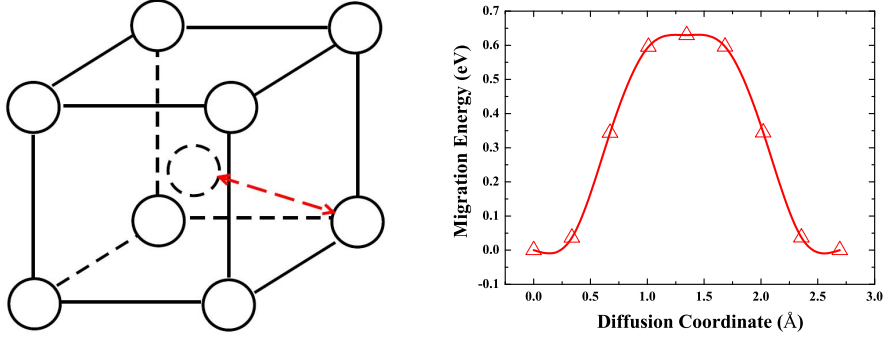


Figure 8.1: First-neighbor diffusion of the vacancy in bcc Fe. One vacancy locates in the center, and diffuses along the red line to the corner of the cubic cell (the corner atom diffuses into the centered vacancy). The calculated migration barrier for vacancy is also shown.

show smaller values of E_m than that for Fe self-diffusion, and Mn exhibits the lowest value. When the vacancy formation, binding and migration energies are combined to compute the ferromagnetic activation energies (Q_0) from Equation 4.15, it is seen that all solutes have a smaller calculated value than that for Fe self-diffusion in the ordered ferromagnetic state.

We focus for the remainder of this section on Mn, Mo, and Nb solute-diffusion. The diffusion coefficient D is expressed in the form of the Arrhenius expression:

$$D = D_0 \exp(-Q_a/k_B T) \quad (8.1)$$

where D_0 is the pre-exponential factor and Q_a is the activation energy above 0K. The influence of the bulk magnetization on the diffusion activation energy is well known [165]. In the whole temperature range across the Curie temperature T_c , Q_a is expressed in the following form:

$$Q_a = Q_0 \left(\frac{1 + \bar{\alpha} s(T)^2}{1 + \bar{\alpha}} \right) \quad (8.2)$$

where $s(T) = M(T)/M(T = 0K)$ is the reduced magnetization at

Table 8.1: Calculated vacancy formation energy (E_v), migration energy (E_m), vacancy-solute binding energy (E_b), and activation energy (Q_0) for self- and solute-diffusion in bcc Fe.

	E_v (eV)	E_m (eV)	E_b (eV)	Q_0 (eV)
Fe	2.21	0.63		2.84
Si		0.43	-0.33	2.31
Ti		0.42	-0.30	2.33
V		0.47	-0.08	2.60
Mn		0.39	-0.23	2.37
Nb		0.40	-0.40	2.21
Mo		0.51	-0.19	2.53

the temperature T , which varies continuously in the ferromagnetic phase between one at 0 K, and zero at the Curie temperature, i.e. $T_c=1043$ K in Fe ($s(T) = 0$ for all T in the paramagnetic state). $s(T)$ can be calculated based on the Onsager and Yang model, which is expressed as [166, 167]:

$$s(T) = (1 - T/T_c)^{1/8} \quad (8.3)$$

In Equation 8.2, the parameter $\bar{\alpha}$ is a species-dependent parameter that quantifies the dependence of Q_a on magnetization. Nitta *et al.* indicated that for solute species where the parameter $\bar{\alpha}$ has not been measured, its value can be estimated from a linear relationship between the magnitudes of $\bar{\alpha}$ and ΔM_{12} [168], which is given by:

$$\bar{\alpha} = 0.053\Delta M_{12} + 0.163 \quad (8.4)$$

where ΔM_{12} is the sum of the change in the local magnetic moments induced on the Fe atoms in the first and second nearest neighbors of an

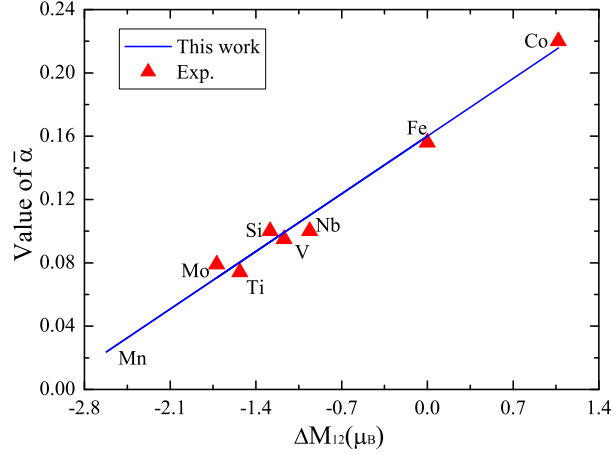


Figure 8.2: Relationship between $\bar{\alpha}$ and ΔM_{12} . The triangles denote the parameter $\bar{\alpha}$ is derived from experiments [169–172] and the line gives the model according to Equation 8.4.

solute atom, i.e.:

$$\Delta M_{12} = \sum_{i=1}^8 \Delta M_i^{1st} + \sum_{i=1}^6 \Delta M_i^{2nd} \quad (8.5)$$

ΔM_{12} can be obtained based on our DFT calculations. In Figure 8.2, the results for measured values of $\bar{\alpha}$ are plotted with triangle symbols. The solid line represents the linear relationship as indicated by Equation 8.5.

In order to compute solute diffusion coefficients, we employ the approach proposed by Asta *et al.*, which is based on the framework of Le Claire’s nine-frequency model [11, 43]. The pre-exponential factor (D_0) can be expressed in terms of the lattice constant (a_l), the correlation factor (f_2), the attempt frequency for the hop of a solute atom to a nearest-neighbor vacancy (ν_0), and the entropy of vacancy formation in Fe (S_v), i.e.:

$$D_0 = a_l^2 f_2 \nu_0 \exp(S_v/k_B) \quad (8.6)$$

where k_B is the Boltzmann constant. In Equation 8.6, the correlation factor (f_2) can be quantitatively evaluated using the nine-frequency model

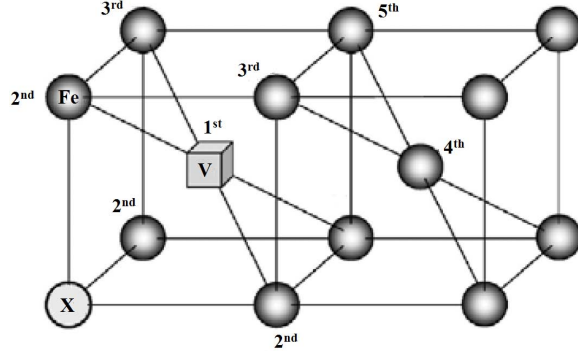


Figure 8.3: An illustration of the different vacancy hops involved in the Le Claire nine-frequency model for the correlation factor for solute diffusion in Fe. X and V denote the solute atom and the vacancy, respectively.

developed by Le Claire [173]. This approach is depended on the jump frequencies as illustrated in Figure 8.3 and are given by:

$$f_2 = \frac{1 + t_1}{1 - t_1} \quad (8.7)$$

where t_1 can be expressed as:

$$t_1 = \frac{\Gamma_X}{\Gamma_X + 3\Gamma_{12} + 3\Gamma_{13} + \Gamma_{15} - \frac{\Gamma_{12}\Gamma_{21}}{\Gamma_{21}+0.512\Gamma_{24}} - \frac{2\Gamma_{13}\Gamma_{31}}{\Gamma_{31}+1.536\Gamma_0} - \frac{\Gamma_{15}\Gamma_{51}}{\Gamma_{51}+3.584\Gamma_0}} \quad (8.8)$$

Here Γ_X , Γ_{ij} , and Γ_0 are the solute-vacancy exchange jump frequency, Fe-vacancy jump frequency from site i to j as illustrated in Figure 8.3, and Fe-vacancy jump frequency in pure Fe. These jump frequencies are calculated according to Equation 4.16

It has been demonstrated that the correlation factors (f_2) display good Arrhenius behavior [119], which can be modeled as:

$$f_2 = f_0 \exp(-E_{f_2}/k_B T) \quad (8.9)$$

where E_{f_2} is defined as the ‘‘correlation energy’’. For Mn, we find E_{f_2} is less than 0.01 eV. While for large solutes, i.e. Mo and Nb, the

calculated correlation energies have small contributions (3% ~5%) to the overall activation energies, which are in agreement with the previous results obtained by Asta *et al.* [11].

In Equation 8.6, the vacancy-formation entropy S_v can be calculated as the difference of the vibrational entropy for a supercell with and without one vacancy, i.e [11]:

$$S_v = k_B \left[\sum_{i=1}^{3(N-1)} \ln\left(\frac{k_B T}{h \nu_i^{eq}}\right) - \frac{N-1}{N} \sum_{i=1}^{3N} \ln\left(\frac{k_B T}{h \nu_i}\right) \right] \quad (8.10)$$

where ν_i^{eq} denotes the vibrational frequencies in a supercell with one vacancy at equilibrium configuration, while ν_i corresponds to the frequencies in a pure Fe system, which are computed from the hessian matrix (see Chapter 4 for detail).

Figure 8.4 provides a direct comparison between calculated and measured temperature-dependent diffusion coefficients for Fe self-diffusion, Mn, Mo and Nb solute-diffusion. For Fe self-diffusion the agreement between calculations and measurements in the ferromagnetic phase is excellent, while the calculated values underestimate some of the measured values in the paramagnetic phase at the highest temperatures [174–176]. For Mn diffusion, our results are slightly (by a factor of 2) higher than the values reported by Lübbekhusen *et al.* in paramagnetic phase [170], while agree well with Kirkaldy *et al.*'s work [177]. For Mo diffusion, the calculated diffusion coefficients show good overall agreement with the experiments, and are roughly in the middle range of the measured values obtained by Nitta *et al.* [172] and Alberry *et al.* [48]. In addition, Figure 8.4c shows previous DFT results for the Mo diffusion coefficient obtained by Asta *et al.* [11], which indicate that our results are consistent with previous DFT calculations. For Nb diffusion, the calculated diffusion coefficients show good overall agreement with the measured values in the ferromagnetic phase obtained by Herzig *et al.* [171]. The calculations are in good agreement with the measurements of Geise *et al.* [178] in the paramagnetic phase as well.

Overall, our calculations predict reasonable results for self- and solute-

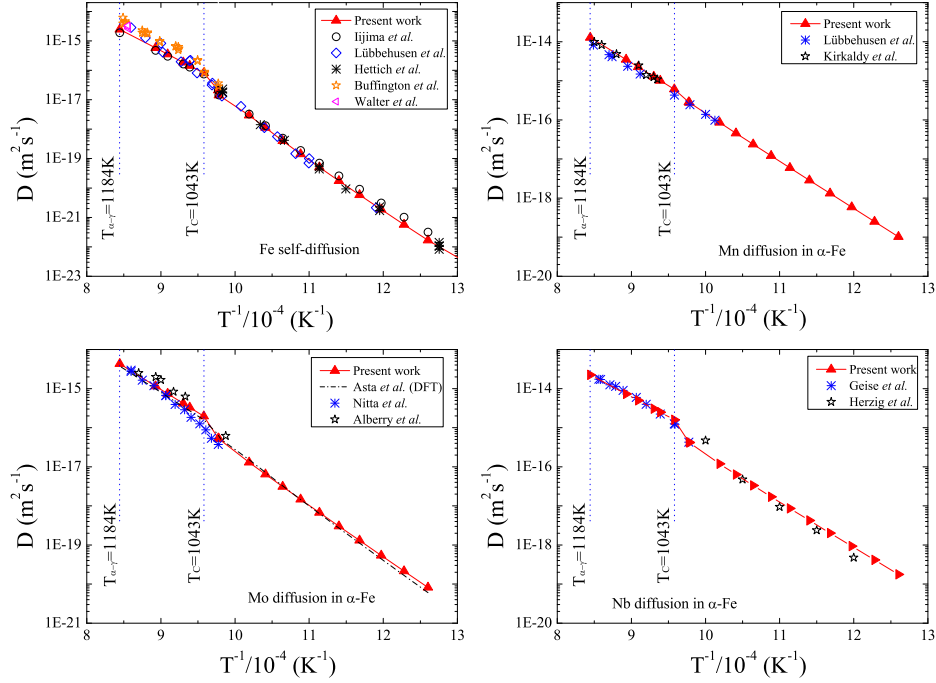


Figure 8.4: Predicted temperature dependence of the calculated α -Fe self-, Mn, Mo, and Nb solute-diffusion coefficients vs. published experimental data [11, 48, 165, 170, 171, 174? –178].

diffusion in the bcc Fe lattice in both para- and ferromagnetic states, which are comparable with the experiments and also previous DFT calculations. The agreement between the computed and measured results demonstrated that the computational methodology presented in this project is capable of predicting quantitative information of the atomistic diffusion processes, which gives us confidence to investigate solute diffusion in grain boundaries and interfaces.

8.2 Diffusion in the Fe fcc Lattice

In this section, AFMD magnetic arrangement is first employed to describe the fcc phase. The calculated vacancy formation energy in pure fcc Fe is 1.72 eV. This value is significantly lower than that in bcc Fe, i.e. 2.21

eV, suggesting that vacancies are much easier to generate in the fcc phase. Such lower vacancy formation energy can be ascribed to the higher packing density in the fcc phase. The migration barriers are then determined using nudged elastic band (NEB) method [105, 106]. In the AFMD configuration, each site (o) has three types of nearest neighbors, namely p , q , and w , which are labeled in Figure 6.1. As a result, three migration paths have to be considered. The results are listed in Table 8.2.

Table 8.2: Vacancy formation energies (E_v), vacancy migration barrier (E_m), and the activation energy for self-diffusion (Q_0) along each path. The migration paths are labeled in Figure 6.1.

Path	AFMD			SQS
	$o-p$	$o-q$	$o-w$	
E_v (eV)	1.72	1.72	1.72	1.92~1.99
E_m (eV)	1.09	0.74	0.93	0.51~0.68
Q_0 (eV)	2.81	2.46	2.65	2.46~2.67

It should be noted that along path $o-w$, the initial and final magnetic moments for the migrating atom have the opposite sign and magnetic moment flips are required along the migration path. Nevertheless, our calculations indicate that the energy cost of magnetic moment flipping is less than 0.05 eV, i.e. less than 5% of the migration energy, and therefore have a relatively small effect on the migration barrier. Overall, the estimated migration energies for vacancies in fcc γ -Fe are in the range of 0.74~1.09 eV, which is about 16% ~ 70% higher than the values in the bcc phase. Combined with the vacancy formation energy, the activation energy for self-diffusion in γ -Fe lies between 2.46 eV and 2.81 eV.

For comparison, the vacancy formation energy, migration energy, and activation energy are also investigated by using the SQS magnetic arrangement. Note that in SQS magnetic structure, the vacancy formation energy and migration energy vary from site to site. In this work, six different

configurations are considered. The results are shown in Table 8.2, from which one can see that though there is some deviations between SQS and AFMD for vacancy formation energies and migration barriers, the activation energies calculated by the two independent magnetic arrangements fall into the same range.

The experimental results of activation energies for fcc self-diffusion are 2.80~2.90 eV [175, 179], which are about 10% higher than our calculated values. This is because our calculations are performed at 0K, whereas the experiments are carried out at high temperature (i.e. $T > 1173$ K). To correlate such deviations, the corresponding lattice constants at high temperature should be employed.

Table 8.3: Lattice constants (a_l), atomic volume (V), vacancy formation energy (E_v), effective migration energy (E_m^{eff}), and effective activation energy (Q_a^{eff}) as a function of temperature.

	a_l (Å)	V (Å ³)	E_v (eV)	E_m^{eff} (eV)	Q_a^{eff} (eV)
bcc (0K)	2.84	11.45	2.21	0.63	2.84
bcc (800K)	2.866	11.77	2.24	0.63	2.87
fcc (0K)	3.55	11.18	1.72	0.87	2.59
fcc (293K)	3.59	11.57	1.87	0.83	2.70
fcc (1184K)	3.65	12.16	1.97	0.81	2.78

To address the influence of the lattice constants due to the thermal expansion, we calculated the vacancy formation energy, effective migration energy, and effective activation energy using different lattice constants. These lattice constants are employed from the experimental measurements at a given temperature T [138, 180]. The results are listed in Table 8.3. In this work, the effective migration energy is calculated via KMC simulations. With the increase of temperature, the effect of lattice constant on the activation energy in the fcc phase is remarkable, while it is rather small in the bcc phase. This is because fcc is the closest-packed structure, which has

12 nearest neighbors. The change of lattice constants induced by thermal expansion results in a larger influence of nearest neighbors Fe atoms on activation energy than that in the bcc phase. Consequently, the activation energy of the fcc phase obtained at $T=1184\text{K}$ is increased to 2.78 eV, which is consistent with the experimental measurements, i.e. 2.80 eV [179]. It should be noted that for the bcc phase, the magnetic transformation has a significant influence on the activation energy, and the activation energy has to be modified according to Equation 8.2. Recall that $\alpha=0.163$ for Fe (see Figure 8.2). Thus the activation energy at a given temperature T is expressed as:

$$Q_a = Q_0 \left(\frac{1 + 0.163s(T)^2}{1.163} \right) \quad (8.11)$$

where $s(T)$ is calculated according to Equation 8.4. The modified activation energies for Fe self-diffusion in bcc and fcc at different temperatures are plotted in Figure 8.5. At low temperature, the activation energy is lower in fcc than in bcc, while it becomes opposite at high temperature.

The diffusion coefficients for Fe self-diffusion in the fcc phase are calculated in the Arrhenius form, i.e.:

$$D = D_0 \exp(-Q_a^{eff}/k_B T) \quad (8.12)$$

where D_0 is the pre-factor, which is given by:

$$D_0 = a_l^2 f_2 \nu_0 \exp(S_v/k_B) \quad (8.13)$$

where the correlation factor $f_2=0.7815$ for fcc. Based on our calculations, the attempt frequencies ν_0 for different jump paths in fcc Fe are very similar, i.e. 9.0 THz, 6.6 THz, and 7.4 THz for jump paths $o-p$, $o-q$, and $o-w$, respectively. For simplicity, we take the average value 7.7 THz, which is also close to the value in the bcc phase, i.e. 8.5 THz. The vacancy formation entropy (S_v) in the fcc phase is $2.8k_B$, which is about 60% of the value in bcc. Consequently, the pre-factor (D_0) in fcc is $9.6 \times 10^{-6} \text{ m}^2/\text{s}$ at zero temperature. The influence of the lattice constants on the pre-factor are also tested. The results indicate that the difference of D_0 is less than 3%.

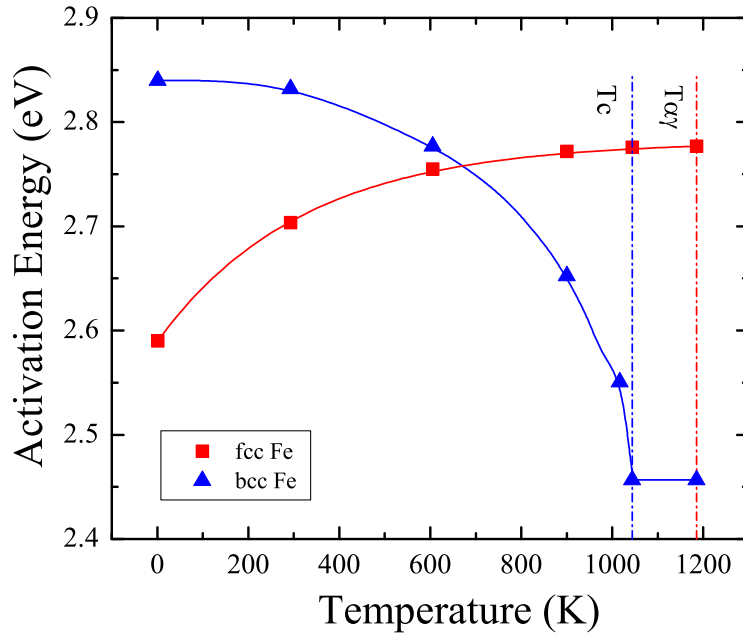


Figure 8.5: The modified activation energies for Fe self-diffusion in bcc and fcc phase at different temperature.

Thus, the pre-factor can indeed be considered as a constant over the relevant temperature range, i.e. 0~1200K.

Figure 8.6 presents the calculated Fe-self diffusion coefficients in bcc and fcc. At lower temperature, the predicted diffusion coefficient is larger in fcc than in bcc, while it becomes opposite at higher temperature. In addition, the calculated self-diffusion coefficients in bcc and fcc at higher temperature agree well with experimental observations [174, 175].

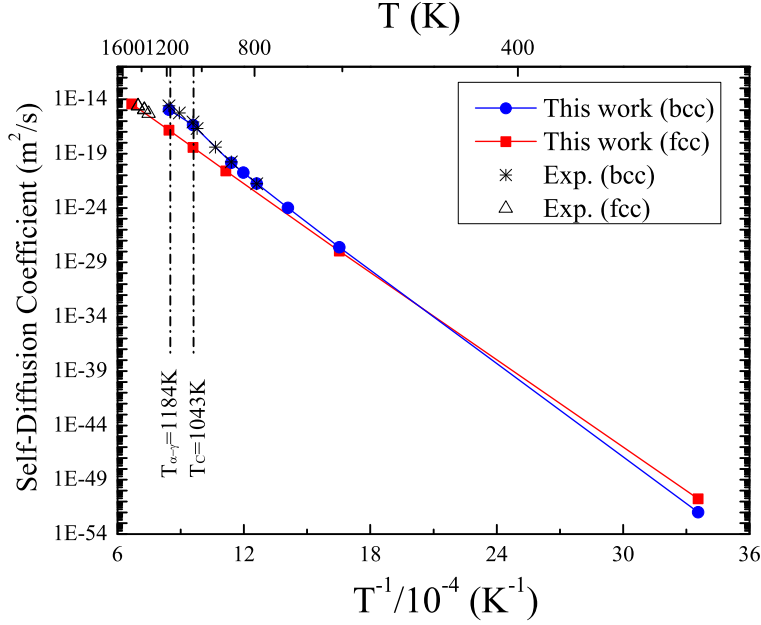


Figure 8.6: Predicted temperature dependence of the Fe-self diffusion coefficients vs. published experimental data in bcc and fcc [174, 175].

8.3 Grain Boundary Diffusion in bcc Fe

The vacancy formation energies (E_v) calculated for several atomic positions within the grain boundary are shown in Figure 8.7. The results indicate that the influence of the grain boundary on E_v is short-ranged and is limited to about 3~4 atomic layers. In addition, it was found that E_v displays very strong site-to-site variations, i.e. at boundary position b , E_v is 0.77 eV (35%) below the bulk value of 2.21 eV, while at boundary site a , the difference is less than 10%. Such large variations in E_v can be attributed to the existence of alternating tension and compression regions in the boundary areas. We find that the nearest Fe-Fe distance at the boundary site b ($d_{bb'}$, see Figure 5.1) is only 2.18Å. It is about 12% shorter than that in the bulk (2.46Å), which gives rise to high strain at this position. While at boundary site a , the nearest Fe-Fe distance (d_{ab}) increases to 2.51Å, resulting in relatively low strain at this

position. Similar results were also reported for Cu grain boundaries [41, 42]. Evidently, lower formation energies favor the accumulations of vacancies in the grain boundary.

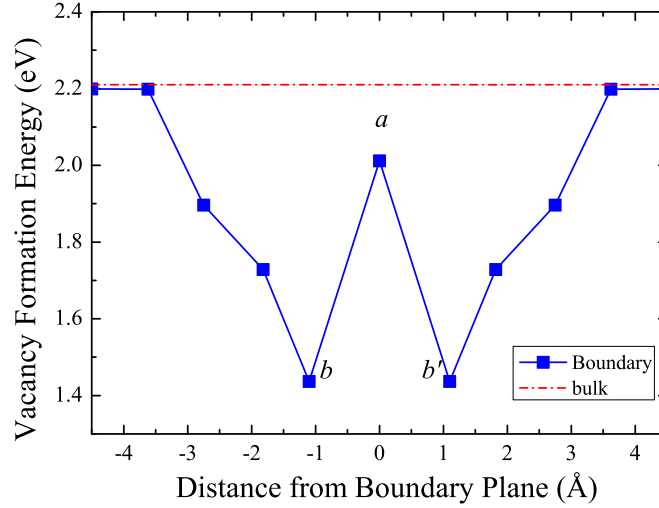


Figure 8.7: Vacancy formation energies at different sites of $\Sigma 5$ (013) grain boundaries in α -Fe. The dotted red line indicates the value in the bulk lattice.

Figure 8.8 shows the calculated binding energies for vacancy-solute pairs. The capital letter X refers to the solute atom while V stands for the vacancy. The subscripts a , b , and c indicate grain boundary positions. A negative sign denotes favorable binding. Overall, the formation of the solute-vacancy pair is energetically favorable. However, similar to E_v , the vacancy-solute binding energies (E_b) vary from site to site. In most of the cases, however, the vacancy-solute binding energies in grain boundaries are comparable with the values in the bulk. While in a couple of cases, the interactions are remarkably weaker than in the bulk, or even show positive (repulsive) values.

The migration energy barriers (E_m) for various solutes along different paths in the $\Sigma 5$ (013) grain boundary are listed in Table 8.4. The jump $b_0 - c$ bridges two neighboring structural units. The jump vector is normal to the tilt [001] axis, so this jump does not contribute to diffusion along the tilt axis. For other jumps, they have components along the tilt axis and can contribute

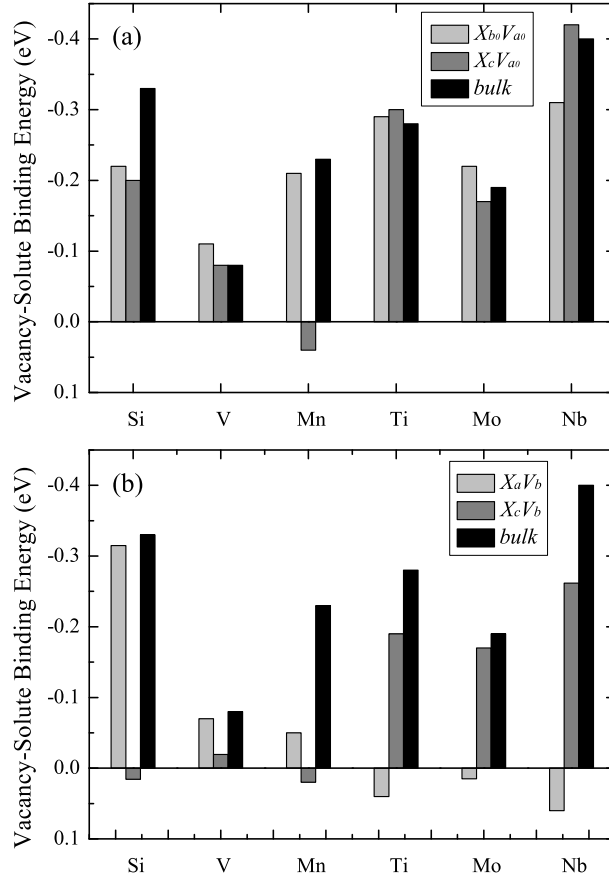


Figure 8.8: Vacancy-solute binding energies at $\Sigma 5$ (013) grain boundaries and bulk in α -Fe. Vacancy segregates at (a) boundary a_0 , and (b) boundary b position. The capital letters X refer to the solute and V refer to the vacancy

to diffusion in both directions in the boundary plane. It is seen that the migration energies can vary for the different paths along the boundary. In general, solutes have a smaller calculated migration energy than that for Fe self-diffusion in the grain boundary, suggesting faster diffusion of solute atoms than Fe self-diffusion.

Unlike the bcc bulk situation, the activation energies of the solutes in the grain boundary depend on the positions, and the jump rates vary at different

Table 8.4: Calculated migration energy for various solutes along grain boundary (E_m , in units of eV). Sites a_0 , b_0 , c_0 , and c refer to boundary sites as shown in Figure 5.1.

<i>Path</i>	a_0-b_0	b_0-a_0	a_0-c	$c-a_0$	b_0-c_0	c_0-b_0	b_0-c	$c-b_0$
Fe	0.91	0.32	0.68	0.40	0.39	0.71	0.45	0.77
Si	0.57	0.42	0.63	0.32	0.28	0.53	0.37	0.62
Ti	0.93	0.18	0.62	0.24	0.18	0.48	0.30	0.60
V	0.88	0.55	0.64	0.28	0.55	0.69	0.41	0.55
Mn	0.84	0.32	0.59	0.21	0.32	0.44	0.31	0.43
Nb	0.98	0.19	0.66	0.22	0.16	0.41	0.24	0.49
Mo	0.85	0.23	0.60	0.31	0.27	0.46	0.34	0.54

sites. To investigate solute diffusion and obtain the effective activation energies, a kinetic Monte Carlo (KMC) model is developed based on the detailed input from DFT calculations. In this work, a thin boundary model with periodic boundary conditions is constructed. As discussed in Chapter 5, the effective thickness of the grain boundary (δ) is about 6 atomic layers ($\sim 4.5 \text{ \AA}$). The ratio of the effective thickness of the grain boundary (δ) to the grain size (d_{gs}) is set to 0.25, i.e. $d_{gs} = 4\delta$. In the KMC model, the supercell consists of $N=8 \times 10^4$ lattice sites with the dimension of $142 \times 180 \times 36 \text{ \AA}^3$. The vacancy concentration is given by $1/N$. To correlate our KMC vacancy concentration with the real case, the physical time is rescaled using the relation [181]:

$$\tau_r = \tau_{kmc} c_v / c_v^{eq} \quad (8.14)$$

where c_v^{eq} is the equilibrium vacancy concentration, which is given by a Boltzmann distribution, i.e.

$$c_v^{eq} = \exp\left(\frac{S_v}{k_B}\right) \exp\left[-\frac{E_v + E_b}{k_B T}\right] \quad (8.15)$$

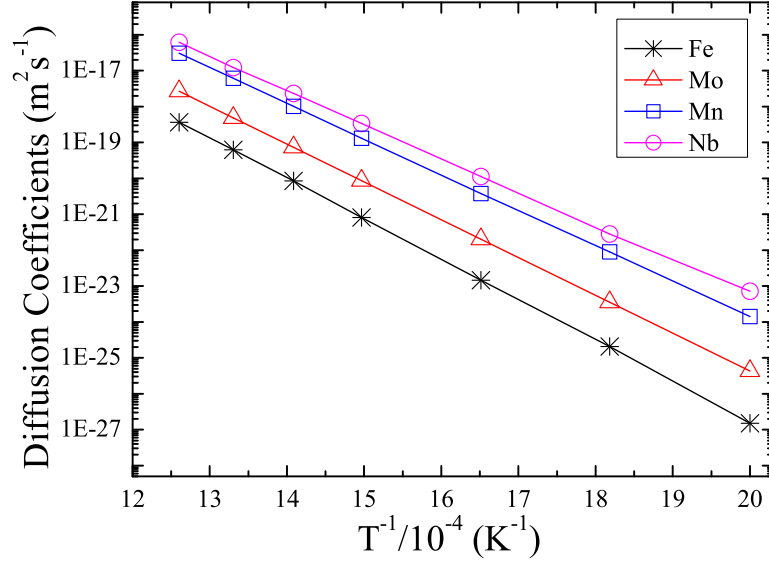


Figure 8.9: Predicted temperature dependence of the calculated Nb, Mo, Mn, and Fe-self diffusion coefficients at grain boundaries.

The apparent diffusion coefficients are determined by Equation 4.22 based on the KMC simulations. According to Equation 4.23, the grain boundary diffusivity is given by:

$$D_b = \frac{d_{gs}}{\delta} (D_{app} - (1 - \frac{\delta}{d_{gs}})D_l) \quad (8.16)$$

When $D_{app} \gg D_l$, diffusion through the bulk lattice can be ignored in comparison to grain boundary diffusion. This is indeed the case in our simulations. At 800K (the highest temperature used in the simulations), the obtained apparent diffusion coefficients for Nb is $1.54 \times 10^{-17} \text{ m}^2/\text{s}$, which is two orders of magnitude larger than the bulk diffusion, i.e. $1.26 \times 10^{-19} \text{ m}^2/\text{s}$ (see Figure 8.4d). The difference is even larger for self-diffusion, which is up to 3 orders of magnitude. Thus, Equation 8.16 can be rewritten as:

$$D_b = \frac{d_{gs}}{\delta} D_{app} \quad (8.17)$$

The calculated Nb, Mo, Mn, and Fe-self diffusion coefficients in $\Sigma 5$ (013)

tilt grain boundary are presented in Figure 8.9. Though the activation energy varies for different diffusion paths, the diffusion coefficients follow the Arrhenius law quite well, which is consistent with the experimental observations for Fe self-diffusion and previous theoretical results for Cu self-diffusion in grain boundaries [41, 42, 182]. In addition, Nb is found to have a much larger diffusion coefficient, which is approximately two orders of magnitude higher than that for Fe self-diffusion. Such an enhanced diffusion coefficient can be ascribed to both the attractive vacancy-solute binding energies and the reduced value of the migration energy (see Figure 8.8 and Table 8.4). The effective activation energy in grain boundaries (Q_{gb}) can be extracted from the slope in the Arrhenius plot shown in Figure 8.9. The results are listed in Table 8.5. Compared with the activation energy in bcc Fe, the effective activation energy in grain boundaries is reduced by 15-20%, which indicates that grain boundaries offer a fast diffusion path.

Table 8.5: The effective activation energy (Q_{gb}) in $\Sigma 5$ (013) grain boundaries and the ratio of Q_{gb}/Q_{bulk} .

	Fe	Si	Ti	V	Mn	Nb	Mo
Q_{gb} (eV)	2.27	1.96	1.92	2.14	1.98	1.83	2.10
Q_{gb}/Q_{bulk}	0.80	0.85	0.82	0.82	0.84	0.83	0.83

Experimental values for diffusion in grain boundaries are limited. Nevertheless, the calculated activation energy for self-diffusion in pure Fe grain boundary are comparable with experimental data, which lies between 1.46~2.34 eV when extrapolated to the ferromagnetic phase [182, 183]. It is interesting to note that Turnbull and Hoffman who studied self-diffusion in [001] grain boundaries in silver as a function of crystal misorientation (θ) found that within the experimental uncertainty, the self-diffusion coefficients in different grain boundaries are independent of θ . Similar results were also obtained by Suzuki and Mishin [42]. They studied Cu self-diffusion in several tilt grain boundaries by molecular dynamics simulations and found that the

conclusions reached for the $\Sigma 5$ grain boundary are general and hold for other grain boundaries as well. Thus, one would expect that the tendency for solute diffusivities at the considered $\Sigma 5$ grain boundary can be extended to more general boundaries. Further calculations are needed to confirm this assumption.

8.4 Diffusion in the bcc-fcc Fe Interface

Figure 8.10 presents the vacancy formation energy at the bcc-fcc interface as a function of distance from the habit plane. The AFMD configuration is employed to describe the magnetic states of fcc. The results indicate that there exists a chemical potential gradient for vacancies between ferrite and austenite. Vacancies form much easier in austenite than in ferrite. In addition, lower vacancy formation energies are observed at the interface positions on the austenite side. Similar to the case of grain boundaries, the influence of the interface on the vacancy formation energy is short-ranged, i.e. the bulk value of the vacancy formation energy is achieved approximately 4 Å away from the interface.

We then calculated the migration energy of vacancies in the bcc-fcc interface. Due to the asymmetric structure, the jump rates vary from site to site. The jump paths are illustrated in Figure 8.11, which can be categorized into five groups: (*I*) migration from the second layer to the first layer in bcc; (*II*) migration within the first layer in bcc; (*III*) migration from the bcc side to the fcc side of the interface; (*IV*) migration within the first layer in fcc; and (*V*) migration from the second layer to the first layer in fcc. The calculated migration energies (E_m) for different types of jumps are listed in Table 8.6. In addition, the migration energy for opposite jump direction (E'_m) are also shown.

The results indicate that in general, E_m is smaller compared with the bulk value. For example, the migration energies from the second layer to the first layer in bcc (group *I*) are 0.55 eV, which are about 13% lower than the bcc bulk value, i.e. 0.63 eV. In addition, the migration energies have lower values when the vacancy moves from the inner grain (second layer) to

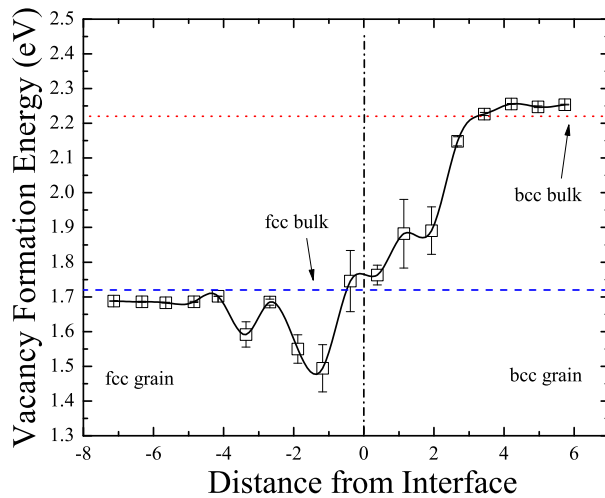


Figure 8.10: Vacancy formation energies as a function of distance from the habit plane. The bars indicate the actual vacancy formation energies, where Fe atom has spin-up or spin-down states.

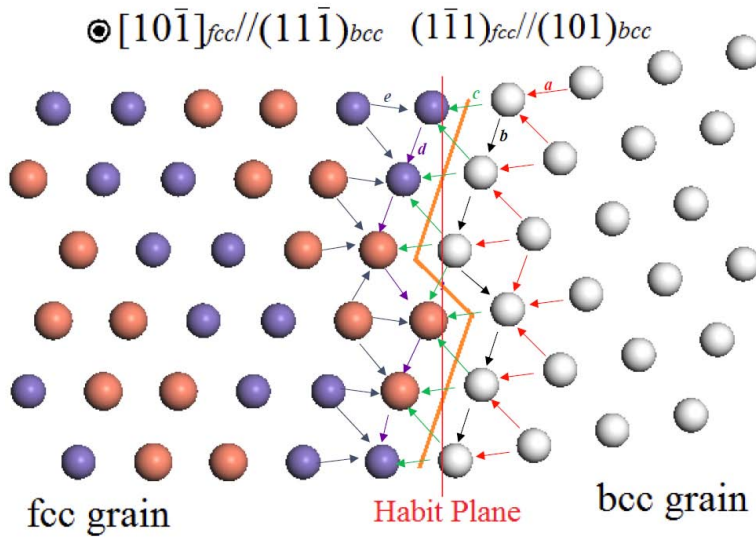


Figure 8.11: Illustration of various jump paths in the bcc-fcc interface. Blue and red circles indicate fcc Fe atoms with spin-down and spin-up magnetic state, while white circles represent bcc Fe atoms.

Table 8.6: Migration energies of vacancy for different types of jump paths as defined in the text in the bcc-fcc interface. The arrows indicate the spin states of the jump Fe atoms in initial and final states.

	E_m	E'_m
<i>I</i> ($\uparrow\uparrow$)	0.55	0.69
<i>II</i> ($\uparrow\uparrow$)	0.60	0.56
<i>III</i> ($\uparrow\uparrow$)	0.52	0.71
<i>III</i> ($\uparrow\downarrow$)	0.58	0.68
<i>IV</i> ($\uparrow\uparrow$)	0.65	0.66
<i>IV</i> ($\downarrow\downarrow$)	0.58	0.76
<i>IV</i> ($\uparrow\downarrow$)	0.58	0.49
<i>V</i> ($\uparrow\uparrow$)	0.61	0.66
<i>V</i> ($\downarrow\downarrow$)	0.70	0.76
<i>V</i> ($\uparrow\downarrow$)	0.70	0.83

the interface (first layer) than when it moves in the opposite directions. As a result, vacancies are expected to be confined to the interface, which are consistent with the experimental observations that interfaces act as a sink for vacancies.

Table 8.7: Activation energy for Fe self-diffusion in the bcc-fcc interface, fcc bulk, bcc bulk, and $\Sigma 5$ grain boundaries (GBs) at 0K. Unit is eV.

	Interface	fcc bulk	bcc bulk	$\Sigma 5$ GBs
Q_0	2.46	2.59	2.84	2.27

The apparent diffusion coefficients in the bcc-fcc interface is determined by Equation 4.22 based on the KMC simulations. In a similar manner with

the grain boundary, if the interface has an effective thickness δ_α in bcc and δ_γ in fcc, and the bcc (fcc) grain size is d_α (d_γ), the apparent diffusion coefficient (D_{app}) is expressed as:

$$D_{app} = \frac{d_\alpha - \delta_\alpha}{d_\alpha + d_\gamma} D_l^\alpha + \frac{d_\gamma - \delta_\gamma}{d_\alpha + d_\gamma} D_l^\gamma + \frac{\delta_\alpha + \delta_\gamma}{d_\alpha + d_\gamma} D_I \quad (8.18)$$

where D_l^α , D_l^γ and D_I are the bcc bulk, fcc bulk, and bcc-fcc interface diffusivities. As discussed in Chapter 7, the effective thickness of the bcc-fcc interface is about 7.0 Å. We set $d_\alpha/\delta_\alpha=d_\gamma/\delta_\gamma=5$. The supercell consists of $N = 2.16 \times 10^5$ lattice sites with the dimension of $197 \times 184 \times 67$ Å³. D_l^α and D_l^γ are obtained directly from the DFT calculations (see sections 8.1 and 8.2). Since the influence of the thermal expansion and magnetic transformation on the interface diffusion is unclear, we did not include these effects in our calculations. So in the simulations, we use the activation energies Q_0 at $T=0$ K to calculate the Fe self-diffusions without any further corrections for lattice constants and magnetism at higher temperature. The interface diffusivity D_I is thus determined by Equation 8.18.

The effective activation energy in the bcc-fcc interface can be extracted from the slope in the Arrhenius plot for the interface diffusivity. The result is shown in Table 8.7. For comparison, the activation energies for Fe self-diffusion in the fcc bulk, bcc bulk, and in the $\Sigma 5$ bcc grain boundary are also listed. Compared with the values in bulk diffusion, bcc-fcc interface provide a moderate “fast diffusion” path. However, it should be noted that at elevated temperature, the thermal expansion and magnetic transformation have significant influence on the activation energies for diffusion in fcc and bcc, respectively. As a result, it can be expected that the activation energy in the bcc-fcc interface is modified at higher temperature as well. Therefore, new theoretical models and simulation tools are required.

Chapter 9

Conclusions and Future Work

9.1 Conclusions

This work demonstrates an atomistic modeling scheme for the simulation of solute-interface interactions in Fe, which provides a basis for further investigations. The binding energies of solutes with grain boundaries and bcc-fcc interfaces are determined based on the framework of DFT calculations. The calculated jump rates are set as the input data for KMC simulations to obtain the diffusion coefficients and effective activation energies. The main simulation results are summarized below:

- Strong interactions between large solutes (i.e. Nb, Mo, and Ti) and $\Sigma 5$ grain boundaries in bcc and fcc Fe as well as the bcc-fcc interface are obtained. Such strong interactions are expected to delay grain growth, recrystallization, and ausenite-to-ferrite transformation. This can be understood in terms of the strain-relief argument, where large solutes bind to the grain boundary or interface as a means of relieving strain on the Fe matrix.
- It is found that segregation to the $\Sigma 5$ bcc grain boundaries are favorable for all solutes and boundary sites considered in this work, and

the magnitude of the segregation energy of the solute atoms increases with the solute atom volume.

- Our DFT calculations indicate that the excess volume at boundaries and interfaces is an important parameter to predict the segregation tendency of solutes. This is in particular of significance for large solute atoms (i.e. Nb, Mo, and Ti). Further, molecular statics simulations reveal that though the site volume distribution is much narrower for the $\Sigma 5$ grain boundary, the average excess volume is comparable to that for high Σ grain boundaries, suggesting that the tendency to accommodate solute atoms at the considered $\Sigma 5$ grain boundary can, to a large extent, be applied to more general boundaries.

- A large set of possible reference states for γ -Fe at 0 K have been evaluated and the AFMD and SQS configurations are found to be the most suitable magnetic states. Though SQS may give more realistic results for paramagnetic γ -Fe, the properties such as vacancy formation energy, solute pair interactions, etc. vary from site to site, which requires a large computational load. Further calculations indicate that the results obtained by AFMD and SQS magnetic structures are comparable to each other, suggesting AFMD structure is a good and more convenient representative for paramagnetic γ -Fe.

- It is found that some of the boundary sites are not favorable for solute segregation at the $\Sigma 5$ grain boundary in fcc Fe. Positive segregation energies are observed for Cr and Si. In addition, no segregation tendency of Ni to fcc grain boundary is found, which implies that Ni prefers to stay at the bulk position rather than at the boundary sites. On the contrary, Large binding energies for Nb and Mo are obtained at the $\Sigma 5$ grain boundary in fcc Fe. The interactions between these solutes and the fcc grain boundary are even stronger than those at the bcc grain boundary.

- In the bcc-fcc interface, a chemical potential difference exists for the substitutional elements between ferrite and austenite. This difference is rather large for Mn and Ni, which provided considerable driving force for solute transfer from ferrite to austenite.

- Using the average energies between the two bulk values as the reference point, we calculate the effective binding energies of selected solutes in the bcc-fcc interface based on the Langmuir-McLean equation. Good agreement with the experimental observations for solute segregation are shown. The reported interaction parameters for Nb, Mo Mn, and Si agree well with our predictions. The tendency predicted for segregation, in particular the strong segregation of Nb, is consistent with observations of the role of Nb in delaying austenite-ferrite transformation in low-carbon steels, which at least in part have been attributed to solute drag.

- The solute-solute interactions and their predicted contributions to the segregation energies indicate that there is a massive penalty to the binding energy when the solute-solute distance is short. While at some intermediate solute-solute distance, co-segregation effects are observed for large solute elements (i.e. Nb, Mo, and Ti) and the binding energies are increased by about 30%. A detailed analysis reveals that for TMs, there are mainly three aspects that contribute to the solute-solute interactions, i.e. elastic strains, competing magnetic interactions, and contributions from magnetically driven clustering. In addition, for non-metal element such as Si, the chemical bonding effects may also contribute to the solute pair interactions.

- The self- and solute-diffusivities in bcc and fcc bulk lattice have been computed within a framework combining DFT calculations and KMC simulations. Good agreement between our calculations and the measurements for self- and solute diffusion in bulk Fe is achieved, which demonstrates the computational methodology presented in this project is capable of predicting quantitative information of the atomistic processes.

- Our simulations indicate that the effective activation energies for the $\Sigma 5$ bcc grain boundary diffusion are 80%~85% of those for lattice diffusion for different solutes, suggesting grain boundaries can provide fast diffusion paths. By contrast, the effective activation energy of self-diffusion in bcc-fcc Fe interface is close to the value of fcc self-diffusion at 0K, and bcc-fcc interface provides a moderate “fast diffusion” path.

9.2 Future Work

To further enhance the present understanding, several suggestions can be made for further investigations as follow:

- The present study focuses on the special grain boundaries, i.e. $\Sigma 5$ grain boundary. Further work is required to understand the solute segregation behavior at more general, e.g. high Σ or low angle, grain boundaries. This could be achieved by employing the hybrid method, i.e. quantum mechanics/molecular mechanics (QM/MM) approach, which combines the strengths of the accuracy of quantum mechanics and the efficiency of molecular mechanics [184, 185].

- It is demonstrated that the lattice constants due to the thermal expansion and the magnetic transformation at elevated temperature have a significant influence on the diffusion coefficients in fcc and bcc, respectively. Thus, new theoretical models and simulation tools are required to modify the activation energies for diffusion across the bcc-fcc interface at higher temperature.

- Carbon is one of the most important elements in steels. Further work will have to be done to incorporate carbon into the system. In particular, the interactions between carbon and alloying elements and the influence of carbon on the solute segregation should be investigated.

Bibliography

- [1] A. Yoshie, M. Fujioka, Y. Watanabe, K. Nishioka, and H. Morikawa, “Modelling of microstructural evolution and mechanical properties of steel plates produced by thermo-mechanical control process,” *ISIJ International*, vol. 32, no. 3, pp. 395–404, 1992. → pages 2
- [2] M. Militzer, “Computer simulation of microstructure evolution in low carbon sheet steels,” *ISIJ International*, vol. 47, no. 1, pp. 1–15, 2007. → pages 2
- [3] G. E. Murch and A. S. Nowick, *Diffusion in crystalline solids*. Academic Press, Orlando, 1984. → pages 2, 17
- [4] Y. Mishin, M. Asta, and J. Li, “Atomistic modeling of interfaces and their impact on microstructure and properties,” *Acta Mater.* → pages 2, 3, 14, 17
- [5] S. Shahahndeh, *Phase Field Modelling of Grain Growth with Particle Pinning and Solute Drag*. PhD thesis, The University of British Columbia, 2013. → pages x, 2
- [6] K. Lücke and K. Detert, “A quantitative theory of grain-boundary motion and recrystallization in metals in the presence of impurities,” *Acta Metallurgica*, vol. 5, no. 11, pp. 628 – 637, 1957. → pages 3
- [7] J. W. Cahn, “The impurity-drag effect in grain boundary motion,” *Acta Metallurgica*, vol. 10, no. 9, pp. 789–798, 1962. → pages 3
- [8] M. Hillert and B. Sundman, “A treatment of the solute drag on moving grain boundaries and phase interfaces in binary alloys,” *Acta Metallurgica*, vol. 24, no. 8, p. 3436, 1976. → pages 3
- [9] D. E. Jiang and E. A. Carter, “Carbon dissolution and diffusion in ferrite and austenite from first principles,” *Physical Review B*, vol. 67, p. 214103, Jun 2003. → pages xi, xii, 4, 17, 18, 19, 26, 27, 28

- [10] R. Wu, A. J. Freeman, and G. B. Olson, “First Principles Determination of the Effects of Phosphorus and Boron on Iron Grain-Boundary Cohesion,” *Science*, vol. 265, pp. 376–380, 1994. → pages 7
- [11] S. Huang, D. L. Worthington, M. Asta, V. Ozolins, G. Ghosh, and P. K. Liaw, “Calculation of impurity diffusivities in α -Fe using first-principles methods,” *Acta Materialia*, vol. 58, no. 6, pp. 1982 – 1993, 2010. → pages xvii, 4, 17, 19, 43, 51, 111, 114, 116, 117
- [12] M. Militzer, J. Hoyt, N. Provatas, J. Rottler, C. Sinclair, and H. Zurob, “Multiscale modeling of phase transformations in steels,” *JOM*, vol. 66, no. 5, pp. 740–746, 2014. → pages 5
- [13] M. Samaras, “Multiscale Modelling: the role of helium in iron,” *Materials Today*, vol. 12, p. 46, 2009. → pages 6
- [14] R. Wu, A. J. Freeman, and G. B. Olson, “On the electronic basis of the phosphorus intergranular embrittlement of iron,” *Journal of Materials Research*, vol. 7, pp. 2403–2411, 1992. → pages 7, 16
- [15] S. Tang, A. J. Freeman, and G. B. Olson, “Phosphorus-induced relaxation in an iron grain boundary: A cluster-model study,” *Physical Review B*, vol. 47, pp. 2441–2445, Feb 1993. → pages x, 7, 8
- [16] R. Wu, A. J. Freeman, and G. B. Olson, “Effects of carbon on Fe-grain-boundary cohesion: First-principles determination,” *Physical Review B*, vol. 53, pp. 7504–7509, 1996. → pages 7
- [17] W. T. Geng, A. J. Freeman, R. Wu, and G. B. Olson, “Effect of Mo and Pd on the grain-boundary cohesion of Fe,” *Physical Review B*, vol. 62, pp. 6208–6214, 2000. → pages 7, 16
- [18] M. Tschopp, M. Horstemeyer, F. Gao, X. Sun, and M. Khaleel, “Energetic driving force for preferential binding of self-interstitial atoms to Fe grain boundaries over vacancies ,” *Scripta Materialia*, vol. 64, no. 9, pp. 908 – 911, 2011. → pages 9
- [19] M. A. Tschopp, K. N. Solanki, F. Gao, X. Sun, M. A. Khaleel, and M. F. Horstemeyer, “Probing grain boundary sink strength at the nanoscale: Energetics and length scales of vacancy and interstitial absorption by grain boundaries in α -Fe,” *Physical Review B*, vol. 85, p. 064108, Feb 2012. → pages x, 9, 10

- [20] N. R. Rhodes, M. A. Tschopp, and K. N. Solanki, “Quantifying the energetics and length scales of carbon segregation to α -Fe symmetric tilt grain boundaries using atomistic simulations,” *Modelling and Simulation in Materials Science and Engineering*, vol. 21, p. 035009, March 2013. → pages 7, 9
- [21] K. T. Aust and B. Chalmers, “Structure of Grain Boundaries,” *Metallurgical Transactions*. → pages 7
- [22] A. Brokman and R. Balluffi, “Coincidence Lattice Model for the Structure and Energy of Grain-Boundaries,” *Acta Metallurgica et Materialia*, vol. 29, no. 10, pp. 1703 – 1719, 1981. → pages 7
- [23] S. Gesari, M. Pronsato, and A. Juan, “The electronic structure and bonding of H pairs at $\Sigma=5$ BCC Fe grain boundary ,” *Applied Surface Science*, vol. 187, no. 3-4, pp. 207 – 217, 2002. → pages 8
- [24] S. Gesari, M. Pronsato, and A. Juan, “Quantum chemical study of sulfur and hydrogen at the $\Sigma=5$ BCC Fe grain boundary ,” *Journal of Physics and Chemistry of Solids*, vol. 65, no. 7, pp. 1337 – 1344, 2004. → pages 8
- [25] E. Wachowicz, T. Ossowski, and A. Kiejna, “Cohesive and magnetic properties of grain boundaries in bcc Fe with Cr additions,” *Physical Review B*, vol. 81, p. 094104, Mar 2010. → pages x, 8, 9, 12, 17, 43, 96
- [26] E. Wachowicz and A. Kiejna, “Effect of impurities on grain boundary cohesion in bcc iron,” *Comput. Mater. Sci.*, vol. 43, no. 4, pp. 736 – 743, 2008. → pages 12
- [27] E. Wachowicz and A. Kiejna, “Effect of impurities on structural, cohesive and magnetic properties of grain boundaries in α -Fe,” *Modelling Simul. Mater. Sci. Eng.*, vol. 19, p. 025001, Jan 2011. → pages 9, 12, 15, 17, 43
- [28] S. K. Bhattacharya, S. Tanaka, Y. Shihara, and M. Kohyama, “*Ab initio* study of symmetrical tilt grain boundaries in bcc fe: structural units, magnetic moments, interfacial bonding, local energy and local stress,” *Journal of Physics: Condensed Matter*, vol. 25, no. 13, p. 135004, 2013. → pages 9, 96

- [29] T. Frolov, D. L. Olmsted, M. Asta, and Y. Mishin, “Structural phase transformations in metallic grain boundaries,” *Nat Commun*, vol. 4, no. 1899, pp. 1–7. → pages xi, 10, 11
- [30] T. Frolov, S. V. Divinski, M. Asta, and Y. Mishin, “Effect of Interface Phase Transformations on Diffusion and Segregation in High-Angle Grain Boundaries,” *Phys. Rev. Lett.*, vol. 110, p. 255502, Jun 2013. → pages 10
- [31] M. Yamaguchi, K.-I. Ebihara, M. Itakura, T. Kadoyoshi, T. Suzudo, and H. Kaburaki, “First-Principles Study on the Grain Boundary Embrittlement of Metals by Solute Segregation: Part II. Metal (Fe, Al, Cu)-Hydrogen (H) Systems,” *Metallurgical and Materials Transactions A*, vol. 42, no. 2, pp. 330–339, 2011. → pages 12
- [32] R. Matsumoto, M. Riku, S. Taketomi, and N. Miyazaki, “Hydrogen-Grain Boundary Interaction in Fe, FeCC, and FeCN Systems,” *Progress in Nuclear Science and Technology*, vol. 2, pp. 9–15, 2011. → pages 12
- [33] S. Gesari, B. Irigoyen, and A. Juan, “Segregation of H, C and B to $\Sigma=5(013)$ α -Fe grain boundary: A theoretical study,” *Applied Surface Science*, vol. 253, no. 4, pp. 1939 – 1945, 2006. → pages 12, 16
- [34] M. Yamaguchi, M. Shiga, and H. Kaburaki, “Grain Boundary Decohesion by Sulfur Segregation in Ferromagnetic Iron and Nickel –A First-Principles Study,” *Materials Transactions*, vol. 11, pp. 2682–2689, Nov 2006. → pages xi, 12, 13
- [35] M. Yamaguchi, “First-Principles Study on the Grain Boundary Embrittlement of Metals by Solute Segregation: Part I. Iron (Fe)-Solute (B, C, P, and S) Systems,” *Metallurgical and Materials Transactions A*, vol. 42, no. 2, pp. 319–329, 2011. → pages xi, 12, 13, 14
- [36] M. Rajagopalan, M. Tschopp, and K. Solanki, “Grain boundary segregation of interstitial and substitutional impurity atoms in alpha-iron,” *arXiv:1310.3413*, 2013. → pages 13, 54
- [37] J. R. Rice and J. S. Wang, “Embrittlement of Interfaces by Solute Segregation,” *Materials Science and Engineering: A*. → pages 15

- [38] J. Braithwaite and P. Rez, “Grain boundary impurities in iron,” *Acta Materialia*, vol. 53, pp. 2715–2726, 2005. → pages 15, 16
- [39] H. Momida, Y. Asari, Y. Nakamura, Y. Tateyama, and T. Ohno, “Hydrogen-enhanced vacancy embrittlement of grain boundaries in iron,” *Physical Review B*, vol. 88, p. 144107, Oct 2013. → pages xi, 15, 16
- [40] W. G. K. Inderjeet, Yuri Mishin, *Fundamentals of grain and interphase boundary diffusion*. New York, John Wiley., 1984. → pages 17
- [41] M. R. Sørensen, Y. Mishin, and A. F. Voter, “Diffusion mechanisms in cu grain boundaries,” *Physical Review B*, vol. 62, pp. 3658–3673, 2000. → pages 17, 20, 21, 22, 54, 123, 127
- [42] A. Suzuki and Y. Mishin, “Interaction of point defects with grain boundaries in fcc metals,” *Interface Science*, vol. 11, p. 131, 2003. → pages xi, xii, 20, 21, 22, 25, 54, 123, 127
- [43] H. Ding, S. Huang, G. Ghosh, P. K. Liaw, and M. Asta, “A computational study of impurity diffusivities for 5d transition metal solutes in α -fe,” *Scripta Materialia*, vol. 67, pp. 732 – 735, 2012. → pages 17, 19, 51, 114
- [44] C. A. Wert, “Diffusion Coefficient of C in α -Iron,” *Phys. Rev.*, vol. 79, pp. 601–605, Aug 1950. → pages 18, 19
- [45] Y. Chen, C.-L. Fu, K.-M. Ho, and B. N. Harmon, “Calculations for the transverse N-point phonons in bcc Zr, Nb, and Mo,” *Phys. Rev. B*, vol. 31, pp. 6775–6778, May 1985. → pages 19
- [46] V. P. Ramunni, R. C. Pasianot, and P. Bruzzoni, “Search of hydrogen transition states on α -Fe: The monomer adapted to first principles calculations,” *Materials Science and Engineering: A*. → pages 19
- [47] S. Takemoto, H. Nitta, Y. Iijima, and Y. Yamazaki, “Diffusion of tungsten in α -iron,” *Philosophical Magazine*, vol. 87, no. 11, pp. 1619–1629, 2007. → pages 19
- [48] P. J. Alberry and C. W. Haworth, “Interdiffusion of Cr, Mo, and W in Iron,” *Met. Sci. J.*, vol. 8, no. 12, pp. 407–412, 1974. → pages xvii, 19, 116, 117

- [49] A. T. Davenport and R. W. K. Honeycombe, "The Secondary Hardening of Tungsten Steels," *Metal Science*, vol. 9, no. 1, pp. 201–208, 1975. → pages 19
- [50] J. Kucera, B. Million, and K. Cihá, "Diffusion of Alloying Elements in Ferrite of Heat-Resistant Steels," *Koveve Mater*, vol. 7, p. 97, 1969. → pages 19
- [51] C. S. Becquart and C. Domain, "Ab initio contribution to the study of complexes formed during dilute FeCu alloys radiation," *Nuclear Instruments and Methods in Physics Research: B*, vol. 202, pp. 44–50, 2003. → pages 19
- [52] S. J. Rothman, N. L. Peterson, C. M. Walter, and L. J. Nowicki, "The Diffusion of Copper in Iron," *Journal of Applied Physics*, vol. 39, no. 11, pp. 5041–5044, 1968. → pages 19
- [53] S. Choudhury, L. Barnard, J. Tucker, T. Allen, B. Wirth, M. Asta, and D. Morgan, "Ab-initio based modeling of diffusion in dilute bcc Fe-Ni and Fe-Cr alloys and implications for radiation induced segregation," *Journal of Nuclear Materials*, vol. 411, no. 1C3, pp. 1 – 14, 2011. → pages 19
- [54] R. Borg and D. Lai, "The diffusion of gold, nickel, and cobalt in alpha iron: A study of the effect of ferromagnetism upon diffusion," *Acta Metallurgica*, vol. 11, no. 8, pp. 861 – 866, 1963. → pages 19
- [55] S. Choudhury, L. Barnard, J. Tucker, T. Allen, B. Wirth, M. Asta, and D. Morgan, "Ab-initio based modeling of diffusion in dilute bcc Fe-Ni and Fe-Cr alloys and implications for radiation induced segregation," *Journal of Nuclear Materials*, vol. 411, no. 1C3, pp. 1 – 14, 2011. → pages 19
- [56] H. Amara, C. C. Fu, F. Soisson, and P. Maugis, "Aluminum and vacancies in α -iron: Dissolution, diffusion, and clustering," *Physical Review B*, vol. 81, p. 174101, May 2010. → pages 19
- [57] M. Koiwa, K. Hirano, H. Nakajima, and T. Okada, "Impurity and Chemical Diffusion of Al in BCC and FCC Iron," *Defect and Diffusion Forum*, vol. 95-98, pp. 709–714, 1992. → pages 19
- [58] J. R. G. da Silva and R. B. McLellan, "Diffusion of carbon and nitrogen in B.C.C. iron," *Materials Science and Engineering*, vol. 26, no. 1, pp. 83–87, 1976. → pages 19

- [59] Y. Hayashi and W. M. Shu, “Iron (ruthenium and osmium)-hydrogen systems,” *Hydrogen in Metal Systems II*, vol. 73-75, pp. 65–114, 2000. → pages 19
- [60] J.-W. Jang, J. Kwon, and B.-J. Lee, “Effect of stress on self-diffusion in bcc Fe: An atomistic simulation study ,” *Scripta Materialia*, vol. 63, no. 1, pp. 39 – 42, 2010. → pages 20
- [61] Y.-N. Wen, Y. Zhang, J.-M. Zhang, and K.-W. Xu, “Atomic diffusion in the Fe [001] $\Sigma=5$ (310) and (210) symmetric tilt grain boundary,” *Comp. Mater. Sci.*, vol. 50, no. 7, pp. 2087 – 2095, 2011. → pages 20, 21
- [62] H.-B. Zhou, Y.-L. Liu, C. Duan, S. Jin, Y. Zhang, F. Gao, X. Shu, and G.-H. Lu, “Effect of vacancy on the sliding of an iron grain boundary,” *J. Appl. Phys.*, vol. 109, p. 113512, Jun 2011. → pages 21
- [63] A. Brokman, P. D. Bristowe, and R. W. Balluffi, “Computer simulation study of the structure of vacancies in grain boundaries,” *Journal of Applied Physics*, vol. 52, no. 10, pp. 6116–6127, 1981. → pages 21, 24, 55, 76
- [64] T. Kwok, P. S. Ho, S. Yip, R. W. Balluffi, P. D. Bristowe, and A. Brokman, “Evidence for Vacancy Mechanism in Grain Boundary Diffusion in bcc Iron: A Molecular-Dynamics Study,” *Phys. Rev. Lett.*, vol. 47, pp. 1148–1151, Oct 1981. → pages 21, 24
- [65] F. Gao, H. Heinisch, and R. Kurtz, “Migration of vacancies, He interstitials and He-vacancy clusters at grain boundaries in α -Fe ,” *Journal of Nuclear Materials*, vol. 386C388, no. 0, pp. 390 – 394, 2009. → pages xi, 22, 23
- [66] Y. Lei, Y. Gong, Z. Duan, and G. Wang, “Density functional calculation of activation energies for lattice and grain boundary diffusion in alumina,” *Physical Review B*, vol. 87, p. 214105, Jun 2013. → pages 22, 24
- [67] X. Y. Liu, W. B. Xie, and H. Zhang, “Effects of grain boundary and boundary inclination on hydrogen diffusion in α -iron,” *Journal of Materials Research*, vol. 26, no. 21, pp. 2735–2743, 2011. → pages xii, 23, 24

- [68] K. Ingle and A. Crocker, “Migration of Vacancies near Twin Boundaries in Body-Centered-Cubic Metals,” *Philosophical Magazine A*, vol. 37, no. 2, pp. 297–303, 1978. → pages 23
- [69] V. Pontikis, “Computer-Simulation of the Structure and of the Intergranular Diffusion,” *Journal De Physique*. → pages 24
- [70] G. Steinie-Neumann, L. Stixrude, and R. E. Cohen, “Magnetism in dense hexagonal iron,” *Proceedings of the National Academy of Sciences*, vol. 101, p. 33, 2004. → pages 26
- [71] J. Kubler, “Magnetic-Moments of Ferromagnetic and Anti-Ferromagnetic Bcc and Fcc Iron,” *Physics Letters A*, vol. 81, pp. 81–83, 1981. → pages 26
- [72] I. A. Abrikosov, A. E. Kissavos, F. Liot, B. Alling, S. I. Simak, O. Peil, and A. V. Ruban, “Competition between magnetic structures in the Fe rich fcc FeNi alloys,” *Physical Review B*, vol. 76, p. 014434, Jul 2007. → pages 26
- [73] D. W. Boukhvalov, Y. N. Gornostyrev, M. I. Katsnelson, and A. I. Lichtenstein, “Magnetism and Local Distortions near Carbon Impurity in γ -Iron,” *Phys. Rev. Lett.*, vol. 99, p. 247205, Dec 2007. → pages xii, 26, 30, 31
- [74] C. Kittel, *Introduction to solid state physics*. Hoboken, NJ: Wiley, 2005. → pages 26, 78
- [75] M. Matsui and M. Doi, “Magnetic properties of fcc-Fe multilayer,” *Journal of Applied Physics*, vol. 79, no. 8, pp. 5583–5583, 1996. → pages 26
- [76] W. A. A. Macedo and W. Keune, “Magnetism of Epitaxial fcc-Fe(100) Films on Cu(100) Investigated *in Situ* by Conversion-Electron Mössbauer Spectroscopy in Ultrahigh Vacuum,” *Phys. Rev. Lett.*, vol. 61, pp. 475–478, Jul 1988. → pages 26
- [77] S. M. Kim and W. J. L. Buyers, “Vacancy Formation Energy in Iron by Positron-Annihilation,” *Journal of Physics F-Metal Physics*, vol. 8, pp. L103–L108, 1978. → pages 28
- [78] P. Soven, “Coherent-Potential Model of Substitutional Disordered Alloys,” *Phys. Rev.*, vol. 156, pp. 809–813, Apr 1967. → pages 28

- [79] J. M. Sanchez, “Cluster expansions and the configurational energy of alloys,” *Physical Review B*, vol. 48, pp. 14013–14015, Nov 1993. → pages 28
- [80] A. Zunger, S.-H. Wei, L. G. Ferreira, and J. E. Bernard, “Special quasirandom structures,” *Phys. Rev. Lett.*, vol. 65, pp. 353–356, Jul 1990. → pages 28
- [81] S.-H. Shim, A. Bengtson, D. Morgan, W. Sturhahn, K. Catalli, J. Zhao, M. Lerche, and V. Prakapenka, “Electronic and magnetic structures of the postperovskite-type Fe_2O_3 and implications for planetary magnetic records and deep interiors,” *Proceedings of the National Academy of Sciences*, vol. 106, no. 14, pp. 5508–5512, 2009. → pages 29
- [82] K. Knöpfle, L. M. Sandratskii, and J. Kübler, “Spin spiral ground state of γ -iron,” *Physical Review B*, vol. 62, pp. 5564–5569, Sep 2000. → pages 29, 77, 78
- [83] E. Sjöstedt and L. Nordström, “Noncollinear full-potential studies of γ -Fe,” *Physical Review B*, vol. 66, p. 014447, Jul 2002. → pages 29, 77
- [84] T. P. C. Klaver, D. J. Hepburn, and G. J. Ackland, “Defect and solute properties in dilute Fe-Cr-Ni austenitic alloys from first principles,” *Physical Review B*, vol. 85, p. 174111, May 2012. → pages 29, 79, 81
- [85] L. T. Kong and B. X. Liu, “Distinct magnetic states of metastable fcc structured Fe and Fe-Cu alloys studied by ab initio calculations,” *Journal of Alloys and Compounds*, vol. 414, pp. 36–41, 2006. → pages xii, 29, 30
- [86] N. I. Medvedeva, D. V. Aken, and J. E. Medvedeva, “Magnetism in bcc and fcc Fe with carbon and manganese,” *Journal of Physics-Condensed Matter*, vol. 22, p. 31, 2010. → pages 30
- [87] R. Nazarov, T. Hickel, and J. Neugebauer, “First-principles study of the thermodynamics of hydrogen-vacancy interaction in fcc iron,” *Physical Review B*, vol. 82, p. 224104, Dec 2010. → pages 30
- [88] S. Lu, Q.-M. Hu, M. P. J. Punkkinen, B. Johansson, and L. Vitos, “First-principles study of fcc-Ag/bcc-Fe interfaces,” *Physical Review B*, vol. 87, p. 224104, Jun 2013. → pages xii, 31, 32

- [89] V. Vaithyanathan, C. Wolverton, and L. Chen, “Multiscale modeling of θ' precipitation in Al-Cu binary alloys ,” *Acta Materialia*, vol. 52, no. 10, pp. 2973 – 2987, 2004. → pages 32
- [90] V. Vaithyanathan, C. Wolverton, and L. Q. Chen, “Multiscale Modeling of Precipitate Microstructure Evolution,” *Phys. Rev. Lett.*, vol. 88, p. 125503, Mar 2002. → pages 32
- [91] M. Benoit, C. Langlois, N. Combe, H. Tang, and M.-J. Casanove, “Structural and electronic properties of the Au(001)/Fe(001) interface from density functional theory calculations,” *Physical Review B*, vol. 86, p. 075460, Aug 2012. → pages xii, 32, 33, 34
- [92] P. Hohenberg and W. Kohn, “Inhomogeneous Electron Gas,” *Phys. Rev.*, vol. 136, pp. B864–B871, Nov 1964. → pages 39
- [93] W. Kohn and L. J. Sham, “Self-Consistent Equations Including Exchange and Correlation Effects,” *Phys. Rev.*, vol. 140, pp. A1133–A1138, Nov 1965. → pages 39
- [94] W. Parr, Robert G; Yang, *Density-Functional Theory of Atoms and Molecules*. Oxford: Oxford University Press, 1994. → pages 39
- [95] J. P. Perdew, K. Burke, and M. Ernzerhof, “Generalized Gradient Approximation Made Simple,” *Phys. Rev. Lett.*, vol. 77, pp. 3865–3868, Oct 1996. → pages 39
- [96] D. J. Singh, W. E. Pickett, and H. Krakauer, “Gradient-corrected density functionals: Full-potential calculations for iron,” *Physical Review B*, vol. 43, pp. 11628–11634, May 1991. → pages 40
- [97] A. F. E. Wimmer, *Fundamentals of the electronic structure of surfaces, Handbook of Surface Science Vol.2: Electronic structure*. Elsevier, Amsterdam, 2000. → pages xiii, 40, 41
- [98] D. Sheppard, R. Terrell, and G. Henkelman, “Optimization methods for finding minimum energy paths,” *The Journal of Chemical Physics*, vol. 128, no. 13, pp. –, 2008. → pages 41
- [99] H. J. Monkhorst and J. D. Pack, “Special Points for Brillouin-Zone Integrations,” *Physical Review B*, vol. 13, pp. 5188–5192, 1976. → pages 43, 75

- [100] A. van de Walle, M. Asta, and G. Ceder, “The alloy theoretic automated toolkit: A user guide ,” *Calphad*, vol. 26, no. 4, pp. 539 – 553, 2002. → pages 46
- [101] G. Kresse and J. Furthmüller, “Efficient iterative schemes for ab initio total-energy calculations using a plane-wave basis set,” *Physical Review B*, vol. 54, pp. 11169–11186, 1996. → pages 48
- [102] G. Kresse and J. Furthmüller, “Efficiency of ab-initio total energy calculations for metals and semiconductors using a plane-wave basis set,” *Comput. Mater. Sci.*, vol. 6, no. 1, pp. 15 – 50, 1996. → pages 48
- [103] G. Kresse and D. Joubert, “From ultrasoft pseudopotentials to the projector augmented-wave method,” *Physical Review B*, vol. 59, pp. 1758–1775, 1999. → pages 48
- [104] J. P. Perdew, K. Burke, and M. Ernzerhof, “Generalized gradient approximation made simple,” *Phys. Rev. Lett.*, vol. 77, pp. 3865–3868, 1996. → pages 48
- [105] G. Henkelman, B. P. Uberuaga, and H. Jónsson, “A climbing image nudged elastic band method for finding saddle points and minimum energy paths,” *Journal of Chemical Physics*, vol. 113, no. 22, pp. 9901–9904, 2000. → pages 50, 118
- [106] D. Sheppard, P. Xiao, W. Chemelewski, D. D. Johnson, and G. Henkelman, “A generalized solid-state nudged elastic band method,” *J. Chem. Phys.*, vol. 136, no. 7, p. 074103, 2012. → pages 50, 118
- [107] G. H. Vineyard, “Frequency factors and isotope effects in solid state rate processes,” *J. Phys. Chem. Solids*, vol. 3, pp. 121 – 127, 1957. → pages 50
- [108] W. M. Young and E. W. Elcock, “Monte Carlo Studies of Vacancy Migration in Binary Ordered Alloys - I,” *Proc. Phys. Soc. Lond.*, vol. 89, p. 735, 1966. → pages 52
- [109] A. Einstein, “The motion of elements suspended in static liquids as claimed in the molecular kinetic theory of heat,” *Ann Phys-Berlin*, vol. 17, pp. 549–560, 1905. → pages 53

- [110] D. Porter and K. Easterling, *Phase Transformations in Metals and Alloys*. Chapman & Hall, London, 1992. → pages 54
- [111] LAMMPS, “molecular dynamics simulator.”
<http://lammps.sandia.gov>. → pages 54
- [112] M. S. Daw and M. I. Baskes, “Semiempirical, Quantum Mechanical Calculation of Hydrogen Embrittlement in Metals,” *Phys. Rev. Lett.*, vol. 50, pp. 1285–1288, Apr 1983. → pages 54
- [113] R. Johnson and D. Oh, “Analytic embedded atom method model for bcc metals,” *Journal of Materials Research*, vol. 4, pp. 1195–1201, 1989. → pages 54
- [114] G. J. Ackland, D. J. Bacon, A. F. Calder, and T. Harry, “Computer simulation of point defect properties in dilute FeCu alloy using a many-body interatomic potential,” *Philosophical Magazine A*, vol. 75, no. 3, pp. 713–732, 1997. → pages 54
- [115] M. I. Mendeleev, S. Han, D. J. Srolovitz, G. J. Ackland, D. Y. Sun, and M. Asta, “Development of new interatomic potentials appropriate for crystalline and liquid iron,” *Philosophical Magazine*, vol. 83, no. 35, pp. 3977–3994, 2003. → pages 54
- [116] L. Malerba, M. Marinica, N. Anento, C. Björkas, H. Nguyen, C. Domain, F. Djurabekova, P. Olsson, K. Nordlund, A. Serra, D. Terentyev, F. Willaime, and C. Becquart, “Comparison of empirical interatomic potentials for iron applied to radiation damage studies,” *Journal of Nuclear Materials*, vol. 406, no. 1, pp. 19 – 38, 2010. → pages 54
- [117] G. A. Chadwick and D. A. Smith, *Grain Boundary Structure and Properties*. Academic Press, London, 1976. → pages 58, 104
- [118] C. White and W. Coghlan, “The spectrum of binding energies approach to grain boundary segregation,” *Metallurgical Transactions A*, vol. 8, no. 9, pp. 1403–1412, 1977. → pages 58, 104
- [119] L. Huber, I. Elfimov, J. Rottler, and M. Militzer, “*Ab initio* calculations of rare-earth diffusion in magnesium,” *Physical Review B*, vol. 85, p. 144301, 2012. → pages 61, 115

- [120] D. Shin and C. Wolverton, “First-principles study of solute-vacancy binding in magnesium,” *Acta Materialia*, vol. 58, no. 2, pp. 531 – 540, 2010. → pages 61
- [121] P. Lejček and S. Hofmann, “Segregation Enthalpies of Phosphorus, Carbon and Silicon at (013) and (012) Symmetrical Tilt Grain-Boundaries in an Fe-3.5 at.%-Si Alloy,” *Acta Metallurgica Sinica*, vol. 39, pp. 2469 – 2476, 1991. → pages 63
- [122] P. Lejček, *Grain boundary segregation in metals*. Berlin: Springer-Verlag, 2010. → pages 63
- [123] C. Sinclair, C. Hutchinson, and Y. Bréchet, “The effect of nb on the recrystallization and grain growth of ultra-high-purity α -Fe: A combinatorial approach,” *Metall Mater Trans A*, vol. 38, no. 4, pp. 821–830, 2007. → pages 63
- [124] T. Gladman, *The Physical Metallurgy of Microalloyed Steels*. London, Institute of Materials, 1997. → pages 63
- [125] J. D. Eshelby, “The Elastic Interaction of Point Defects,” *Acta Metallurgica Sinica*, vol. 3, no. 5, pp. 487–490, 1955. → pages 65
- [126] J. D. Eshelby, “The Continuum Theory of Lattice Defects,” *Solid State Physics*, vol. 3, pp. 79–144, 1956. → pages 65
- [127] K. A. G. Jr., “Physical Properties and Interrelationships of Metallic and Semimetallic Elements,” vol. 16, pp. 275 – 426, Academic Press, 1964. → pages 66
- [128] G. Rahman, I. G. Kim, and H. K. D. H. Bhadeshia, “A first-principles investigation on the effects of magnetism on the Bain transformation of alpha-phase FeNi systems,” *J. Appl. Phys.*, vol. 111, no. 6, p. 063503, 2012. → pages 66
- [129] T. Moriya, “Spin Polarization in Dilute Magnetic Alloys - with Particular Reference to Palladium Alloys,” *Prog. Theor. Phys.*, vol. 33, no. 2, pp. 157–183, 1965. → pages 67, 108
- [130] P. Olsson, T. P. C. Klaver, and C. Domain, “*Ab initio* study of solute transition-metal interactions with point defects in bcc Fe,” *Physical Review B*, vol. 81, p. 054102, 2010. → pages 67, 68

- [131] M. Levesque, E. Martínez, C.-C. Fu, M. Nastar, and F. Soisson, “Simple concentration-dependent pair interaction model for large-scale simulations of fe-cr alloys,” *Physical Review B*, vol. 84, no. 18, p. 184205, 2011. → pages 69
- [132] A. Deschamps, M. Militzer, and W. Poole, “Comparison of precipitation kinetics and strengthening in an Fe-0.8%Cu alloy and a 0.8% Cu-containing low-carbon steel,” *ISIJ International*, vol. 43, no. 11, pp. 1826–1832, 2003. → pages 69
- [133] M. E. Fine, J. Z. Liu, and M. D. Asta, “An unsolved mystery: The composition of bcc Cu alloy precipitates in bcc Fe and steels,” *Materials Science and Engineering A*, vol. 463, pp. 271–274, 2007. → pages 69
- [134] A. V. Ruban, S. Shallcross, S. I. Simak, and H. L. Skriver, “Atomic and magnetic configurational energetics by the generalized perturbation method,” *Physical Review B*, vol. 70, p. 125115, 2004. → pages 69
- [135] J. von Pezold, A. Dick, M. Friák, and J. Neugebauer, “Generation and performance of special quasirandom structures for studying the elastic properties of random alloys: Application to Al-Ti,” *Physical Review B*, vol. 81, p. 094203, Mar 2010. → pages 75
- [136] V. P. Antropov, M. I. Katsnelson, B. N. Harmon, M. van Schilfgaarde, and D. Kusnezov, “Spin dynamics in magnets: Equation of motion and finite temperature effects,” *Phys. Rev. B*, vol. 54, pp. 1019–1035, Jul 1996. → pages 76
- [137] R. Iglesias and S. Palacios, “*Ab initio* studies on the magnetic phase stability of iron ,” *Acta Materialia*, vol. 55, no. 15, pp. 5123 – 5127, 2007. → pages 78
- [138] M. Acet, H. Zähres, E. F. Wassermann, and W. Pepperhoff, “High-temperature moment-volume instability and anti-Invar of γ -Fe,” *Physical Review B*, vol. 49, pp. 6012–6017, Mar 1994. → pages 78, 119
- [139] G. Rahman, I. G. Kim, H. K. D. H. Bhadeshia, and A. J. Freeman, “First-principles investigation of magnetism and electronic structures of substitutional 3d transition-metal impurities in bcc Fe,” *Physical Review B*, vol. 81, p. 184423, May 2010. → pages 81

- [140] P. Mohan, *Magnetism in the Solid State*. Springer, Berlin, 2003. → pages 81
- [141] M. Enomoto, C. White, and H. Aaronson, “Evaluation of the effects of segregation on austenite grain boundary energy in Fe-C-X alloys,” *Metallurgical Transactions A*, vol. 19, no. 7, pp. 1807–1818, 1988. → pages 89, 103
- [142] D. A. Porter and K. E. Easterling, *Phase Transformations in Metals and Alloys*. Boca Raton, FL : CRC Press, c2009, 2009. → pages 90
- [143] G. Kurdjumow and G. Sachs, “About the mechanism of hardening steel ,” *Zeitschrift Fur Physik*, vol. 64, pp. 325–343, 1930. → pages 90
- [144] J. van der Merwe and G. Shiflet, “The role of structural ledges at phase boundariesIII. F.C.C.-B.C.C. interfaces in Kurdjumov-Sachs orientation ,” *Acta Metallurgica et Materialia*, vol. 42, no. 4, pp. 1199 – 1205, 1994. → pages 90
- [145] K. Ameyama, G. Weatherly, and K. Aust, “A study of grain boundary nucleated widmanstätten precipitates in a two-phase stainless steel,” *Acta Metallurgica et Materialia*, vol. 40, no. 8, pp. 1835 – 1846, 1992. → pages 91
- [146] K. Ogawa and S. Kajiwara, “High-resolution electron microscopy study of ledge structures and transition lattices at the austenite-martensite interface in Fe-based alloys ,” *Acta Metallurgica et Materialia*, vol. 84, pp. 2919–2947, 2004. → pages 91
- [147] J. Rigsbee and H. Aaronson, “The interfacial structure of the broad faces of ferrite plates,” *Acta Metallurgica*, vol. 27, no. 3, pp. 365 – 376, 1979. → pages 91
- [148] W. Tyson and W. Miller, “Surface free energies of solid metals: Estimation from liquid surface tension measurements ,” *Surface Science*, vol. 62, no. 1, pp. 267 – 276, 1977. → pages 94
- [149] D. Jiang and E. A. Carter, “Adsorption and diffusion energetics of hydrogen atoms on Fe(110) from first principles ,” *Surface Science*, vol. 547, no. 1C2, pp. 85 – 98, 2003. → pages 94
- [150] H. Chamati, N. Papanicolaou, Y. Mishin, and D. Papaconstantopoulos, “Embedded-atom potential for Fe and its

- application to self-diffusion on Fe(100) ,” *Surface Science*, vol. 600, no. 9, pp. 1793 – 1803, 2006. → pages 94
- [151] J. Hirth and J. Lothe, *Theory of Dislocations*. Wiley, New York, 1982. → pages 94
- [152] C. Qiu, H. Zurob, D. Panahi, Y. Brechet, G. Purdy, and C. Hutchinson, “Quantifying the Solute Drag Effect on Ferrite Growth in Fe-C-X Alloys Using Controlled Decarburization Experiments,” *Metallurgical and Materials Transactions A*, vol. 44, no. 8, pp. 3472–3483, 2013. → pages 94, 95, 107
- [153] M. Čák, M. Šob, and J. Hafner, “First-principles study of magnetism at grain boundaries in iron and nickel,” *Physical Review B*, vol. 78, p. 054418, Aug 2008. → pages 96
- [154] L. Zhong, R. Wu, A. J. Freeman, and G. B. Olson, “Effects of interfacial relaxation on the magnetic coupling of Mn/Fe(111),” *Journal of Applied Physics*, vol. 81, no. 8, pp. 4479–4481, 1997. → pages 96
- [155] T. Shimada, Y. Ishii, and T. Kitamura, “*Ab initio* study of ferromagnetism in edged iron nanowires under axial strain,” *Physical Review B*, vol. 84, p. 174405, Nov 2011. → pages 96
- [156] D. Yeşilten, M. Nastar, T. A. Arias, A. T. Paxton, and S. Yip, “Stabilizing Role of Itinerant Ferromagnetism in Intergranular Cohesion in Iron,” *Phys. Rev. Lett.*, vol. 81, pp. 2998–3001, Oct 1998. → pages 96
- [157] Y. A. Du, L. Ismer, J. Rogal, T. Hickel, J. Neugebauer, and R. Drautz, “First-principles study on the interaction of H interstitials with grain boundaries in α - and γ -Fe,” *Physical Review B*, vol. 84, p. 144121, Oct 2011. → pages 96
- [158] H. Zurob, D. Panahi, C. Hutchinson, Y. Brechet, and G. Purdy, “Self-Consistent Model for Planar Ferrite Growth in Fe-C-X Alloys,” *Metallurgical and Materials Transactions A*, vol. 44, no. 8, pp. 3456–3471, 2013. → pages 100, 103, 107
- [159] H. Zurob, C. Hutchinson, A. Bch, G. Purdy, and Y. Brchet, “A transition from local equilibrium to paraequilibrium kinetics for ferrite growth in Fe-C-Mn: A possible role of interfacial segregation

- ,” *Acta Materialia*, vol. 56, no. 10, pp. 2203 – 2211, 2008. → pages 100
- [160] H. Zurob, D. Panahi, C. Hutchinson, Y. Bréchet, and G. Purdy, “Self-Consistent Model for Planar Ferrite Growth in Fe-C-X Alloys,” *Metallurgical and Materials Transactions A*, vol. 44, no. 8, pp. 3456–3471, 2013. → pages 107
- [161] C. R. Hutchinson, H. S. Zurob, and Y. Bréchet, “The growth of ferrite in Fe-C-X alloys: The role of thermodynamics, diffusion, and interfacial conditions,” *Metallurgical and Materials Transactions A*, vol. 37A, no. 6, pp. 1711–1720, 2006. → pages 107
- [162] H. Chen and S. van der Zwaag, “Analysis of ferrite growth retardation induced by local Mn enrichment in austenite created by prior interface passages ,” *Acta Materialia*, vol. 61, no. 4, pp. 1338 – 1349, 2013. → pages 107
- [163] E. Vincent, C. Becquart, and C. Domain, “Solute interaction with point defects in alpha Fe during thermal ageing: A combined ab initio and atomic kinetic Monte Carlo approach,” *J. Nucl. Mater.*, vol. 351, pp. 88 – 99, 2006. → pages 111
- [164] F. Soisson and C.-C. Fu, “Cu-precipitation kinetics in α -Fe from atomistic simulations: Vacancy-trapping effects and Cu-cluster mobility,” *Physical Review B*, vol. 76, p. 214102, 2007. → pages 111
- [165] Y. Iijima, K. Kimura, and K. Hirano, “Self-diffusion and isotope effect in α -iron ,” *Acta Metallurgica*, vol. 36, no. 10, pp. 2811 – 2820, 1988. → pages xvii, 112, 117
- [166] C. N. Yang, “The Spontaneous Magnetization of a Two-Dimensional Ising Model,” *Phys. Rev.*, vol. 85, pp. 808–816, Mar 1952. → pages 113
- [167] S. M. Bhattacharjee and A. Khare, “Fifty years of the exact solution of the two-dimensional Ising model by Onsager,” *Curr.Sci.*, vol. 69, pp. 816–820, 1995. → pages 113
- [168] H. Nitta and Y. Iijima, “Influence of magnetization change on solute diffusion in iron,” *Philosophical Magazine Letters*, vol. 85, no. 10, pp. 543–548, 2005. → pages 113

- [169] G. Neumann and C. Tuijn, *Self-diffusion and impurity diffusion in pure metals : handbook of experimental data*. Amsterdam ; Boston : Pergamon/Elsevier, 2009. → pages xvii, 114
- [170] M. Lübbehusen, *Diploma work*. Univ. Münster, 1984. → pages xvii, 116, 117
- [171] C. Herzig, J. Geise, and S. Divinski, “Niobium bulk and grain boundary diffusion in α -iron,” *Z. Metallk.*, vol. 93, no. 12, pp. 1180–1187, 2002. → pages xvii, 116, 117
- [172] H. Nitta and Y. Iijima, “Influence of magnetization change on solute diffusion in iron,” *Philosophical Magazine Letters*, vol. 85, no. 10, pp. 543–548, 2005. → pages xvii, 114, 116
- [173] A. L. Claire, “Solute diffusion in dilute alloys,” *Journal of Nuclear Materials*, vol. 69-70, no. 0, pp. 70 – 96, 1978. → pages 115
- [174] M. Lübbehusen and H. Mehrer, “Self-diffusion in α -iron: The influence of dislocations and the effect of the magnetic phase transition ,” *Acta Metallurgica et Materialia*, vol. 38, no. 2, pp. 283 – 292, 1990. → pages xvii, 116, 117, 121, 122
- [175] F. Buffington, K. Hirano, and M. Cohen, “Self diffusion in iron ,” *Acta Metallurgica*, vol. 9, no. 5, pp. 434 – 439, 1961. → pages xvii, 119, 121, 122
- [176] C. M. Walter and N. L. Peterson, “Isotope Effect in Self-Diffusion in Iron,” *Phys. Rev.*, vol. 178, pp. 922–929, Feb 1969. → pages 116
- [177] J. Kirkaldy, P. Smith, and R. Sharma, “Diffusion of manganese in paramagnetic BCC iron,” *Metallurgical Transactions*, vol. 4, no. 2, pp. 624–625, 1973. → pages 116
- [178] J. Geise and C. Herzig, “Lattice and Grain-Boundary Diffusion of Niobium in Iron,” *Z. Metallk.*, vol. 76, p. 622, 1985. → pages xvii, 116, 117
- [179] D. Bergner, Y. Khaddour, and S. Lörx, “Diffusion of Si in bcc- and fcc-Fe,” *Defect and Diffusion Forum*, vol. 66-69, p. 1407, 1989. → pages 119, 120
- [180] G. Neumann and C. Tuijn, *Self-diffusion and Impurity Diffusion in Pure Metals: Handbook of Experimental Data*. Pergamon Materials Series, Elsevier Science, 2011. → pages 119

- [181] Y. L. Bouar and F. Soisson, “Kinetic pathways from embedded-atom-method potentials: Influence of the activation barriers,” *Physical Review B*, vol. 65, p. 094103, 2002. → pages 125
- [182] A. Inoue, H. Nitta, and Y. Iijima, “Grain boundary self-diffusion in high purity iron,” *Acta Materialia*, vol. 55, no. 17, pp. 5910 – 5916, 2007. → pages 127
- [183] J. Bernardini, P. Gas, E. Hondros, and M. Seah, “Grain boundary diffusion: from fundamentals to recent developments,” *Proceedings of the Royal Society A*, vol. 379, p. 159, 1982. → pages 127
- [184] N. Bernstein, J. R. Kermode, and G. Csnyi, “Hybrid atomistic simulation methods for materials systems,” *Reports on Progress in Physics*, vol. 72, no. 2, p. 026501, 2009. → pages 135
- [185] X. Zhang, G. Lu, and W. A. Curtin, “Multiscale quantum/atomistic coupling using constrained density functional theory,” *Phys. Rev. B*, vol. 87, p. 054113, Feb 2013. → pages 135